SERI/STR-211-2924
UC Category: 63
DE86004453

MASTER

SERI/STR--211-2924

DE86 004453

Research on High-Efficiency Single-Junction Monolithic Thin-Film Amorphous Silicon Solar Cells

Annual Subcontract Report — Phase 2
1 December 1984 - 30 November 1985

F. E. Aspen, D. P. Grimmer, R. L. Jacobson,
F. R. Jeffrey, N. T. Tran
Electronic and Information Sector Laboratories/3M
St. Paul, MN

April 1986

SERI Technical Monitor:
W. Wallace

Prepared under Subcontract No. ZB-4-03056-2

Solar Energy Research Institute
A Division of Midwest Research Institute

1617 Cole Boulevard
Golden, Colorado 80401-3393

Prepared for the
U.S. Department of Energy
Contract No. DE-AC02-83CH10093

DISTRIBUTION OF THIS DOCUMENT IS UNLIMITED

DISCLAIMER

DISCLAIMER

PREFACE

This Annual Report-Draft covers the work performed by the Electrical and Communications Technologies Laboratory of the 3M Company, St. Paul, Minnesota, for the period 01 December 1984 to 30 November 1985 under Subcontract No. ZB-4-03056-2. The Project Manager is Dr. Donald L. Janes and the Technical Manager is Dr. James V. Burt. The staff members (and associate staff personnel) who have contributed to the report, and their areas of specialization, are listed below.

Dr. Frank E. Aspen	Research Specialist, Sputter Deposition of Thin Films Task Two Leader
Dr. Fred Bacon	Surface Analysis
Mr. Joseph Cross	Solar Simulator
Mr. John K. Echo	Graphic Design
Mr. Jathan Edwards	Amorphous Silicon Deposition
Dr. Kenneth A. Epstein	Transport and Stability Measurements
Mr. James R. Gergen	SEM and EDX
Mr. James R. Gilbert	Amorphous Silicon Deposition and Measurement
Dr. Derrick Grimmer	Senior Physicist, Submodule Design/Fabrication Task Four Leader
Dr. Erick Hockert	Laser Scribing
Mr. Richard L. Jacobson	Senior Research Specialist, Multi-Chamber Vacuum System Design/Fabrication Task Five Leader
Dr. Frank R. Jeffrey	Research Specialist, Amorphous Silicon Device Fabrication/Measurement Task Three Leader
Mr. David C. Knoll	Laser Scanner for Defects
Mr. James Krause	Optical Modeling
Mr. Pat Lasswell	University of Delaware, Institute of Energy Conversion Laser Scanner

Dr. David K. Misemer	Device Modeling
Dr. Arnold Moore	University of Delaware, Institute of Energy Conversion Surface Photovoltage
Mr. David J. Mullen	Technical Report Editor
Mr. David V. Nins	ITO Deposition
Mr. Donald J. Olsen	Amorphous Silicon Deposition
Dr. Rajendra I. Patel	Plasma Diagnostics
Dr. Thomas C. Paulick	Optical Modeling for Back Contact
Mr. Ken Paulson	Laser Scribing
Mr. James Petrell	Computer Control
Dr. James Phillips	University of Delaware, Institute of Energy Conversion Solar Simulation
Ms. Joan Richards	Laser Scribing
Mr. William B. Robbins	ITO Research
Ms. Christine Swansen	Gas Purity Analysis
Ms. Linda S. Thalhuber	Government Programs Coordinator
Dr. Nang Tran	Research Specialist, Amorphous Silicon Material Deposition Measurement Task One Leader
Mr. George D. Vernstom	Amorphous Silicon Deposition and Measurement, and EBIC Measurements
Dr. Michael Weber	Amorphous Silicon Deposition, Optical Modeling
Mr. Roger K. Westerberg	Mechanical Design Engineer
Mr. Robert C. Williams	Amorphous Silicon Deposition
Mr. Steve Znameroski	Metallization

SUMMARY

For the past two years, 3M Company has been involved in a three-year research and development program which is being partially funded by the Solar Energy Research Institute. The primary goal of this program is to advance the state-of-the-art of single-junction, flexible, thin film amorphous silicon solar cells using glow discharge deposition techniques. 3M believes that its extensive expertise in continuous, large-area vacuum deposition processes, which utilizes a variety of different thin-caliper substrate materials, will significantly influence the future commercialization of flexible solar cells.

This Annual Technical Progress Report-Draft covers the progress made in Phase II of this program, for the period which extends from December 1, 1984 through November 30, 1985. The accomplishments in this program during the past year are summarized in this section and presented in detail in this report.

Deposition System One has been modified and is now capable of simultaneously depositing films on eight substrates per run. Depositions are monitored by plasma diagnostics using both optical emission and quadrupole mass spectroscopy.

A diffusion length of 0.57 micrometer under AM1 illumination conditions was achieved for intrinsic a-Si deposited on metal-coated polyimide substrate. Lightly boron-doped a-Si films exhibit better diffusion length characteristics than undoped a-Si films. However, the diffusion length of both lightly boron-doped and undoped silicon films stabilize at 0.3 micrometer after 400 hours of continuous AM1 illumination.

Modifications to the gas analysis system allow detection levels of approximately 1 ppm to be achieved. Deposition rates of 8 Å/second have been achieved using silane/hydrogen gas mixtures with virtually no dust formation. The emission intensities, I_{SiH} and I_H, and the deposition rate monotonically increase with power. The deposition rate was also found to be linearly dependent on the I_{SiH} of the silane/hydrogen plasma.

Stability studies were initiated by lightly doping intrinsic layers with boron. For a-Si films grown from a gas mixture containing 5 ppm diborane, the photocurrent decreased by 30% after two hours of AM1 illumination and then remained stable over the next 70 hours of illumination. The light current data returned to their original values after three hours of annealing at 160°C. Intrinsic layers with lightly doped fluorine and phosphorous compensated with boron have also been studied although coherent results have not yet been obtained. Surface photovoltage, sub-band photocurrent, electron spin resonance, and time-of-flight measurements are being used to study degradation mechanisms. Typical defect densities of 2×10^{16} spins/cm^3 for powders and 6×10^{15} spins/cm^3 for a-Si films have been observed.

Cross-contamination studies of the p^+/i and i/n^+ interfaces have been initiated using SIMS analysis. The effects of contaminants on device quality are being investigated.

a-SiC:H films have been optimized for use as both p^+ and n^+ layers. These layers have been evaluated for use as a window layer in p-i-n and n-i-p a-Si solar cells.

Currently, both Ni and Al/TiN bilayers are being used as back contacts. The Al/TiN bilayer is preferred because of its higher reflectivity, higher conductivity, and the greater amount of diffuse scattering of reflected light that it provides compared to Ni. TiN is an effective diffusion barrier that does not reduce the reflectivity of Al.

Indium tin oxide (ITO) is used as the front contact. 2100 Å thick ITO films deposited at room temperature have a sheet resistance of 30 ohms/square and 2 to 5% absorption loss over the wavelengths of 500 to 700 nm. Heat treatment studies at 130°C indicate that the ITO/a-Si interface is unstable without a diffusion barrier.

Improvement in the red response has been achieved by texturing the polyimide substrate using sputter etching techniques.

An investigation to characterize defects and to study defect densities in a-Si devices using EBIC is ongoing. The four major categories of defects are discussed in Section 4.0 of this report.

Studies of the effects of substrate surface roughness on the charge collection of a-Si devices and the relationship between active area and defect density have been initiated.

The thermal coefficient of expansion of our best polyimide film and of a-Si are very similar, which significantly reduces web curling after deposition. By reducing the formation of Si powder accumulations in System 4, a marked improvement in device quality has been realized.

The best device parameters observed for standard construction cells on polyimide are: $V_{oc} = 0.9V$, $FF = 0.65$, $J_{sc} = 13.5\ mA/cm^2$, Eff = 7.2%.

Good quality devices with fill factors as high as 0.65 have been produced using a-SiN as the n^+ layer. This layer serves as an indium diffusion barrier and as part of the optical anti-reflection coating.

An optical modeling program was created for use in identifying optimum anti-reflection coatings. The results show that several options are viable, and also quantify the tradeoff between the ITO thickness and reflection losses.

Intrinsic layer doping with boron in single chamber systems is ineffective due to the extensive level of boron carry-over from depositing the p+ layer. In the new two-chamber system, an improved p^+-i interface and the reduction of the boron content in the i-layer have been demonstrated.

The effect of dopant profiles on V_{oc} has shown that the differences in V_{oc} commonly observed between p-i-n and n-i-p cells are due to boron carry-over in the intrinsic layer. Surface recombination at the p/i interface appears to be the limiting factor for low V_{oc} devices. The boron profile reduces this surface recombination, allowing V_{oc} to increase to the level where it is controlled by bulk recombination.

The construction of monolithic a-Si solar cell submodules is progressing. The submodules are produced from YAG-laser scribed series-connected 0.5 x 10.0 centimeter cells fabricated on flexible polyimide substrate. Efforts are being made to improve the mechanics of accurate substrate positioning and laser output control.

Evaluation of the submodules using the ELH bulb solar simulator and laser scanner defect detector continues. In particular, efforts to determine the sources of submodule defects has intensified. Reduced submodule efficiency has been partially attributed to surface damage and debris generation arising from the laser scribing process. A systematic materials investigation of deposited scribed layers as well as of complete devices is under way to study the causes of high interconnect resistance and low open circuit voltages in submodules.

The multi-chamber deposition system became operational in June, 1985. Numerous single and multi-layer a-Si films have been deposited in the system to date. Both undoped and doped films have demonstrated properties which are characteristic of good quality a-Si material. One series of depositions has demonstrated that cross-contamination between deposition chambers is less than 1 ppm under typical operating conditions.

p-i-n layers, with good I-V characteristics, were made by depositing all three layers continuously and sequentially in the multi-chamber system.

TABLE OF CONTENTS

TABLE OF CONTENTS (continued)

LIST OF FIGURES

LIST OF FIGURES (continued)

LIST OF FIGURES (continued)

LIST OF FIGURES (continued)

LIST OF FIGURES (continued)

LIST OF TABLES

LIST OF EQUATIONS

1.0 INTRODUCTION

The present program, which is titled: "Research On High Efficiency Single-Junction Monolithic Thin Film Amorphous Silicon Solar Cells," consists of five research tasks. These tasks are: (1) amorphous silicon materials research, (2) non-semiconductor materials research, (3) solar cell research, (4) monolithic, intra-connected cells/submodule research and (5) multi-chamber deposition system research.

2.0 TASK ONE - AMORPHOUS SILICON MATERIALS RESEARCH

2.1 Amorphous Silicon Materials Research Progress

2.1.1 Gas Analysis by Mass Spectroscopy

A dedicated gas analysis system for analyzing the composition and purity of incoming gases used in the deposition of a-Si has been constructed. The system is based on the method of gas analysis known as "modulated beam mass spectrometry." Test gas from a cylinder being analyzed is metered into a vacuum system and a gas beam is defined by a limiting aperture. The beam is mechanically chopped just prior to entering the ionization section of a mass spectrometer to minimize mass peaks due to residual background gases. Measurements are made using a UTI quadrupole spectrometer, Model 200C, with a mass range to 300 AMU. The quadrupole output approximates a square wave and is phase sensitive detected using a Princeton Model 5101 lock-in amplifier. The dc output is displayed on an X-Y recorder as a function of the mass-to-charge ratio.

The analysis system is contained in a stainless steel chamber with Conflat flanges. It is bakable to $200^{\circ}C$ and residual gas pressures during analysis are typically in the 10^{-9} torr range. The system is pumped with a TMP 360 liter/second turbomolecular pump. The gas inlet manifold contains a gas regulator to which cylinders are connected through a stainless steel flexible line. Provision is made to purge the manifold with high purity argon during cylinder changes. The entire manifold is constructed of welded stainless steel with VCR fittings. Care is taken to obtain a representative gas sample from cylinders by charging and evacuating the gas manifold several times prior to running an analysis.

The system has been successfully used to analyze the composition and purity of all incoming gas cylinders. The majority of gas cylinders analyzed to date have had impurity levels of less than 10 ppm. Cylinders that have shown impurities in excess of this level are listed in Table 2-1. Most of these cylinders were not used in a-Si deposition systems.

Table 2-1. Contaminated Gas Cylinders

Cylinder #	Composition	Contaminants
YR 7437	100% SiH_4	~40 ppm $Si_2H_xO^+$
UN 1954	100% SiH_4	~70 ppm SiH_xO^+
AH 9549	100% SiH_4	~40 ppm Ar and ~30 ppm CO_2
AH 9650	100% SiH_4	~50 ppm Ar and ~40 ppm CO_2
AH 7241	10% SiH_4 in H_2	~50 ppm CO_2
AH 9652	10% SiH_4 in H_2	~40,000 ppm Ar and ~20 ppm CO_2
AH 9651	10% SiH_4 in H_2	~40,000 ppm Ar and ~20 ppm CO_2
AE 5164	10% SiH_4 in H_2	~60 ppm CO_2
XX 2841	5.8 ppm B_2H_6 in H_2	~50 ppm N_2

2.1.2 Intrinsic Material

A new reactor design, as shown in Figure 2-1, has been incorporated into deposition System One. The dimensions of this reactor are the same as those of System Four in order to maintain a consistent geometry relationship between the different systems. Using this new design, several samples can be fabricated per run and several runs can be performed per day. This capability will greatly facilitate the materials optimization effort. The system is equipped with optical emission spectroscopy and mass spectro scopy for use in high deposition rate studies, interface studies between individual a-Si layers, and in the preparation of p-i-n devices having various configurations. System Two is dedicated to studying the stability of lightly doped a-Si films incorporated with various dopants such as boron, fluorine, and boron compensated with phosphorous, and to optimization studies of the p^+ a-SiC:H window layer.

Several series of depositions have been performed in Systems One and Two in order to determine the optimum parameters for depositing intrinsic and p^+ a-SiC:H window layer materials. Parameters which have been studied include: a) varying the RF power and SiH_4 flow rate, b) heating the substrate to 250°C, c) using a system pressure of 1 torr, d) varying the ratio of SiH_4/H_2, and e) varying dopant concentration levels from 0.2 to 5 ppm.

Typical deposition parameters used in making high quality p^+, i, and n^+ a-Si layers are shown in Table 2-2.

Table 2-2. Typical Deposition Parameters For High Quality p^+, i And n^+ Layers Of Amorphous Silicon

	System 1	System 2	System 4	System 5 (Semi-Multi-Chamber)	Multi-Chamber
p^+	Ts = 250°C pure SiH_4 $B_2H_6/SiH_4 = 1x10^{-2}$ $3.2x10^{-2} W/cm^2$	Ts = 250°C $SiH_4/H_2 = 1x10^{-1}$ $B_2H_6/SiH_4 = 2x10^{-2}$ $3.1x10^{-2} W/cm^2$	Ts = 250°C $SiH4/H_2 = 9x10^{-2}$ $B_2H_6/SiH_4 = 2x10^{-2}$ $2.2x10^{-2} W/cm^2$	Ts = 250°C $SiH_4/H_2 = 5.3x10^{-2}$ $CH_4/SiH_4 = 9.3x10^{-1}$ $B_2H_6/SiH_4 = 1.8x10^{-2}$ $9x10^{-2} W/cm^2$	Ts = 200°C 1.0 Torr $SiH_4/H_2 = 2x10^{-2}$ $B_2H_6/SiH_4 = 2x10^{-2}$ $4.3x10^{-2} W/cm^2$
i	Ts = 250°C $SiH_4/He = 1/2$ $3.1x10^{-2} W/cm^2$	Ts = 250°C $SiH_4/H_2 = 1x10^{-1}$ 0.5 ppm B_2H_6 $3.2x10^{-2} W/cm^2$	Ts = 250°C $SiH_4/H_2 = 1.1x10^{-1}$ $2.2x10^{-2} W/cm^2$	Ts = 200°C $SiH_4/H_2 = 1x10^{-1}$ $6x10^{-2} W/cm^2$	Ts = 225°C 1.0 Torr $SiH_4/H_2 = 1x10^{-1}$ 1ppm B_2H_6 $2.2x10^{-2} W/cm^2$
n^+	Ts = 250°C pure SiH_4 $PH_3/SiH_4 = 2x10^{-2}$ $3.1x10^{-2} W/cm^2$	Ts = 250°C $SiH_4/H_2 = 1x10^{-1}$ $PH_3/SiH_4 = 1x10^{-2}$ $9.6x10^{-2} W/cm^2$	Ts = 250°C $SiH_4/H_2 = 1.1x10^{-1}$ $PH_3/SiH_4 = 1.3x10^{-2}$ $2.6x10^{-2} W/cm^2$	Ts = 250°C $SiH_4/H_2 = 1.7x10^{-2}$ $PH_3/SiH_4 = 1.8x10^{-2}$ $6x10^{-1} W/cm^2$	Ts = 200°C 1.0 Torr $SiH_4/H_2 = 7x10^{-3}$ $PH_3/SiH_4 = 1x10^{-2}$ $1.3x10^{-1} W/cm^2$

2.1.2.1 Thermodynamic Study of the Silane-Hydrogen Chemical System

Thermodynamic calculations of the chemical equilibrium compositions of various species were performed for the silane/hydrogen system at different temperatures (500^{o} to 6000^{o}K), pressures (0.01 to 10 torr), and silane mixing fractions. A computer program to calculate the equilibrium properties of plasmas containing various ionized species, was obtained from NASA, Lewis Research Center. The program code uses all the species with known thermodynamic functions that are available in its thermodynamic library. For species whose thermodynamic functions are not available, another program (PAC code) can be used to calculate the required functions from spectroscopic constants.

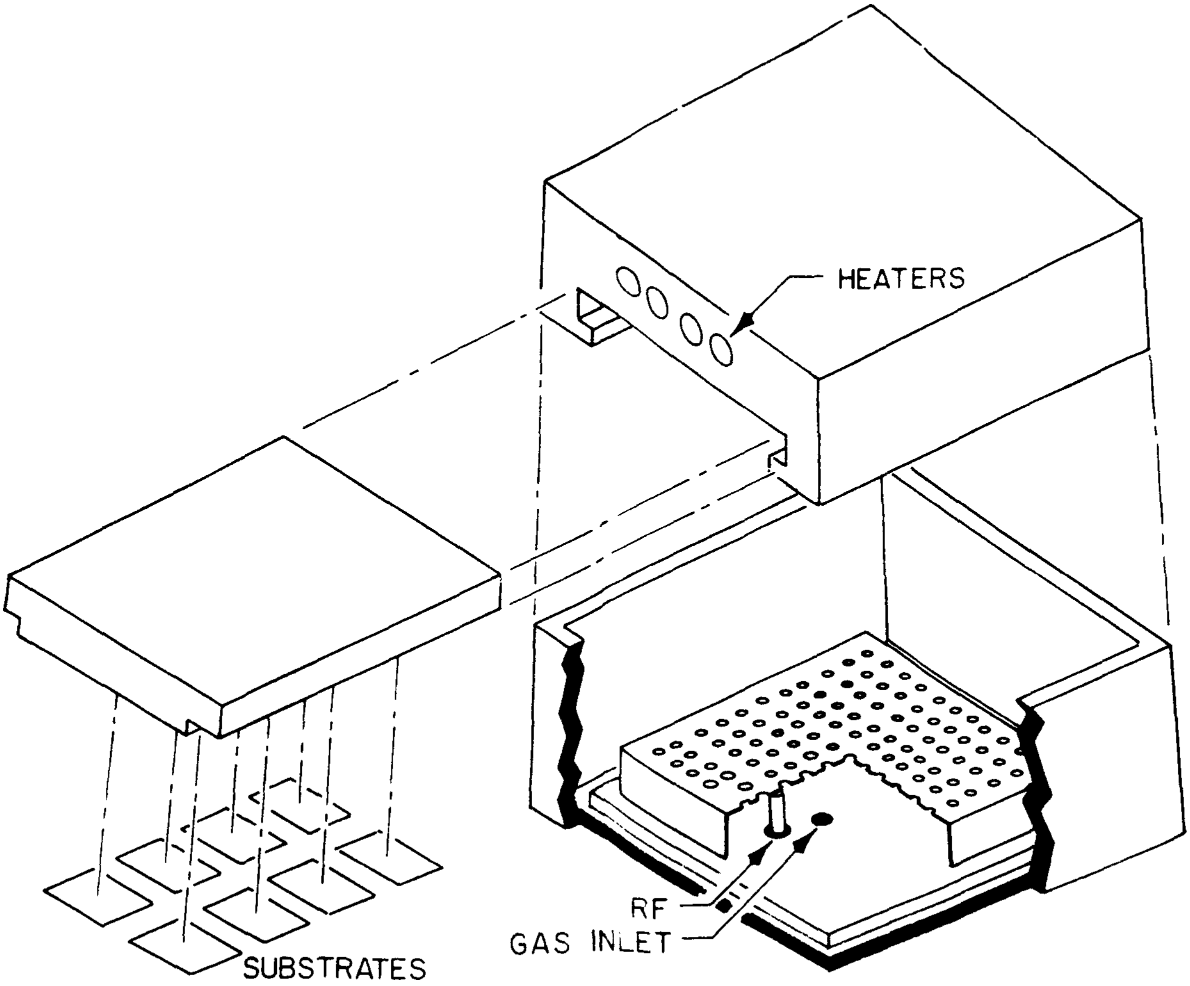

Figure 2-1. Schematic Diagram Of The Reactor For System One

Figure 2-2, illustrates the pressure dependence of calculated equilibrium compositions of Si, Si_2, Si_3, SiH, SiH_2 and SiH_3. At a SiH_4/H_2 ratio of 0.1 and 2000°K, silicon containing species rise monotonically with pressure and reach a maximum at 5 torr. Figure 2-3, shows the profiles of silicon containing species for different silane fractions in hydrogen at a temperature of 2000°K and a total pressure of 1 torr. Silicon species reach a maximum in silane mixtures of greater than 30%.

For an optimized high deposition rate, this calculation predicts a system with a silane fraction of 30% in H_2 at a total system pressure of 5 torr, and a system temperature of 2000°K.

Calculations for a P-doped SiH_4/H_2 system as well as for a B-doped SiH_4/H_2 system, have also been made.

Additional results and further discussion of this work are given in Reference 1.

2.1.2.2 High Deposition Rate of Intrinsic Material

High deposition rate studies of intrinsic layers were performed in System One, using various SiH_4/H_2 gas mixtures [2]. The dimensions of the RF electrodes in this system are 5 inches x 5 inches, and the electrodes are spaced a distance of 3/4-inch apart. Optical emission spectra were accumulated using a PAR/EG&G optical multi-channel analyzer and the data were stored on a magnetic disk during depositions.

Gas analysis results for pure SiH_4 which was utilized in these studies are shown in Figure 2-4. SiH_x^+ and $Si_2H_x^+$ peaks were observed.

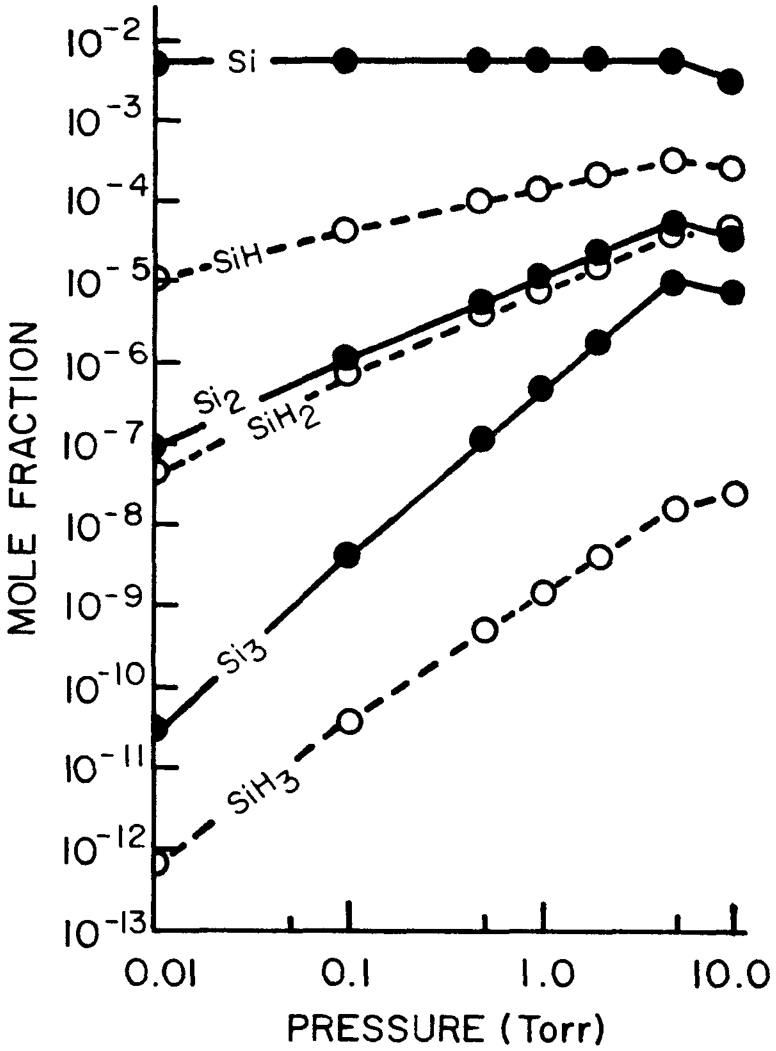

Figure 2-2. Pressure Dependence Of Calculated Equilibrium Compositions Of Si, Si_2, Si_3, SiH, SiH_2, And SiH_3 For $SiH_4/H_2 = 0.1$ And T = 2000°K

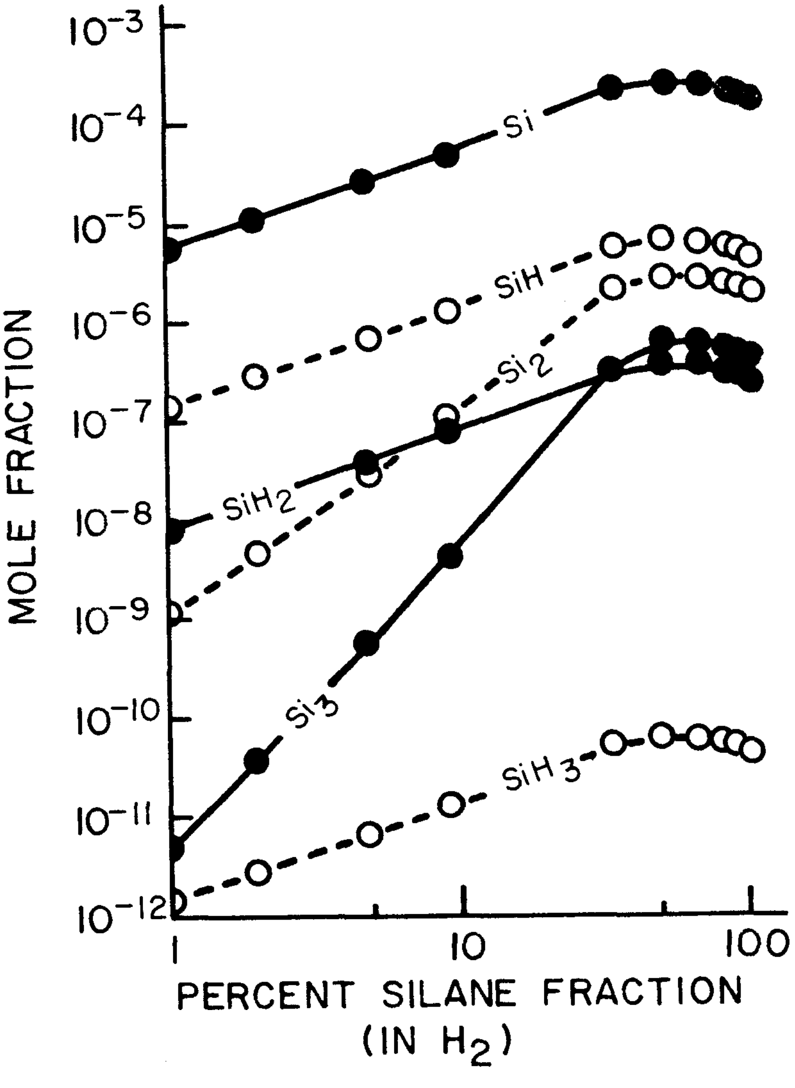

Figure 2-3. Silane Fraction Dependence On Equilibrium Concentrations Of Si, Si_2, Si_3, SiH, SiH_2, And SiH_3 At T = 2000°K And Total Pressure Of 1 Torr

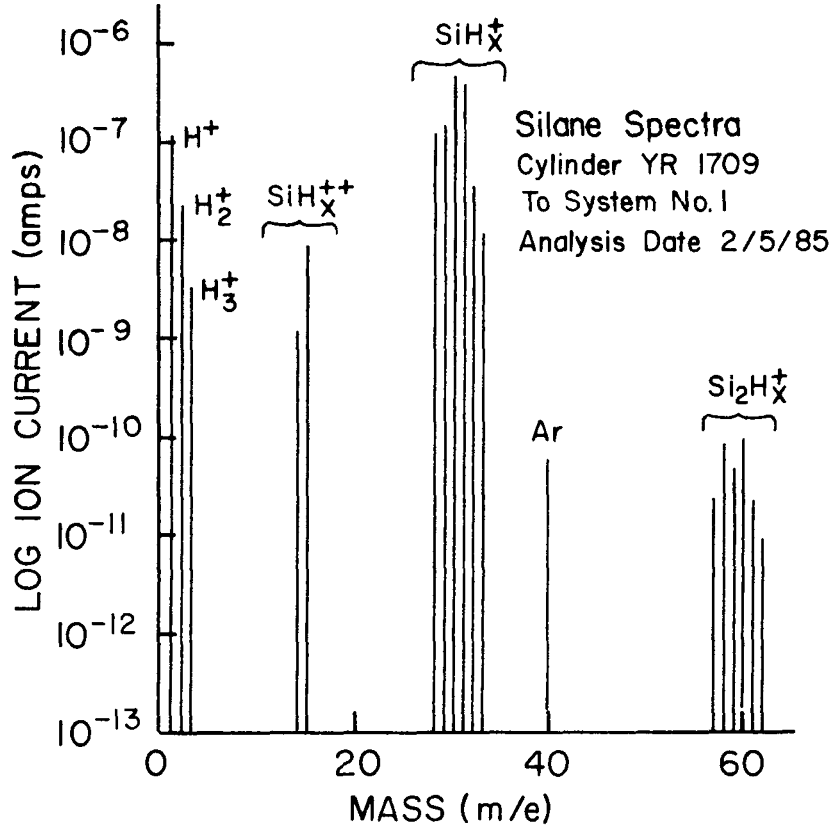

Figure 2-4. Mass Spectra Of Pure Silane

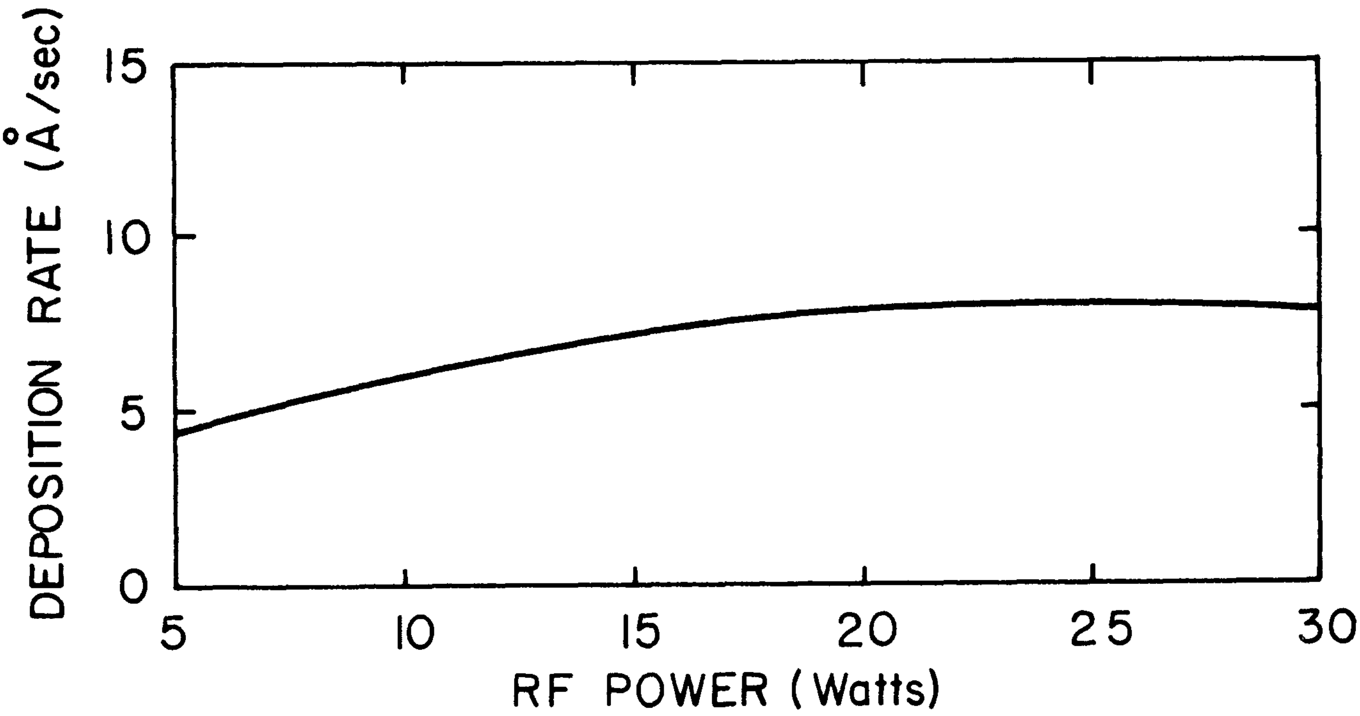

Figure 2-5. Deposition Rate As A Function Of RF Power For SiH_4/H_2 Mixtures

The following observations have been made:

(i) Films made under different deposition conditions exhibit a band gap of 1.76 eV, an activation energy of 0.75 eV, and a light/dark current ratio in the mid to high 10^5 range.

(ii) Good film properties can be obtained at a deposition rate of 8 Å/second using a 33% silane in hydrogen mixture with virtually no dust formation, as shown in Figure 2-5.

(iii) In general, the deposition rate is linearly proportional to the [SiH] intensity as shown in Figure 2-6 and the deposition rate increases with increasing power.

(iv) [SiH/H] decreases exponentially with power, as shown in Figure 2-7.

(v) [SiH/H] increases with the SiH_4 fraction in the SiH_4/H_2 mixture as shown in Figure 2-8.

(vi) At a fixed power value, the deposition rate increases as a function of the silane fraction.

(vii) The substrate temperature, T_s, in the 200^o to 300^oC range, has no effect on the deposition rate and [SiH/H].

In Figure 2-9, the intensity of I_{SiH} and I_H is plotted as a function of power for mixtures of silane in H_2. I_{SiH} and I_H increase linearly with the RF power and intersect at a power level of ~35W for a SiH_4/H_2 ratio of 1:10. The IR spectra of a-Si films prepared at an RF power of 15 watts for two different mixing ratios were identical as shown in Figure 2-10. It has been observed by J. Knights et. al., [3] and other researchers that the stretching mode at 2090 cm^{-1} (corresponding to $[SiH_2]_n$) increases with RF power, and ratios of the stretching mode at 2000 cm^{-1} (corresponding to SiH) to 2090 cm^{-1} decrease with RF power. This correlates well with the I_{SiH}/I_H ratio shown in Figure 2-7. This correlation suggests that the I_{SiH} corresponds to the 2000 cm^{-1} band of [SiH], and the I_H corresponds to the 2090 cm^{-1} band of $[SiH_2]_n$ observed with infrared spectroscopy. There is a correlation between $(SiH_2)n$, of which the corresponding IR peak is 2090 cm^{-1}, with voids in the a-Si network.

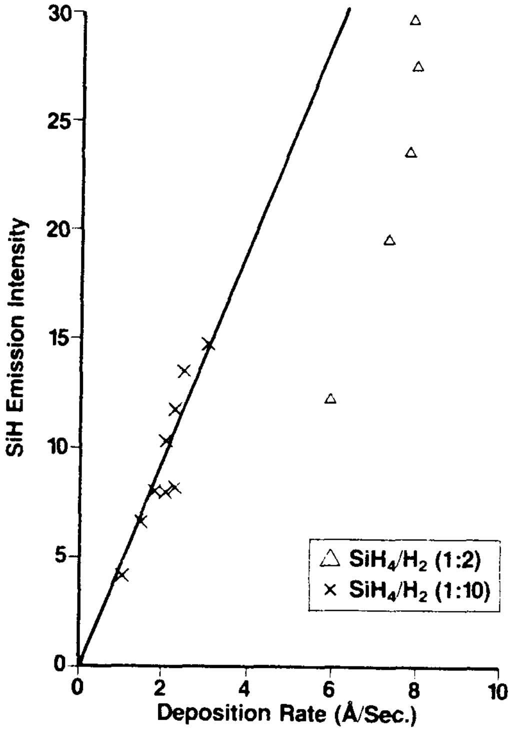

Figure 2-6. Deposition Rate Is Proportional To $I_{[SiH]}$ Signal Intensity

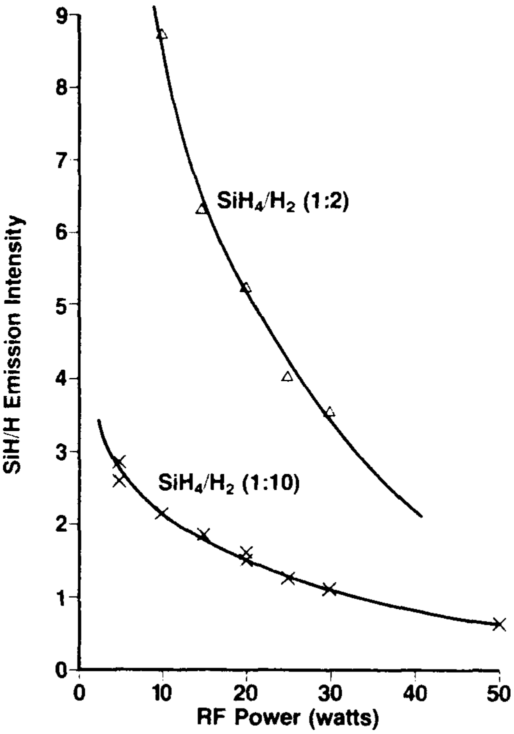

Figure 2-7. Power Dependence Of [SiH/H]

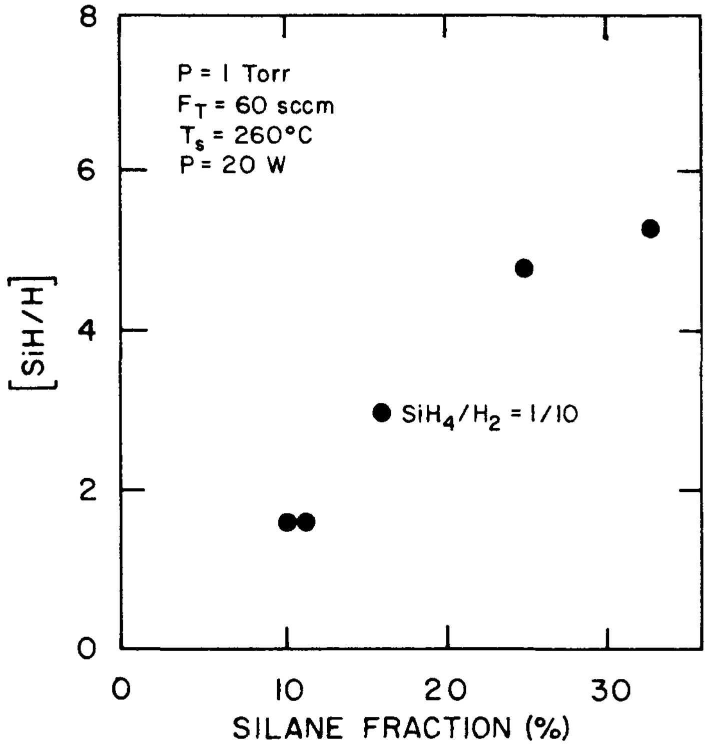

Figure 2-8. Silane Fraction Dependence Of [SiH/H]

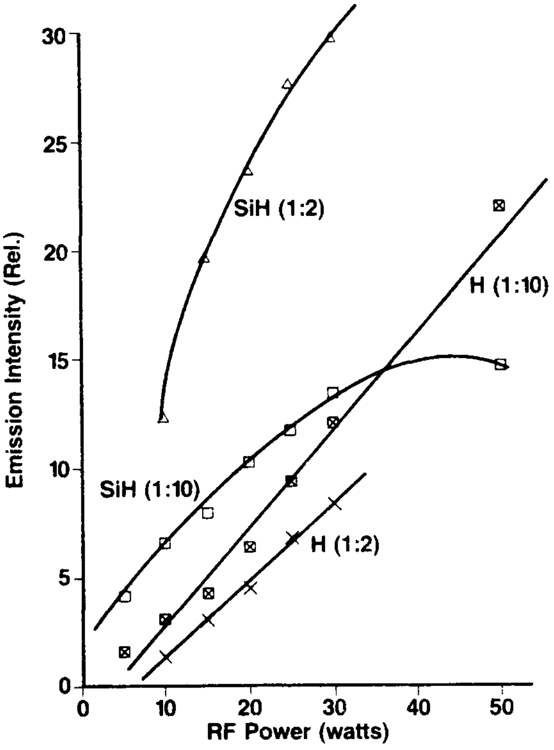

Figure 2-9. Intensity Of I_{SiH} And I_H Plotted As A Function Of Power For SiH_4/H_2 Mixtures

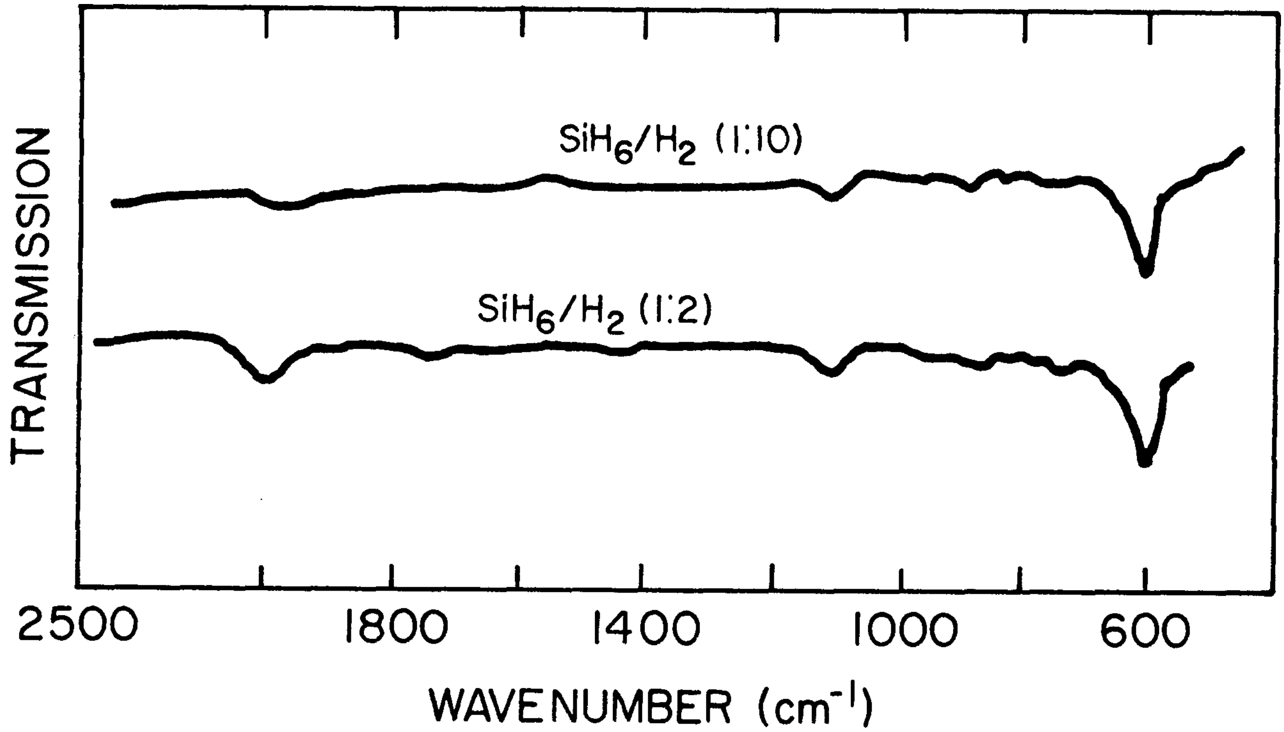

Figure 2-10. **IR Spectra Of Si:H Films Prepared At 15 Watts For Two Silane Mixtures**
Thickness of the films is 1.0 µm.

Therefore, to produce films of high quality, it may be advantageous to maintain the I_{SiH} and I_H below the power level where the intersection occurs in the optical emission spectroscopy data, i.e., in the case of SiH_4/H_2 mixture of 1:10, the corresponding power level is ~35W. Presumably, the power level varies with the geometry of the reactor, and optical emission spectroscopy can be a useful tool for screening the properties of the films.

2.1.2.3 Surface Photovoltage (SPV)

A computerized system for measuring surface photovoltage (SPV) was designed and built by Dr. Arnold Moore of the Institute of Energy Conversion at the University of Delaware. A schematic diagram of the system is shown in Figure 2-11.

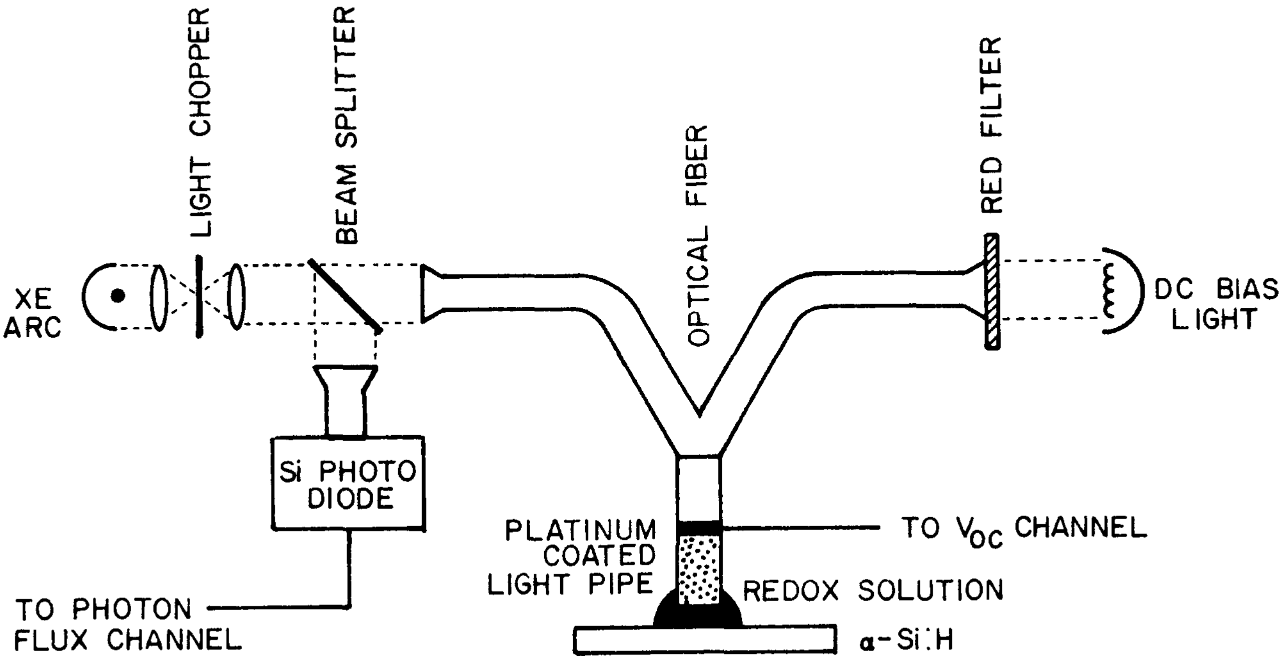

Figure 2-11. Block Diagram Of SPV Apparatus Using Redox Electrochemical Liquid Pickup
Light is conducted to the sample surface by fiber optics. A servo loop adjusts the light intensity to keep the SPV constant at all wavelengths.

The quinone-hydroquinone electrolyte, buffered at a pH of 6 to complete the liquid Schottky barrier, is contained between the sample and probe by adhesion and surface tension which allows light to reach the a-Si films while permitting easy sample interchange. An HP 3497A data acquisition system and an HP 86B controller disk drive are used to store and print data. References 4 and 5 provide additional detailed information.

Samples were prepared by first depositing a metal contact such as Cr (1000 Å thick) onto a Corning 7059 glass substrate followed by a highly conductive n^+ layer (200 Å thick). Undoped and lightly B-doped a-Si films (2 microns thick) were then deposited onto the n^+ layer. A hole diffusion length of 0.5 μm has been observed in undoped a-Si films using the SPV technique.

An approach used to possibly improve the hole diffusion length, has involved light B-doping of the intrinsic layer. Depth profiling of the n^+/lightly B-doped i-layer films is shown in Figure 2-12. Phosphorous carry over to the i-layer was measured in the range of 5×10^{17} atoms/cm^3, the boron dopant concentration in the i-layer was found to be 8×10^{16} atoms/cm^3, and the oxygen concentration was approximately 3×10^{19} atoms/cm^3. The hydrogen content was between 10 to 14% of the Si concentration in the films (assuming a-Si concentration in the range of 10^{22} atoms/cm^3).

Surface photovoltage measurements require an accurate determination of the absorption coefficient. Two methods have been used to convert reflectance (R), and transmittance (T) to (n, k) in the range 1.8 eV < hv < 2.3 eV, where n and k represent the index of refraction and extinction coefficients, respectively. Both methods assume normal incident light on the four layer stack: air/a-Si:H/glass/air. Using the first method (Swanepoel method [5]), the n value is determined from the reflectance and transmittance extremes, and k is determined from the transmittance in the strong absorption regime ($4\pi kd/\lambda > 1$). A BASIC code is used to simplify the analysis. The method is accurate only when k << n. The second method (Paulick method [6]) uses a FORTRAN code "Index" to minimize the difference between the calculated R, T and (n, k) values and the measured R and T values. The accuracy of the resulting n value is limited by uncertainty in the reflectance measurement. However, k is insensitive to the error in the reflectance value which is measured in the strong absorption region.

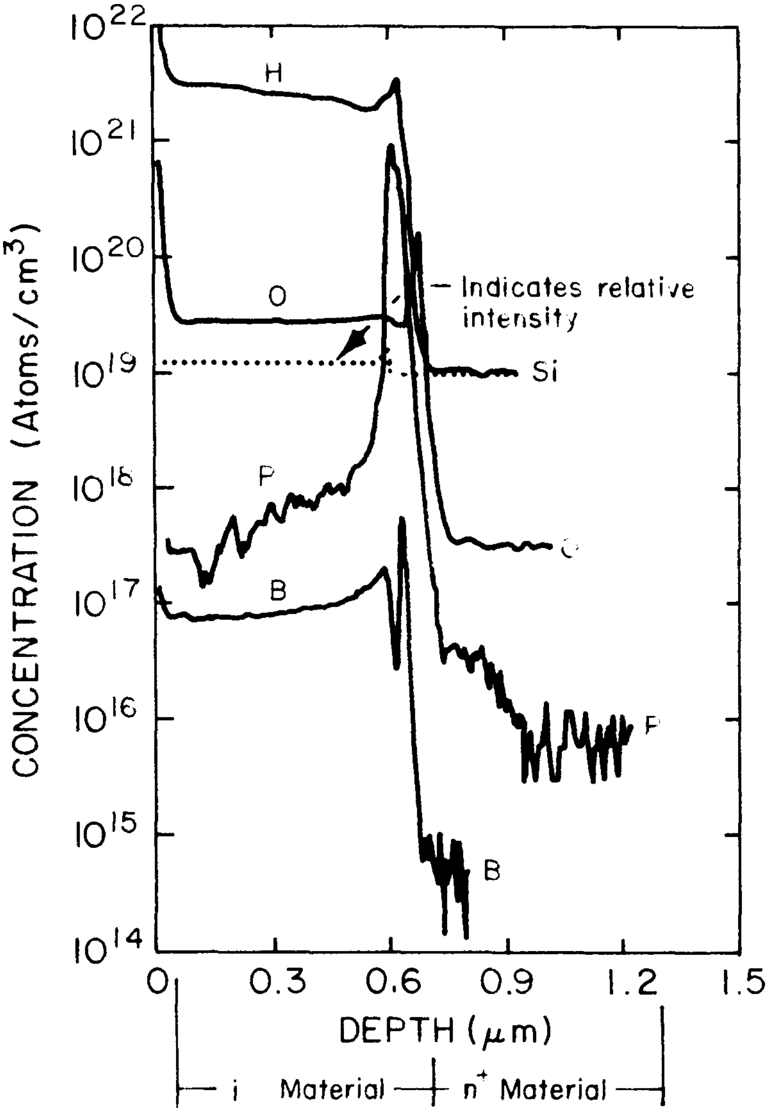

Figure 2-12. Depth Profiling Of n$^+$ (200 Å)/Lightly B-Doped i-Layer (2 µm On 7059 Glass)

The two methods agree well with the determination of k in the strong absorption region. A typical curve of the absorption coefficient ($\alpha = 4\pi k/\lambda$) versus hc/λ is shown in Figure 2-13. The low absorption coefficient was obtained using AC photoconductivity measurements. An absorption coefficient as low as 1 cm^{-1} has been obtained, as shown in Figure 2-14.

The SPV technique has been used to study the Staebler-Wronski effect. Two principle observations have been made: i) the diffusion length, L, decreases and saturates at 0.25 to 0.3 microns, and ii) the space charge width, W, decreases.

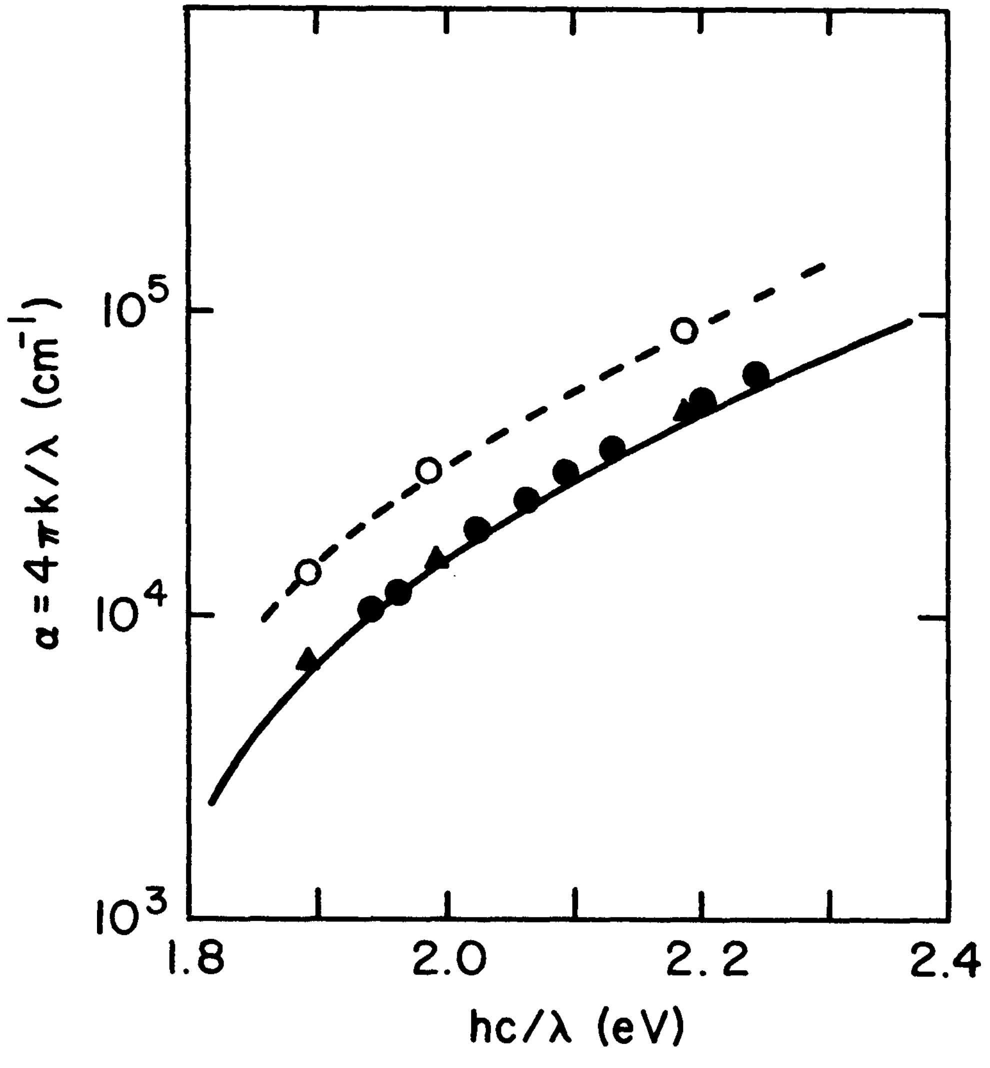

Figure 2-13. **Absorption Coefficient $\alpha = 4\pi k/\lambda$ Versus hc/λ**
The ●'s were obtained using the program "Index" for R and T data obtained from a lightly boron doped sample deposited in System Two at 250°C. The remaining data are from Reference 7, GD a-Si:H;
The ▲'s are 325°C substrate,
The o's are 420°C substrate,
(solid line) 200°C substrate.

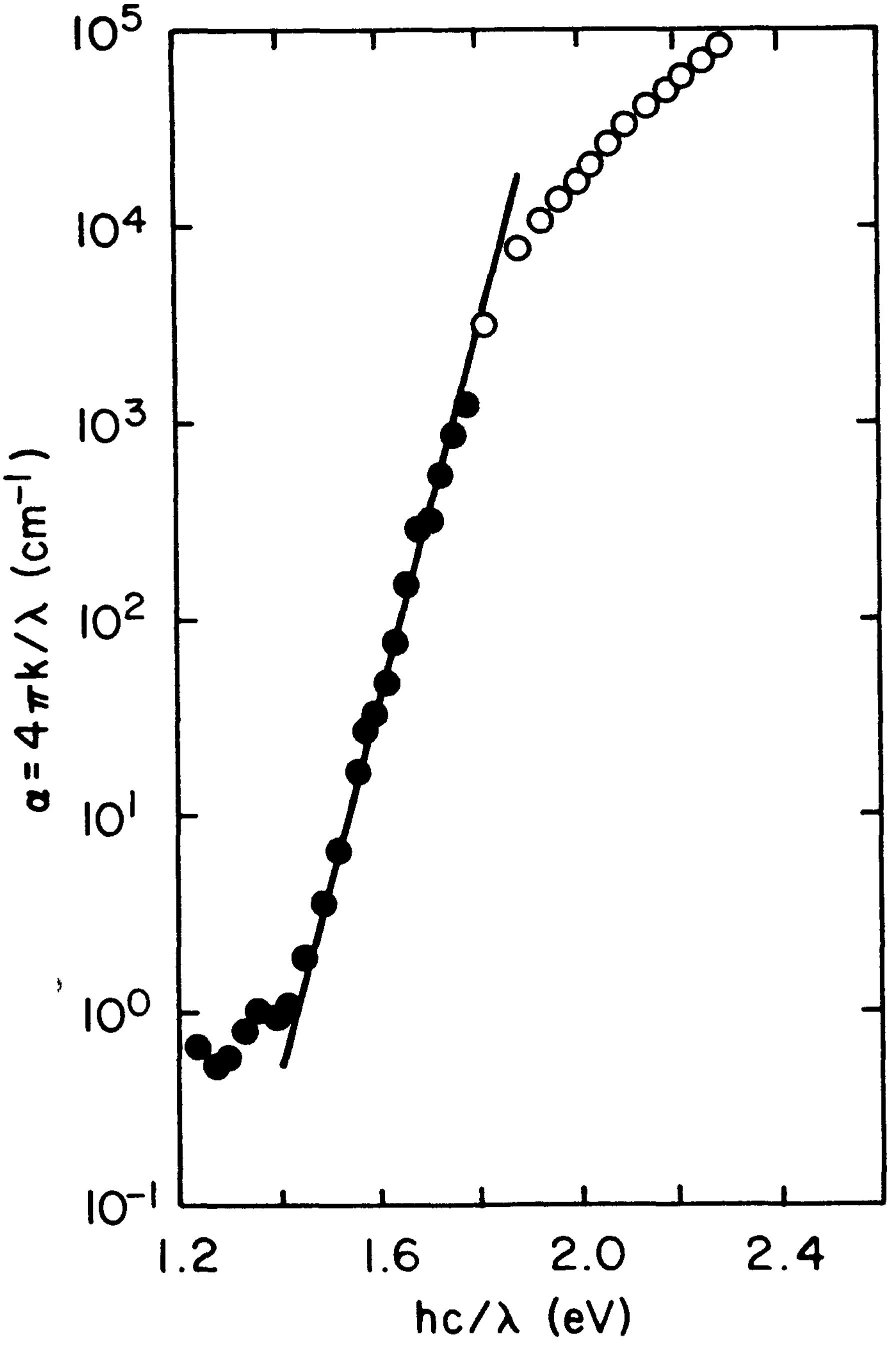

Figure 2-14. Absorption Coefficient $\alpha = 4\pi k/\lambda$ Versus hc/λ
Lightly doped a-Si:H from System Two. The data were acquired by sub-band gap photoconductivity normalized at 1.8 eV to α obtained from R, T. The slope of the solid line between 1.5 and 1.7 eV indicates that the density of gap states near the valence band edge has an approximate width of 45 meV.

Moore [8] has shown, using a regional approximation, that the relative photon flux intensity for a fixed surface photovoltage is:

$$I = \frac{\mathrm{const}\,(1/\alpha + L)(1 + V_\tau \mu_n / v_c F_1)}{(1/\alpha + L)(1 + V_\tau \mu_n / v_c F_2)F_2 - (1 + V_\tau \mu_n / v_c F_1)F_1(1/\alpha)\exp(-\alpha W)} \qquad \text{(Equation 2-1)}$$

where the Schottky formula for the barrier fields give:

$$F_1 = -\left[V_\tau / |E_0|\right]\left[\exp(-|E_0| W / V_\tau) - 1\right] ,$$

and

$$F_2 = -\left[V_\tau / |E_0| + \alpha V_\tau\right]\left\{\exp\left[(-\alpha - |E_0| / V_\tau)W\right] - 1\right\}$$

where:

W is the width of the space charge region near the Schottky contact,
$1/\alpha$ is the photon penetration depth,
E_O is the electric field at the interface $V_T \equiv KT$, and
L is the diffusion length.

When W collapses to zero, for instance under intense illumination conditions, Equation 1 reduces to the Goodman formula [9]:

$$I = \mathrm{const}\ (1/\alpha + L) \qquad \text{(Equation 2-2)}$$

Four samples were prepared in System Two; three samples were undoped, the fourth was doped at the level 0.5 ppm diborane.

The SPV measurement was performed in the constant photovoltage mode [8]. We assumed that Equation 2-2 is valid in order to determine an apparent diffusion length, L^*, from a plot of relative photon flux versus $1/\alpha$. The dependence of the apparent diffusion length upon dc bias light absorption F, was then measured. The bias light, which is passed through a 615 nm high-pass filter was varied through six decades of intensity up to a 2 AM1 equivalent level. Samples were studied in the annealed state and after increasing periods of light soaking at AM1.

The true diffusion length L was defined as the apparent diffusion length under dc red bias such that the carrier generation is equivalent to that produced by AM1 illumination. This is defined as 1 sun in the discussion that follows.

Figure 2-15(a) shows the relative photon flux versus 1/α for sample #3/18/85 (annealed) under zero sun and 1 sun bias illumination. The diffusion length is 0.46 μm and the large apparent diffusion length at zero sun indicates that W, the space charge width, is large.

After 400 hours of light stress on sample #3/18/85, L drops to 0.3 μm as shown in Figure 2-16.

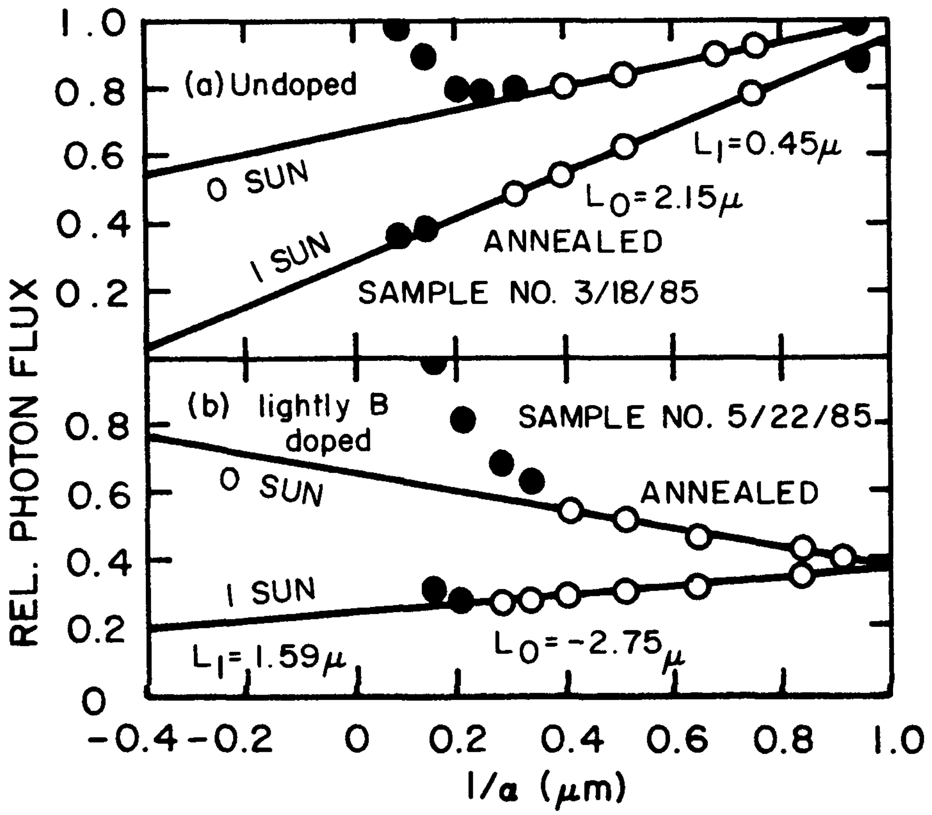

Figure 2-15. **Relative Photon Flux Versus 1/α For Annealed Samples At Different Illumination For Undoped And Lightly B-Doped Samples**

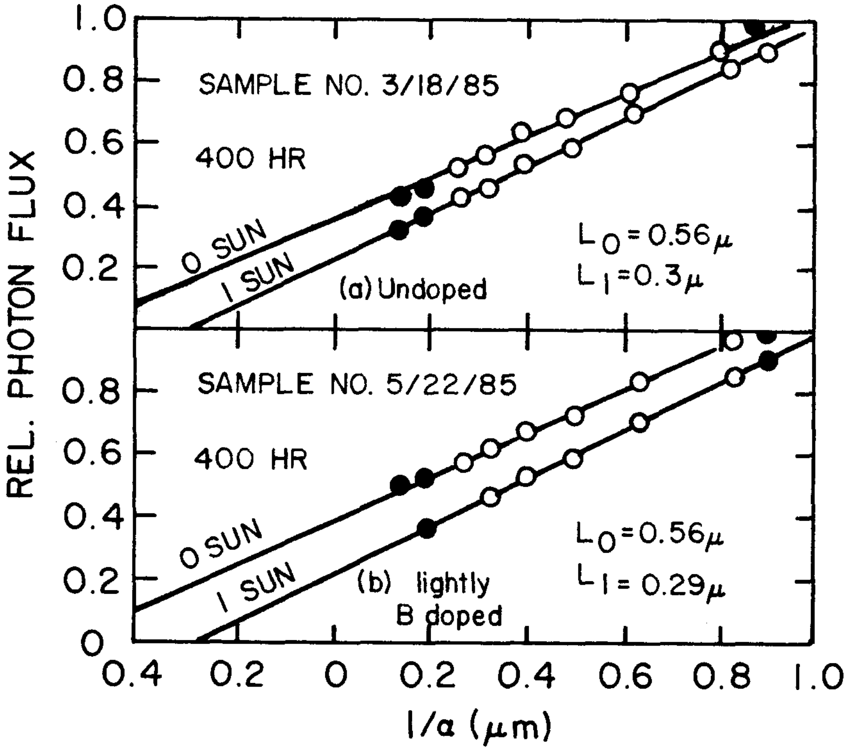

Figure 2-16. Relative Photon Flux Versus 1/α After 400 Hours Of Light Soaking

The diffusion length, for all samples studied converged between 0.25 and 0.3 μm and stabilized in that range (see Figure 2-17). In addition, it is evident in Figure 2-16 that L^*, at zero sun bias, converges toward L, which indicates that W has collapsed.

In Figure 2-18, the apparent diffusion length $L^*(F)$ versus the bias illumination are plotted for the annealed and light soaked states. After 400 hours, the undoped samples qualitatively approach a pattern containing two regions. For bias light flux greater than 0.0001 sun the apparent diffusion length varies only 20% over four decades of intensity. This behavior is consistent with the expected flux dependence of the carrier recombination lifetime [10, 11].

If the hole density is given by:

$$P \propto F^{\gamma} \qquad \text{(Equation 2-3)}$$

then, $L \propto F^{S} \qquad S \equiv (\gamma-1)/2$

where: γ is the exponent for sublinear photoconductivity [12]

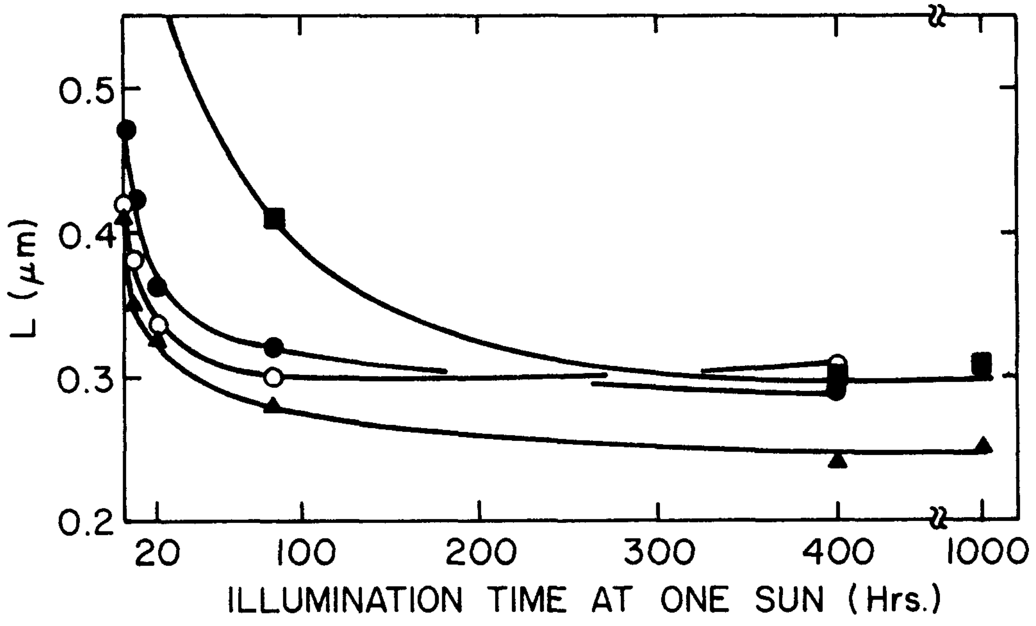

Figure 2-17. Diffusion Length Versus Light Soaking Time
The ■'s are boron-doped sample #5/22/85.
The ●'s are undoped #3/18/85.
The o's are undoped #3/13/85.
The ▲'s are undoped #4/16/85.

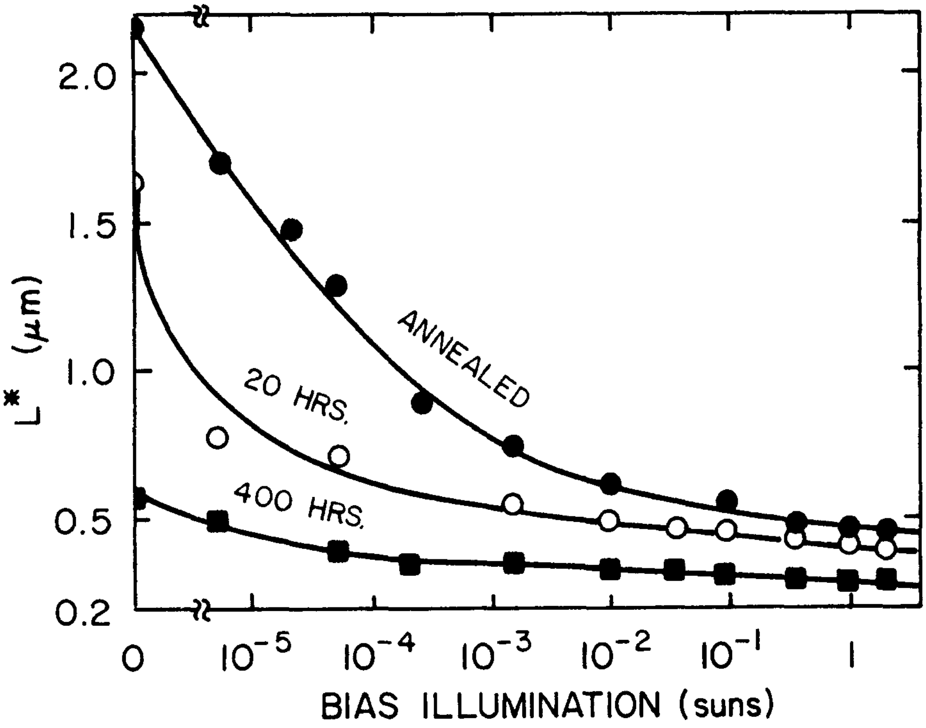

Figure 2-18. Apparent Diffusion Length Versus Bias Illumination For Annealed And Light Soaked States (Sample #3/18/85)

A measurement of $S \equiv -0.025$ (Figure 2-19) is in close agreement with the results of Moore and Kane [10] who have determined the flux dependence of L in annealed samples. The second region in Figure 2-18, flux < 0.0001 sun, is marked by a more rapid increase in L^* which is associated with the growth of the space charge region.

It is possible to quantitatively approximate the dependence of W upon flux intensity [8]. This is accomplished by inserting L into Equation 2-1, assigning an arbitrary value to W, and then calculating the $1/\alpha$ intercept, L^*. W is varied until the calculated value of L^* converges to the measured value. In Figure 2-20, W is plotted versus V_{oc} for sample #3/18/85. The data labeled 1 through 3 assume a fixed diffusion length defined in the normal manner. The data labeled 4 assume a flux dependent diffusion length as defined by Equation 2-3 with $S \equiv -0.025$. The space charge width determined by this analysis is reduced by at least 70% after 400 hours of light soaking, and the reduction is more severe if one assumes a flux dependent diffusion length. It is not yet known whether W stabilizes after 400 hours.

Figure 2-15(b) illustrates the relative photon flux versus $1/\alpha$ for annealed sample #5/22/85 under zero sun and 1 sun bias. Figures 2-18 and 2-21 show that there is considerably more dependence of L^* upon flux in the doped versus the undoped samples. Futhermore, L^* becomes negative at low illumination and appears to diverge positive at intermediate values of F. This point is evident on the 0, 5 and 20 hour-soaked states but not the 400 hour-soaked state. The behavior can be accounted for in Moore's model [13] by (-) charge trapping in the space charge layer at low illumination rather than the normal (+) charge that occurs in undoped samples. On the other hand, the 400 hour exposure produces data in quantitative agreement with that of the undoped sample. (Figure 2-19.) The metastable (+) trapping centers introduced by light soaking appear to overwhelm the (-) trapping centers associated with B-doping.

From these data it must be concluded that no advantage is gained with low density B-doping ($\simeq$ 0.5 ppm). The space charge width collapses and the diffusion length degrades to the same limits observed in the undoped samples.

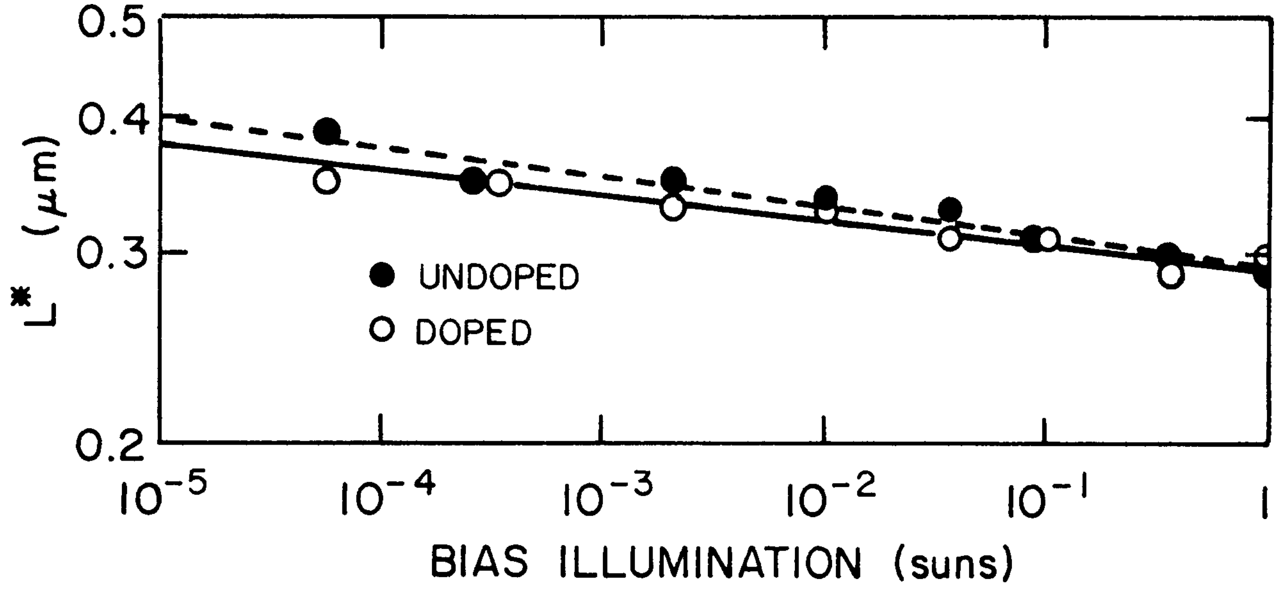

Figure 2-19. **Apparent Diffusion Length Versus Bias Illumination**
Sample #5/22/85
The o's are doped sample #5/22/85.
The ●'s are undoped sample #3/18/85.
The solid and dashed lines are fits to Equation 2-3 for the open circles and solid circles, respectively. The slopes of the lines are -.024 and -.026, respectively.

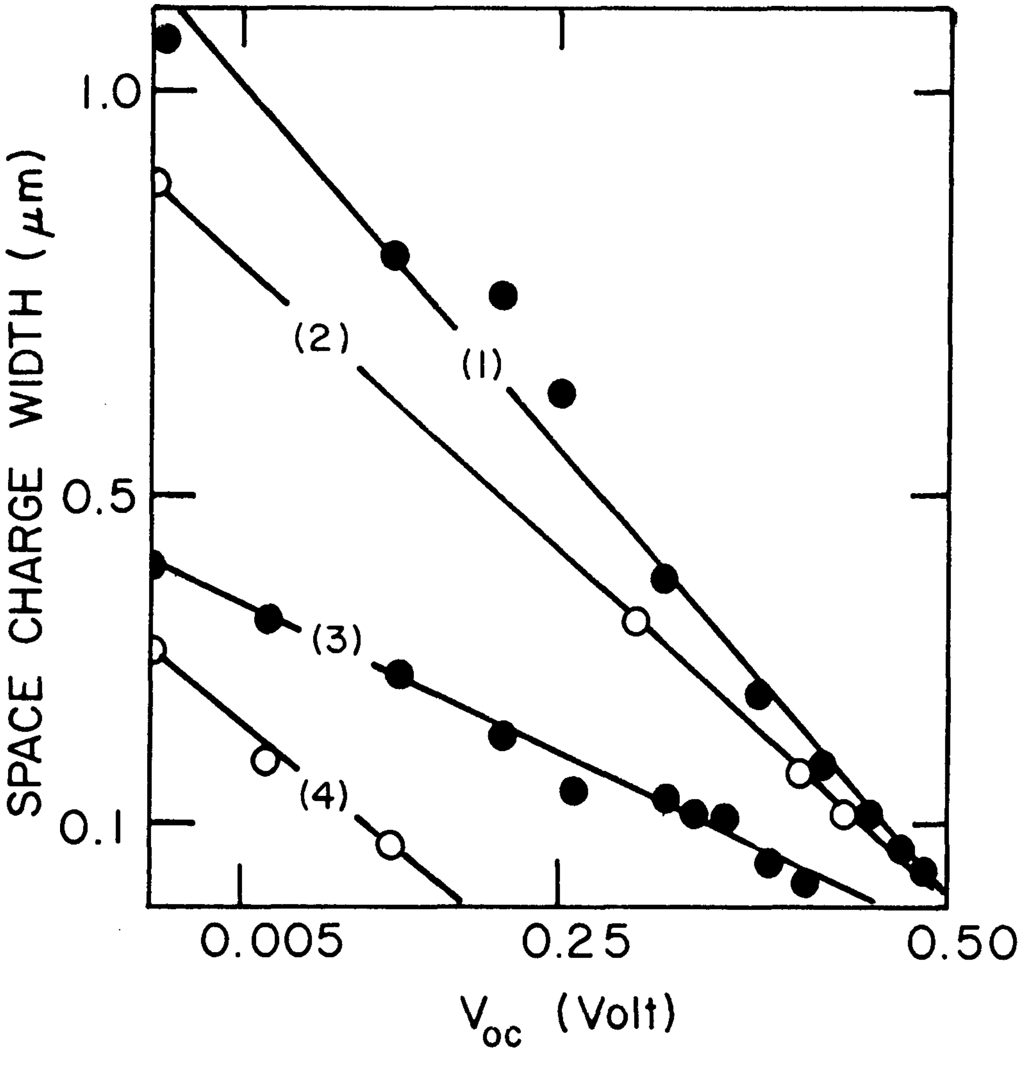

Figure 2-20. Space Charge W Versus V_{oc} For An Undoped Si Sample

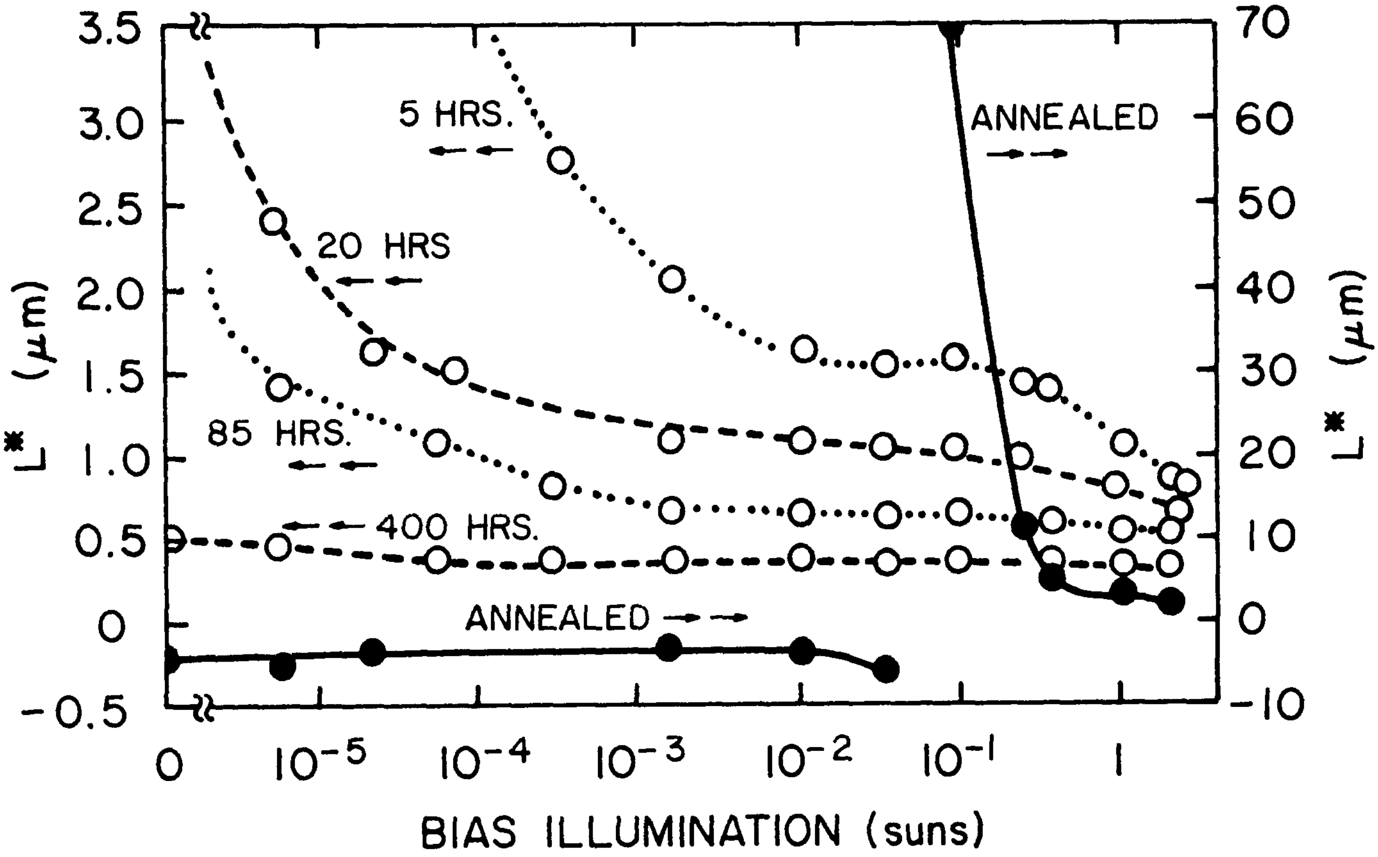

Figure 2-21. Apparent Diffusion Length Versus Flux Of Lightly B-Doped a-Si Films

The observations concerning the space charge layer are determined at V_{oc} conditions in an SPV measurement. Solar cells operate near V_{oc} conditions, therefore, the conclusions that are drawn concerning the built-in-field in an SPV measurement apply. L degrades approximately 40% with light exposure from 0.5 μm prior to exposure to 0.3 μm after exposure. The space charge width, which can be as large as 1 μm in the annealed state, degrades to less than 0.5 μm and under modest illumination to less than 0.2 μm. The results suggest that the reduction in the space charge width is responsible for the efficiency losses in a-Si p-i-n solar cells following prolonged light exposure.

The areas remaining to be addressed are: (i) the correlation of light-soaking effects on devices of different configurations and on the hole diffusion length of the intrinsic layer, and (ii) the correlation between $\mu\tau$ in the time-of-flight measurements and the hole diffusion length, especially for lightly B-doped samples, where some complicated factors are introduced in the SPV measurements due to space charge trapping in the bulk or at the surface. It has been found that a-Si samples with a boron concentration in the 10^{19} atoms/cm^3 range exhibit a reverse polarity in SPV measurements. It is believed that this anomalous phenomenon is due to negative space charge trapping. Therefore, SPV measurements on lightly P-doped samples are suggested to study the space charge polarity.

Surface photovoltage measurements will also be used to study the light-soaking effect on intrinsic a-Si films having different dopants such as fluorine, boron, and phosphorus compensated with boron.

2.1.2.4 Stability

To minimize the degradation in the conversion efficiency of a-Si solar cells, the light-induced effect was studied in lightly B-doped a-Si films. Intrinsic films were grown using 0.1 and 1 ppm diborane in the glow discharge gas mixture. An activation energy of 0.85 eV indicates that the Fermi level lies in the mid-gap region. The photocurrent was measured at 2 x 10^{-6} A and the ratio of light to dark current was 10^6. The SIMS profile shown in Figure 2-22 shows a boron concentration in the low 10^{19} range and a carbon concentration in the high 10^{19} range for B-doped films.

Figure 2-23 illustrates that light B-doping can reduce the photocurrent degradation. For an a-Si film grown from a gas mixture having 5 ppm diborane, the photocurrent decreased by 30% after two hours of AM1 illumination and then remained stable over the next 70 hours of illumination. The light current data returned to their original values after three hours of annealing at 160°C.

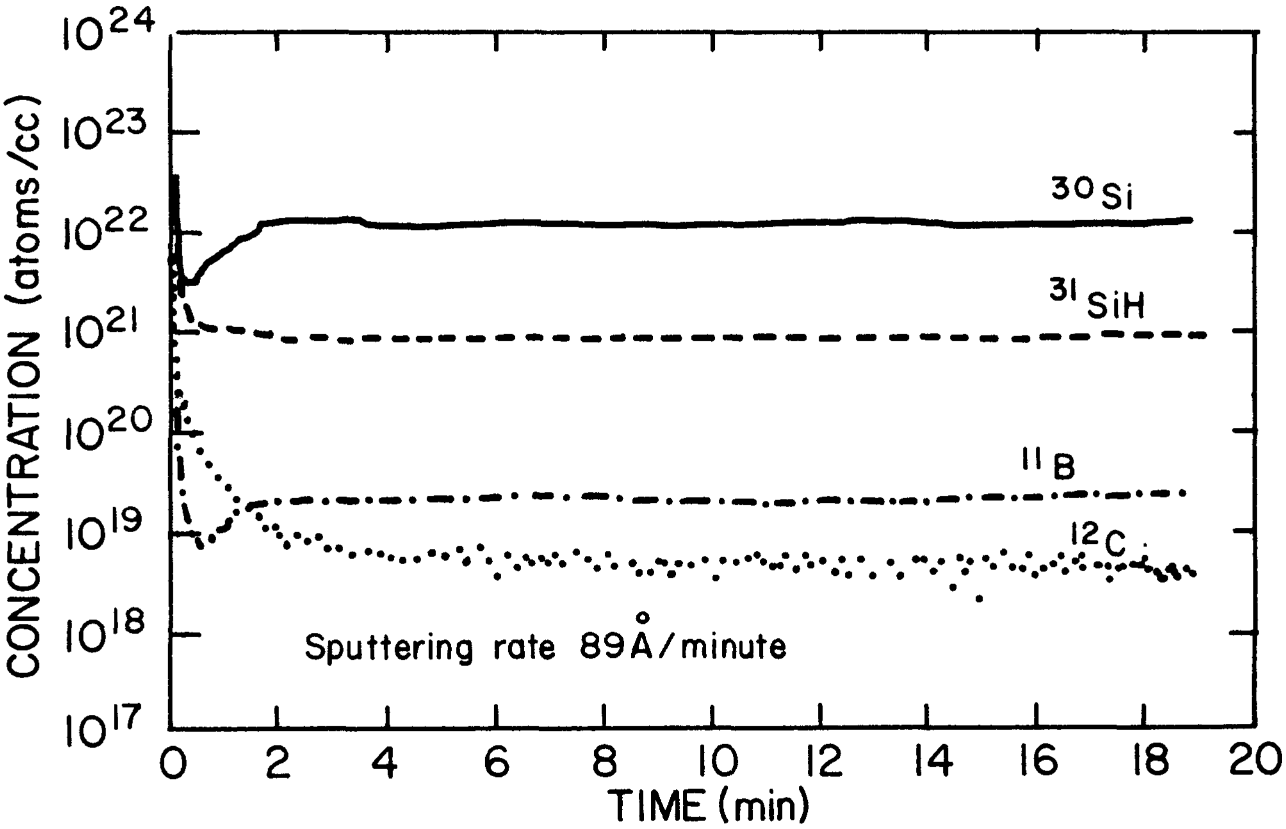

Figure 2-22. SIMS Profile Of Lightly B-Doped a-Si Films

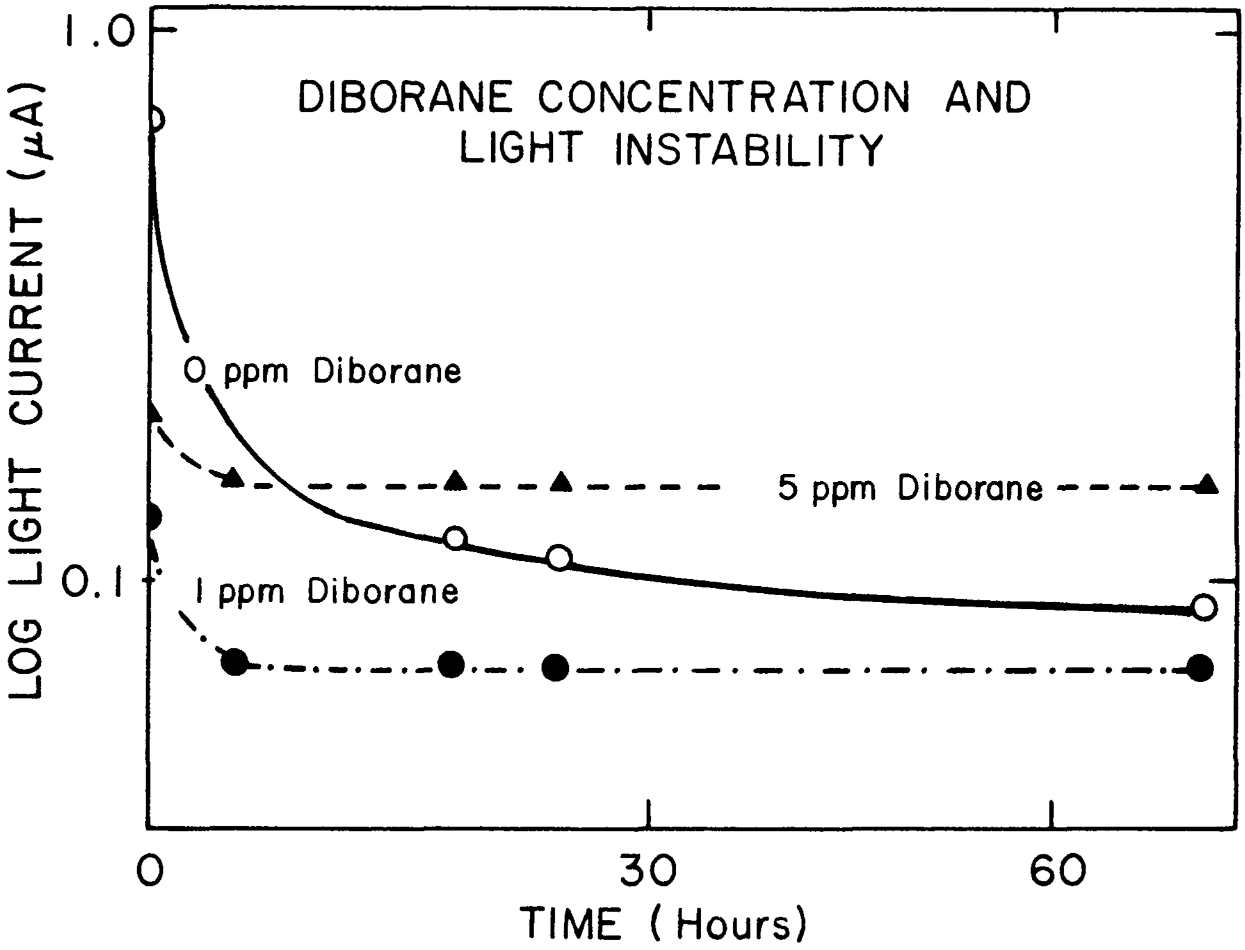

Figure 2-23. Diborane Concentration And Light Instability
The measurement parameters of the light current are: thickness = 0.5 μm, electrode separation = 1 mm, electrode width = 1 cm, voltage = 100 V.

The mechanism for the light B doping effect on the stability of a-Si films is not clearly understood. Boron could form B-H bonds thus decreasing the density of the Si-H bonds and/or pin the Fermi level to the mid-gap region. Investigations of these phenomena are progressing.

Other dopants such as fluorine, and phosphorous compensated with boron are being studied. Moreover, devices of different configurations including polyimide/Ni/p-i-n/ITO, and polyimide/Ni/n-i-p/ITO with different dopants in the intrinsic layer will be prepared, and the p^+/i and i/n^+ interfaces as well as the device stability will be studied.

Electron spin resonance (ESR) was initiated on a-Si:H material to study the variation of spin concentration with illumination. Powder samples were collected from shower heads, and from films deposited on glass and polyimide substrates. Future work may expand into films deposited on quartz substrates, observed in-situ, and films deposited on aluminum substrates--removed as flakes and powders. In this manner, the effects that different deposition substrates have on ESR signals may be examined and compared.

Relative to powders, the ESR work has established that an increase in the dangling bond signal occurs with light soaking and a corresponding decrease in the signal occurs with thermal annealing. Light-induced ESR (LESR) has also been used to observe powder samples at 77°K. A typical LESR signal is shown in Figure 2-24. The ESR signal increases with light exposure, and the contribution of the high field is larger, (asymmetrical) while the g value becomes smaller. This is in general agreement with published LESR results [14]. Since these are powder samples, the illumination is very likely non-uniform. Also, the relative effect of the increased surface dangling bond states with powder samples is unknown.

For some of the powders which were analyzed, as shown in Figure 2-25, an anomalous background has been observed. A similar effect was also observed by Lowry at Iowa State/Ames Laboratories [15]. The cause of this phenomenon has not been established. Contamination by foreign magnetic impurities has been suspected, but not detected thus far. The analysis of a-Si coated polyimide substrate samples has concentrated on achieving a baseline value for the dangling bond signal.

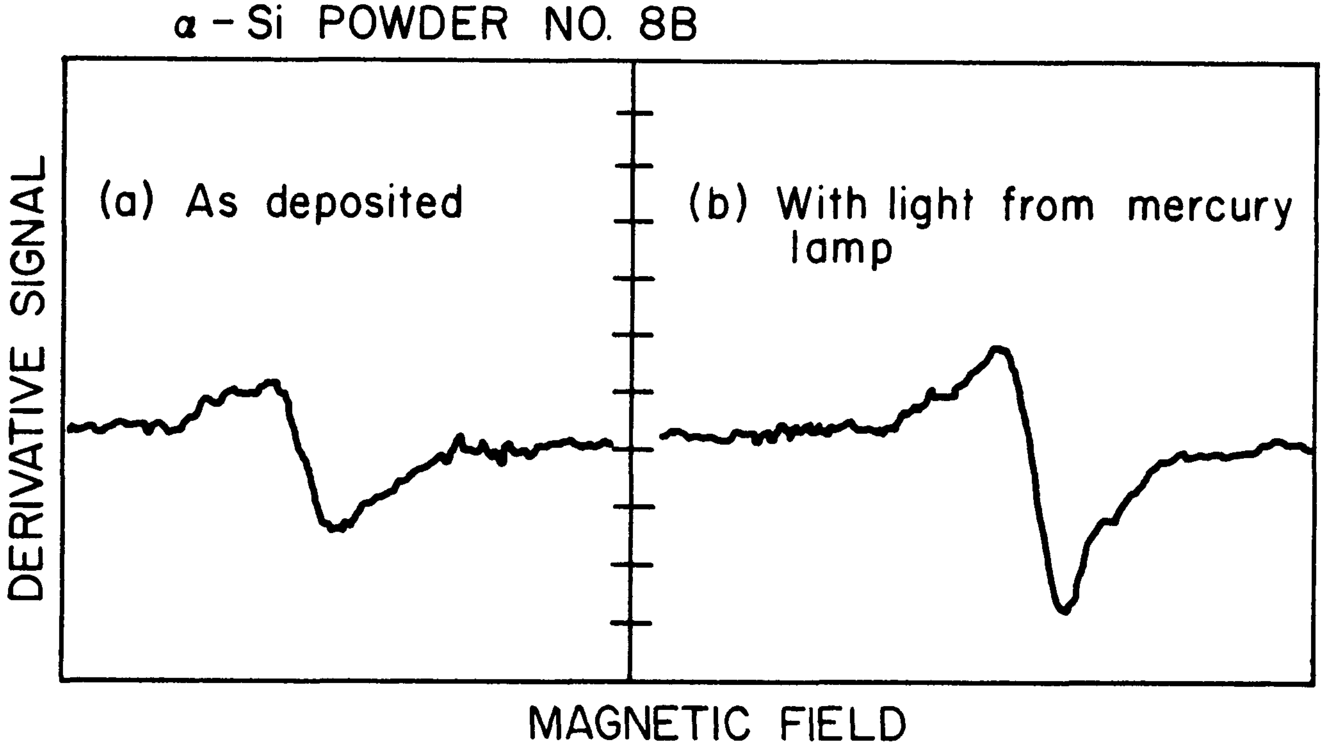

Figure 2-24. Light-Induced ESR (LESR) Of a-Si Films

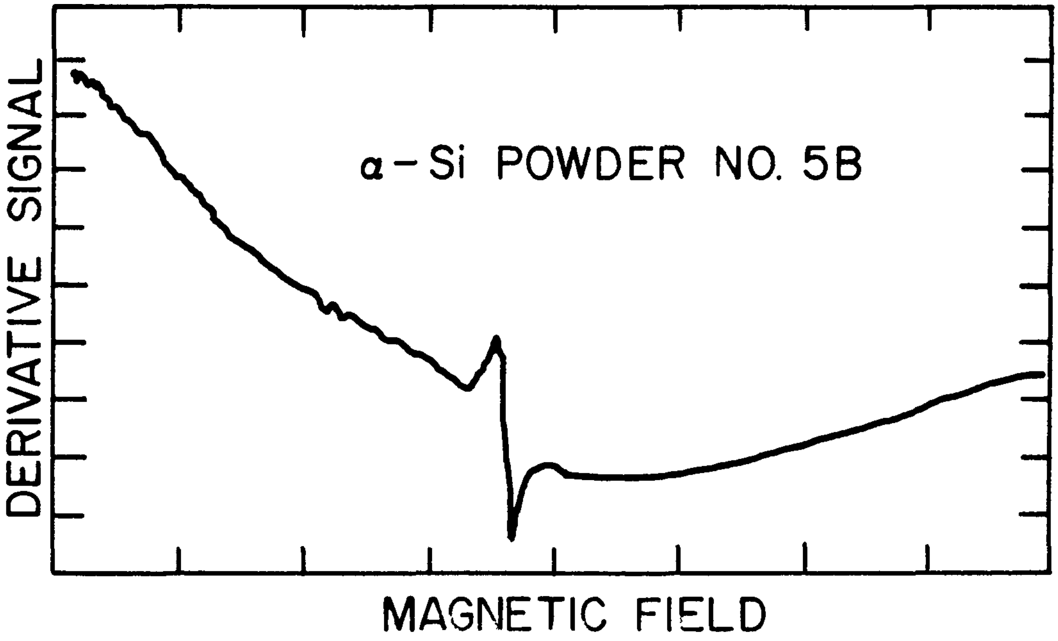

Figure 2-25. An Anomalous Background Was Observed In ESR On Powders

Bare polyimide material has a dangling bond signal at the g = 2 position, which is very similar to that for a-Si coated polyimide material. The a-Si signal can be obtained by subtracting the bare polyimide signal from the a-Si coated polyimide substrate signal. To reach the baseline, a baking time of greater than 100 hours at 170°C is necessary. The signal is presumably related to water in the polyimide substrate, and to the reduction in the water content realized with baking, which drives out adsorbed and chemisorbed waters. Typically, baking has been done in air at 170°C, as seen in Figures 2-26 and 2-27, for flat polyimide substrates of both Vendors A and B, respectively. However, two rolled polyimide substrates (Vendor A) coated with a-Si showed a decrease followed by an increase in signal with baking time in air as shown in Figure 2-28. Amorphous silicon on rolled polyimide substrate of Vendor B did not show the increase (Figure 2-29). Also, this a-Si coating thickness of 0.8 μm was intermediate between the thicknesses of the films on the Vendor A polyimide, which were 1.44 μm and 0.32 μm, respectively. It should be noted that a-Si on the flat polyimide substrate material of Vendors A and B shows a decrease in signal with baking time.

Presumably, heating the polyimide reduces the stress within the a-Si film on the rolled polyimide. The thicker polyimide substrate (Vendor A) exerts more force on the a-Si film. In any case, the columnar structure of the a-Si film may "open up," admitting more O_2 from the air. Oxygen is paramagnetic and may add to the dangling bond signal. Stress due to the difference in the thermal coefficients of the Vendor A and Vendor B polyimides may be ruled out because both polyimides have similar thermal coefficient values. These heating experiments will be repeated, but with the baking done under vacuum or in a N_2 gas atmosphere and then compared with the observations made when baking in air. If no differences are observed, the source of the change in the dangling bond signal will not be attributed to the atmosphere (O_2), but rather to the polyimide or a-Si films.

Studies of the effects of light intensity and light wavelength on LESR are progressing.

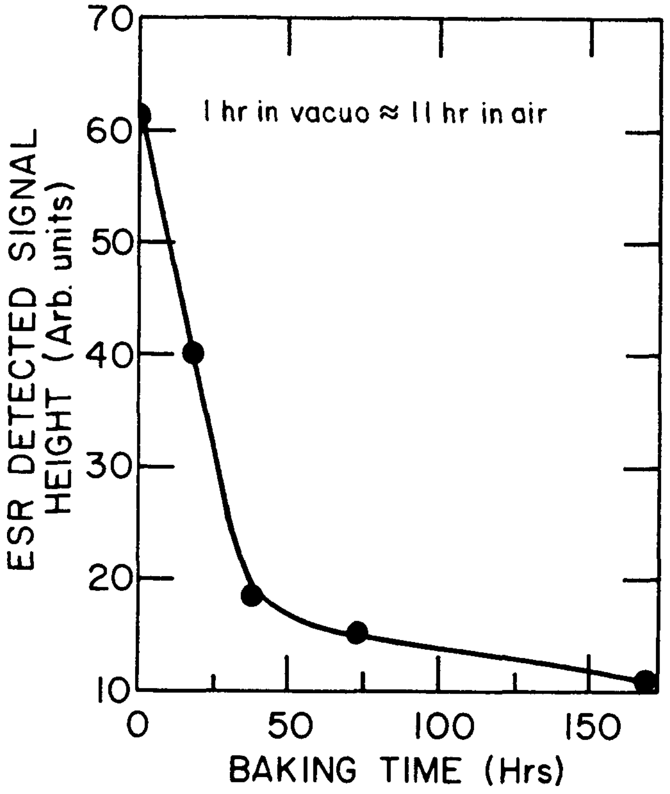

Figure 2-26. Baking Effect On The Bare Polyimide Substrate, Rolled (Vendor A)

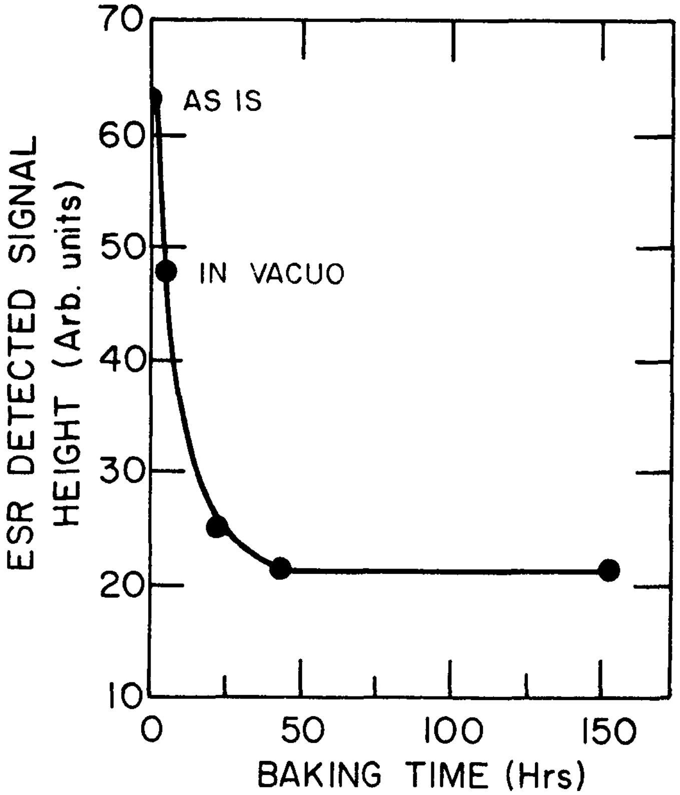

Figure 2-27. Baking Effect On The Bare Polyimide Substrate, Rolled (Vendor B)

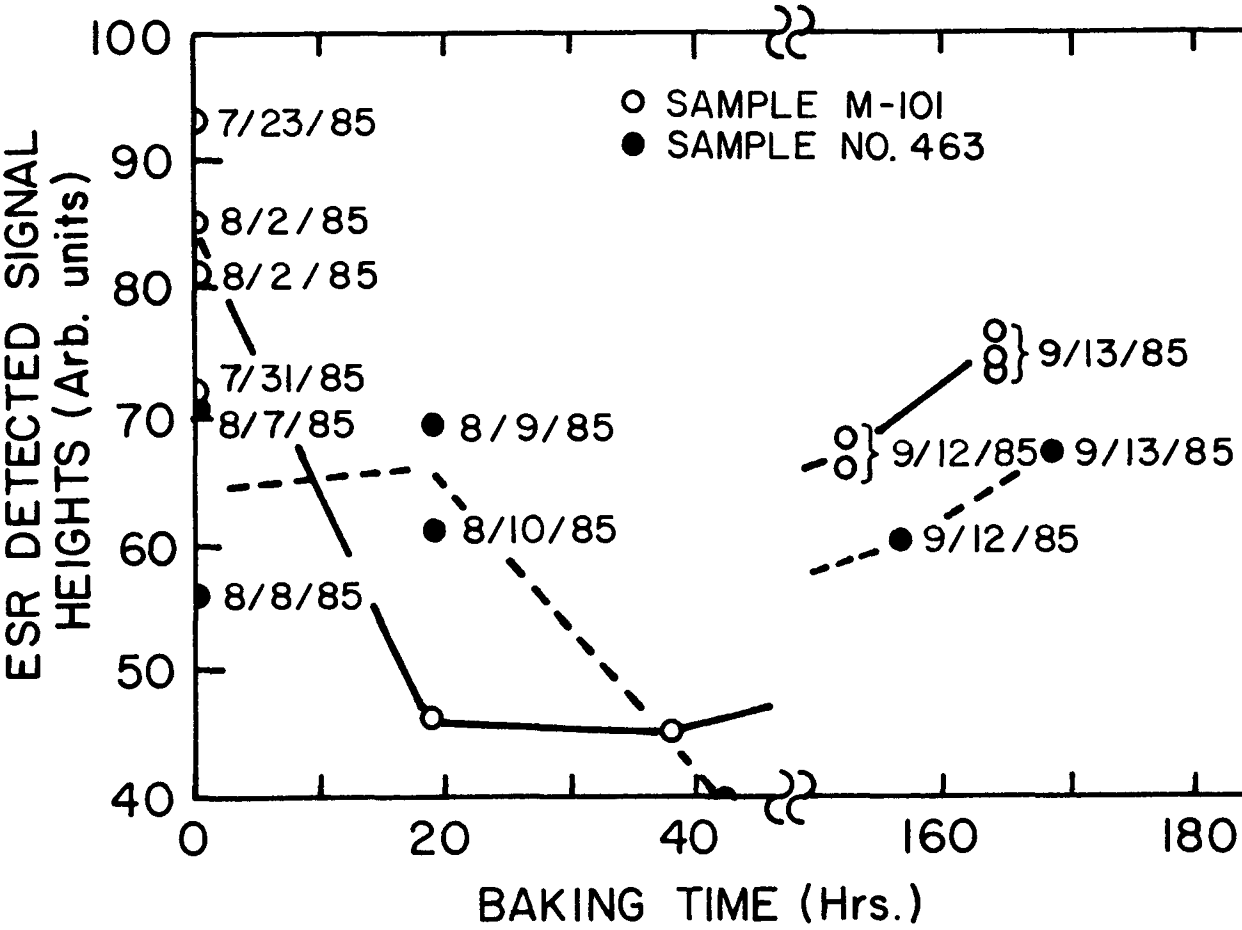

Figure 2-28. Baking Effect On a-Si:H/Polyimide Substrate (Vendor A)

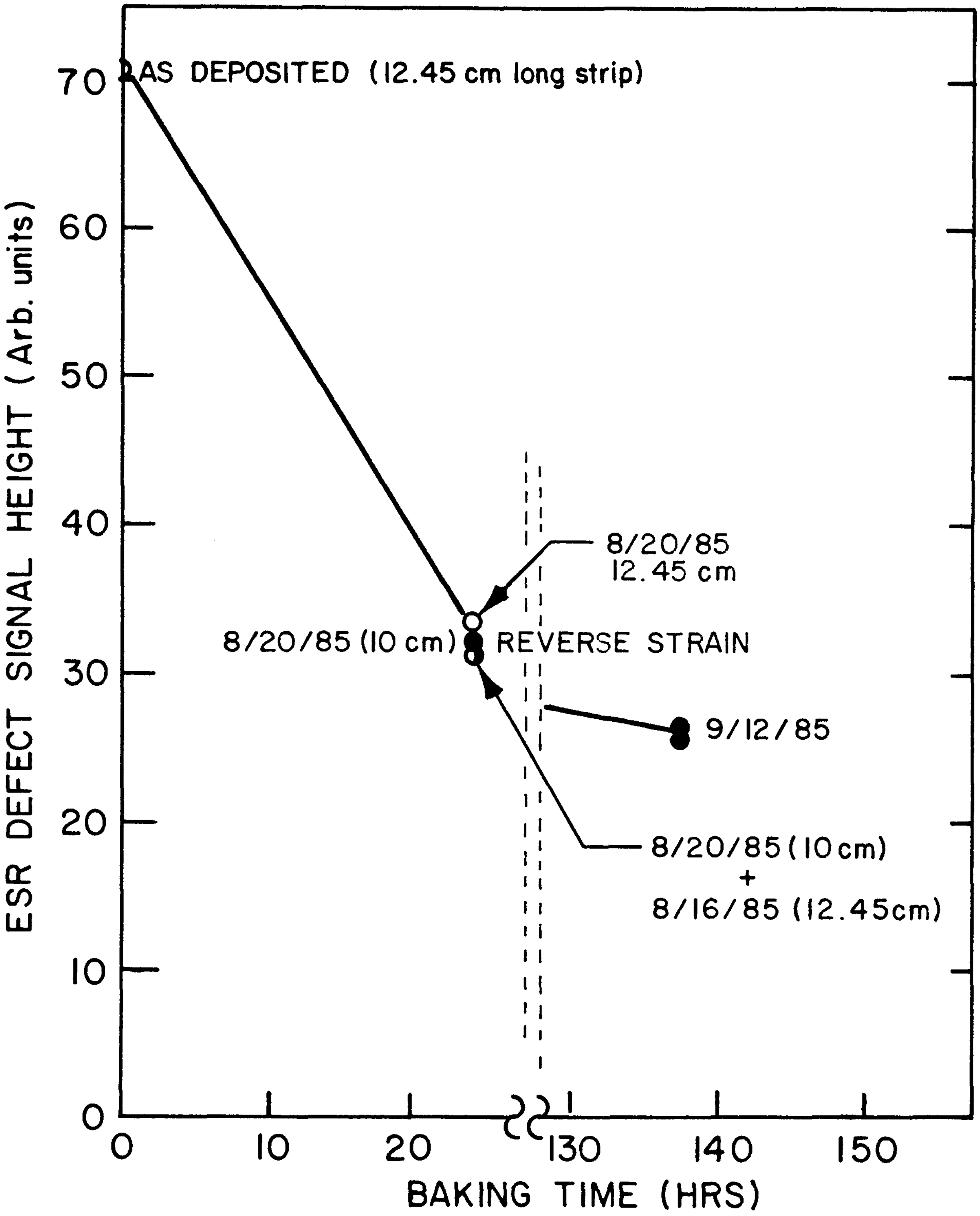

Figure 2-29. Baking Effect On a-Si:H/Polyimide Substrate (Vendor B)

Typical defect densities of $2 \times 10^{16}/cm^3$ for powders and $6 \times 10^{15}/cm^3$ for a-Si films have been measured in the thermally annealed state. Typically, the increase in defect densities with light soaking are 40-60% for powder samples.

2.1.3 p^+ Amorphous SiC:H

A series of systematic investigations involving a-SiC:H films have been performed by plasma decomposition of silane and methane gas mixtures. p^+ a-SiC:H has been optimized for different CH_4/SiH_4 ratios and B_2H_6 concentrations. A band gap, between 1.8 eV and 2.25 eV, can be controlled. SIMS analysis indicates a carbon concentration ranges between 8 and 14%. The optimized values exhibit a band gap of 1.86 eV, an activation energy of 0.4 eV, a dark conductivity of 1×10^{-4} (ohm cm)$^{-1}$, an index of refraction of 3.3, and a deposition rate of 10.6 Å/second. This high deposition rate was achieved with virtually no dust formation. As shown in Figure 2-30, optical gap, activation energy, and deposition rate vary linearly with the RF power. A deposition rate of 14.2 Å/second, a band gap of 2.08 eV, and an activation energy of 0.58 eV were obtained using an RF power of 15W. Pure SiH_4, CH_4/SiH_4 = 50/50 and $B_2H_6/SiH_4 = 3 \times 10^{-4}$ were used in this experiment. Figure 2-31 illustrates the power dependence on the dark conductivity. Using an RF power of 10W films having a maximum conductivity of 6×10^{-6} (ohm cm)$^{-1}$ were produced.

The effect of the boron concentration (by changing the B_2H_6/SiH_4 ratio) on the electrical properties and the deposition rate of p^+ a-SiC:H films were studied. The optical gap and activation energy values decrease with increasing B_2H_6/SiH_4 ratios. As shown in Figure 2-32, the optical gap and the activation energy varied from 2.08 eV (0.583 eV at $B_2H_6/SiH_4 = 3 \times 10^{-4}$) to 1.86 eV (0.4 eV at $B_2H_6/SiH_4 = 4 \times 10^{-3}$) respectively. The corresponding dark conductivity increased linearly from 1.95×10^{-8} (ohm cm)$^{-1}$ to 1×10^{-4} (ohm cm)$^{-1}$, as shown in Figure 2-33.

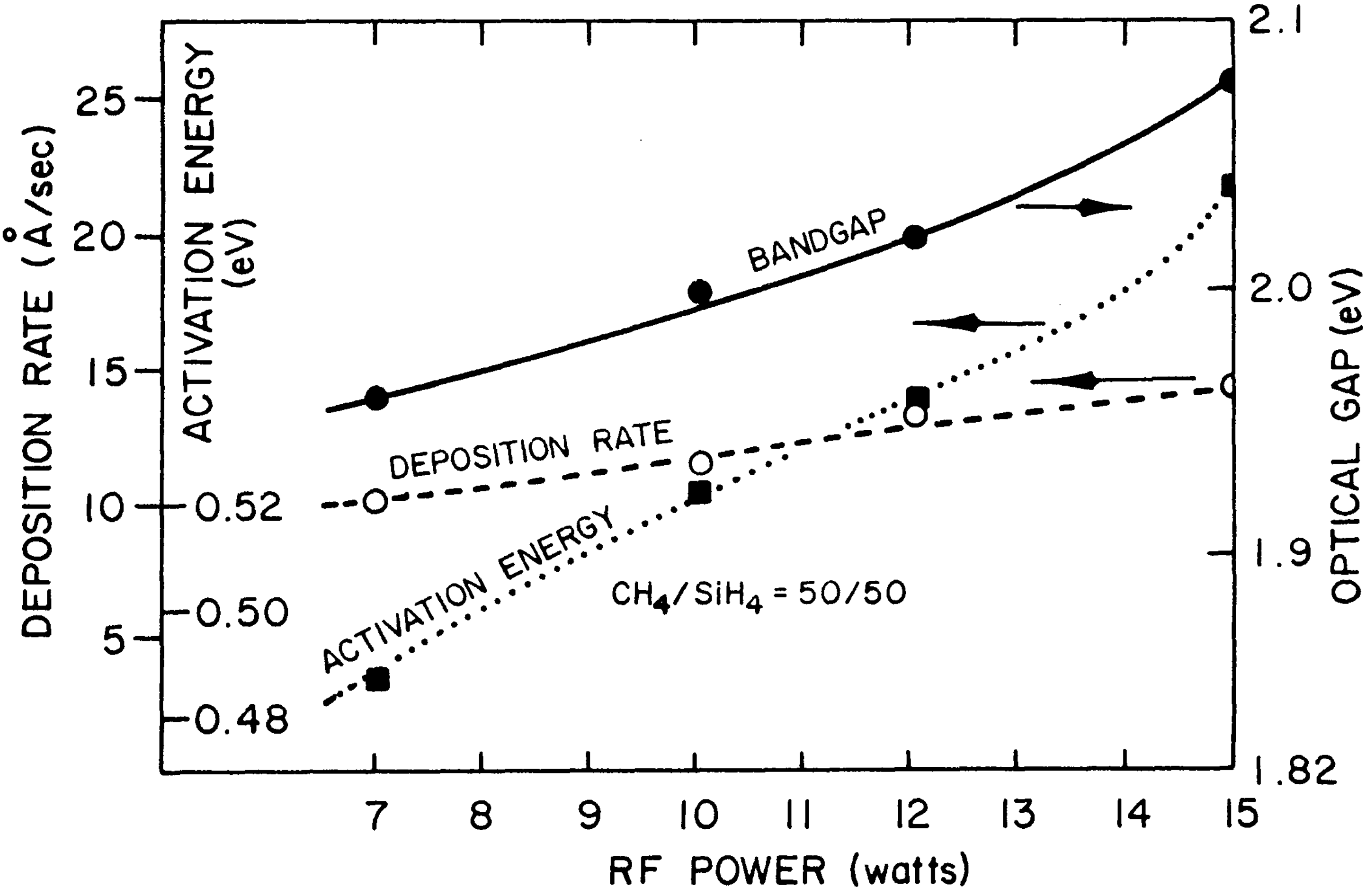

Figure 2-30. Optical Gap, Activation Energy And Deposition Rate As A Function of Power

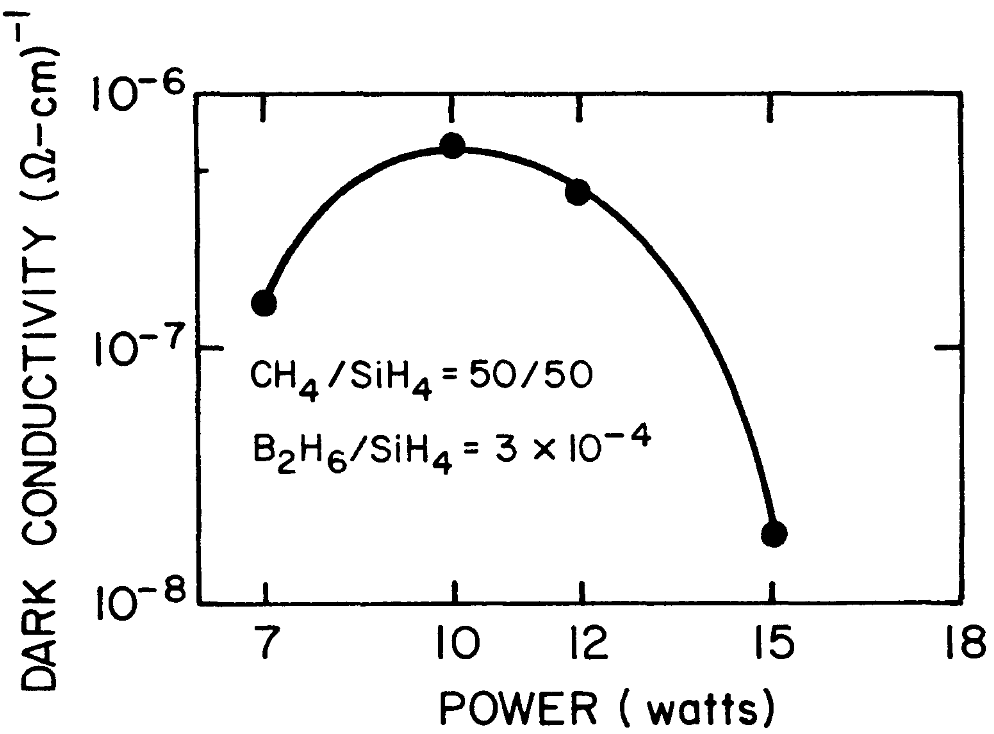

Figure 2-31. Power Dependence Of The Dark Conductivity Of p^+SiC:H

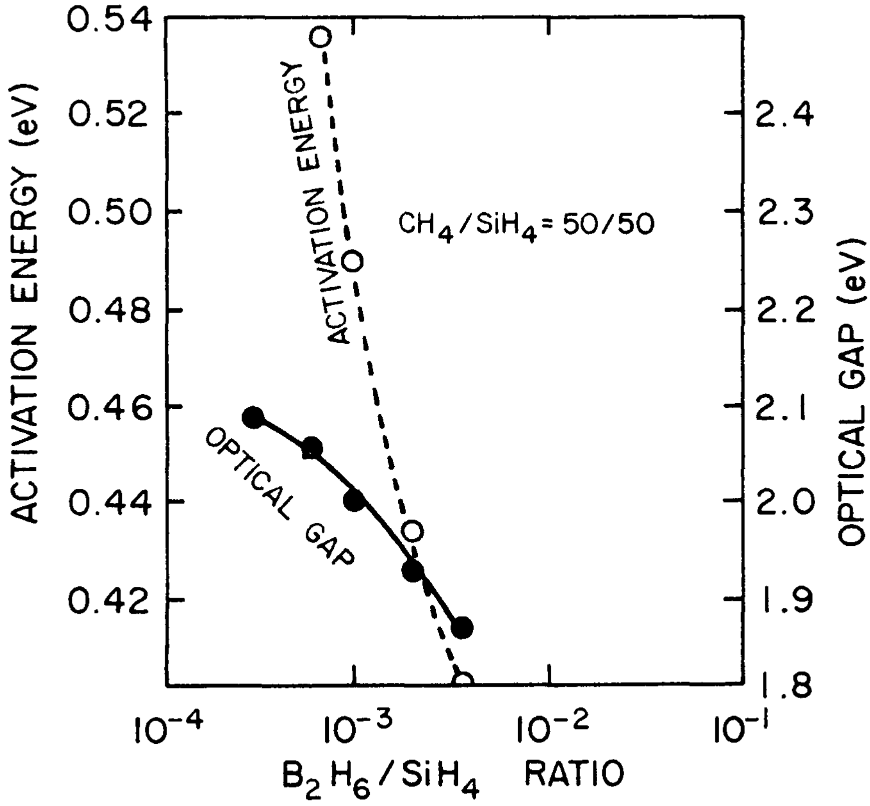

Figure 2-32. Optical Gap And Activation Energy As A Function Of B_2H_6/SiH_4 Ratio

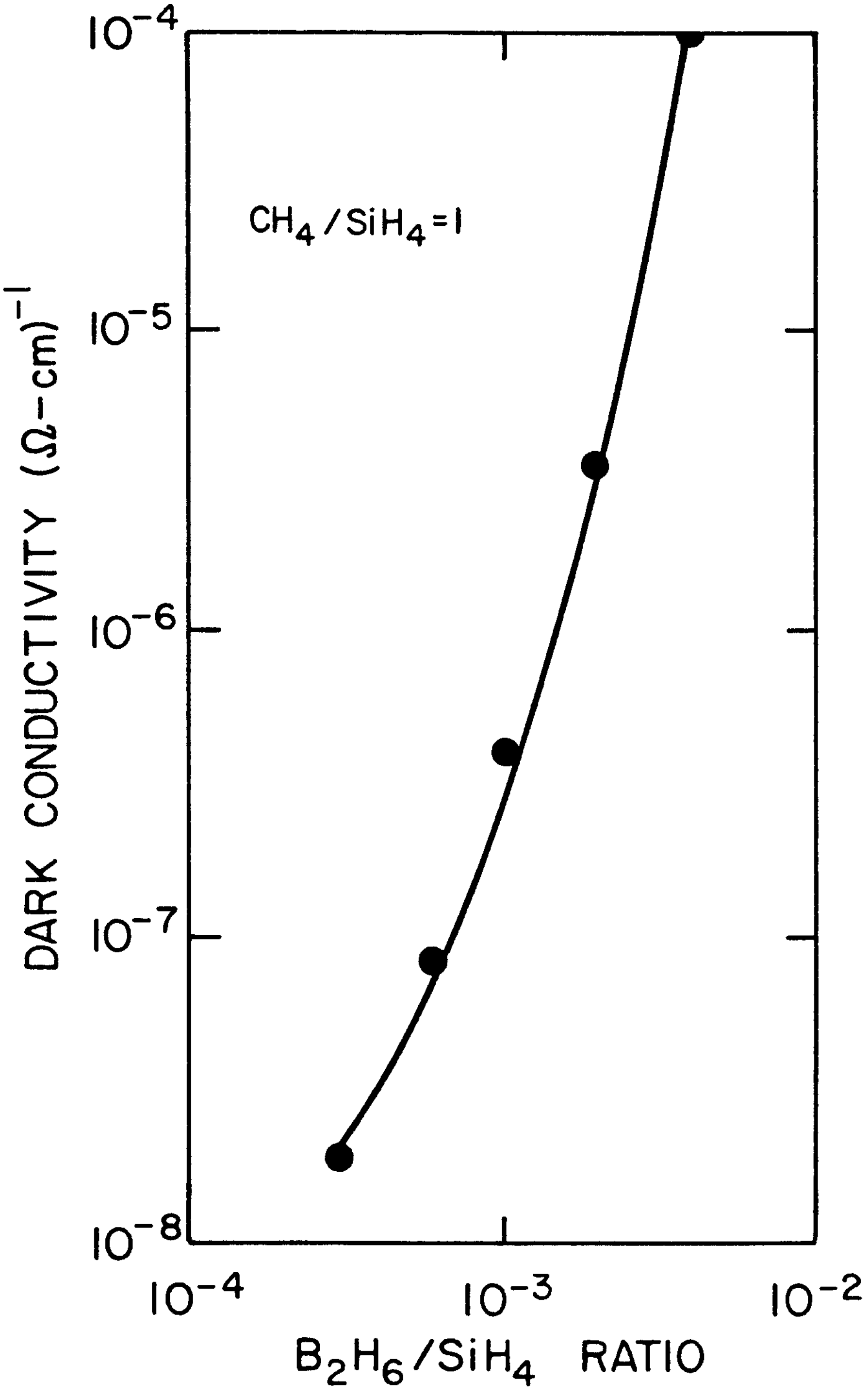

Figure 2-33. Conductivity Of p^+SiC:H As A Function Of B_2H_6/SiH_4 Ratio

At a CH_4/SiH_4 ratio of 50/50, the deposition rate decreased with increasing B_2H_6/SiH_4 gas ratios, as shown in Figure 2-34. The rate decreased to 10.6 Å/second using a B_2H_6/SiH_4 ratio of 4×10^{-3}.

The index of refraction varies linearly between of 3.0 and 3.3 at $\lambda = 530$ nm, with power and B_2H_6/SiH_4 ratios, as shown in Figure 2-35. The variation in the dark conductivity, photoconductivity, and deposition rate with the CH_4 fraction is shown in Figure 2-36. Both dark and photoconductivity decrease with increasing CH_4 fractions. This is due to an increase in the optical gap and activation energy, as illustrated in Figure 2-37. A peak in the deposition rate versus the CH_4 fraction has been observed.

The IR spectra of p^+ a-SiC:H for different ratios of CH_4/SiH_4 was also studied. For reference purposes the IR spectrum of undoped a-Si film was measured, as shown in Figure 2-38. Bond stretching at 2000 cm^{-1} and a bond rocking at 630 cm^{-1} for the Si-H structural group were observed. The IR spectra of p^+ a-SiC:H films made with different CH_4/SiH_4 ratios are shown in Figure 2-39. From this figure, it was observed that absorptions in the 860 to 890 cm^{-1} band, which is assigned to SiH_2 or $(SiH_2)_n$, is associated with carbon incorporation. Also it was seen that carbon promotes silicon dihydride bonds in the amorphous network. Carbon is incorporated as methyl ($-CH_3$) groups in the a-Si network and the amount of ($-CH_3$) groups increases with increasing CH_4/SiH_4 ratios in the gas phase.

n^+ SiC:H films were also produced but it was observed that P doping is more effective than B doping. The existence of good photoconductivity values of $\sigma_L = 10^{-4}$ $(\text{ohm cm})^{-1}$ for both n^+ and p^+ material, and a wide band gap of 1.92 to 2.0 eV in the glow discharge produced a-SiC:H films indicate a good candidate material for window layers. Evaluation of this material, both p^+ type and n^+ type, for use in p-i-n and n-i-p a-Si solar cells is in progress. The advantage of the p^+ SiC:H window layer in p-i-n structures is that it gives a higher current due to more light collected in the blue region. The p^+ SiC:H window layer also gives a higher V_{oc} due to the increased built-in potential. In addition, p^+ SiC:H adjacent to the ITO can reduce the effects of indium diffusion because indium is an acceptor in a-Si. n^+ SiC:H can also be used as a window layer in n-i-p structures.

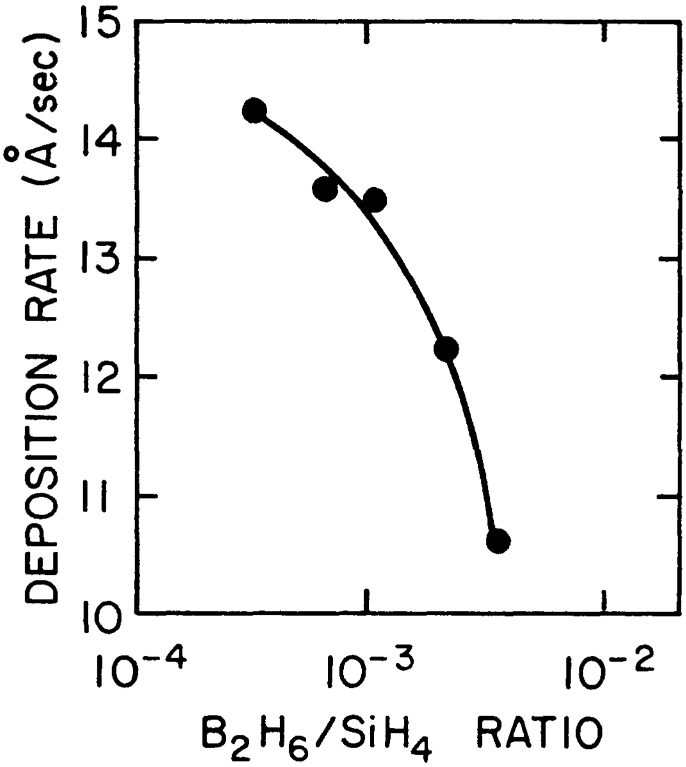

Figure 2-34. Deposition Rate As A Function Of B_2H_6/SiH_4 Ratio

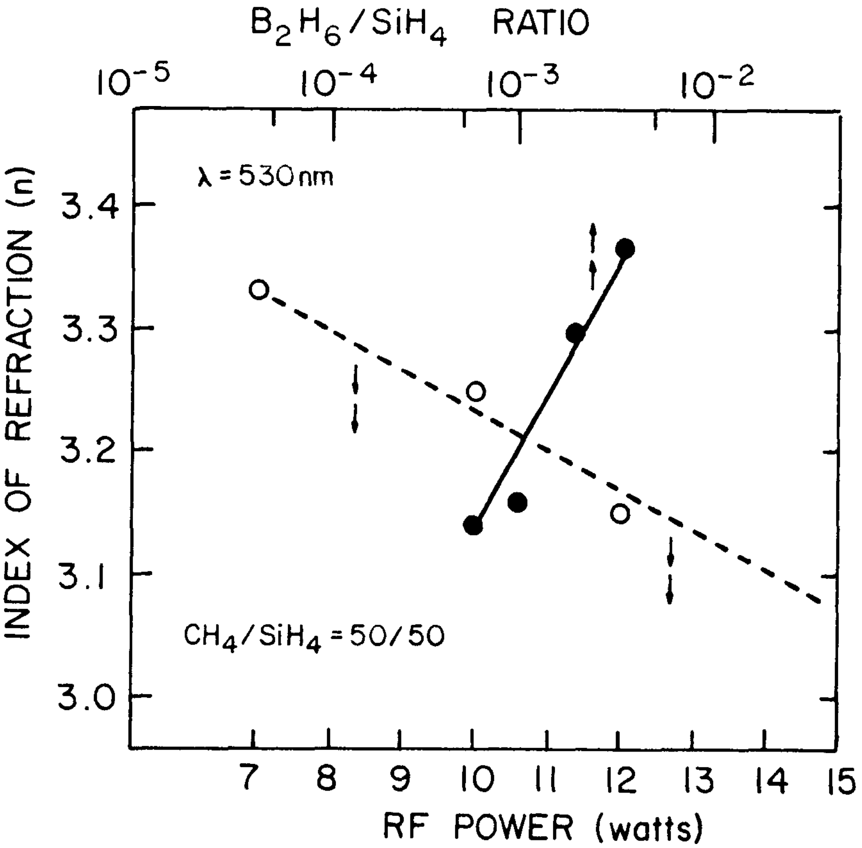

Figure 2-35. Dependence Of Index Of Refraction On Power And B_2H_6/SiH_4 Ratios

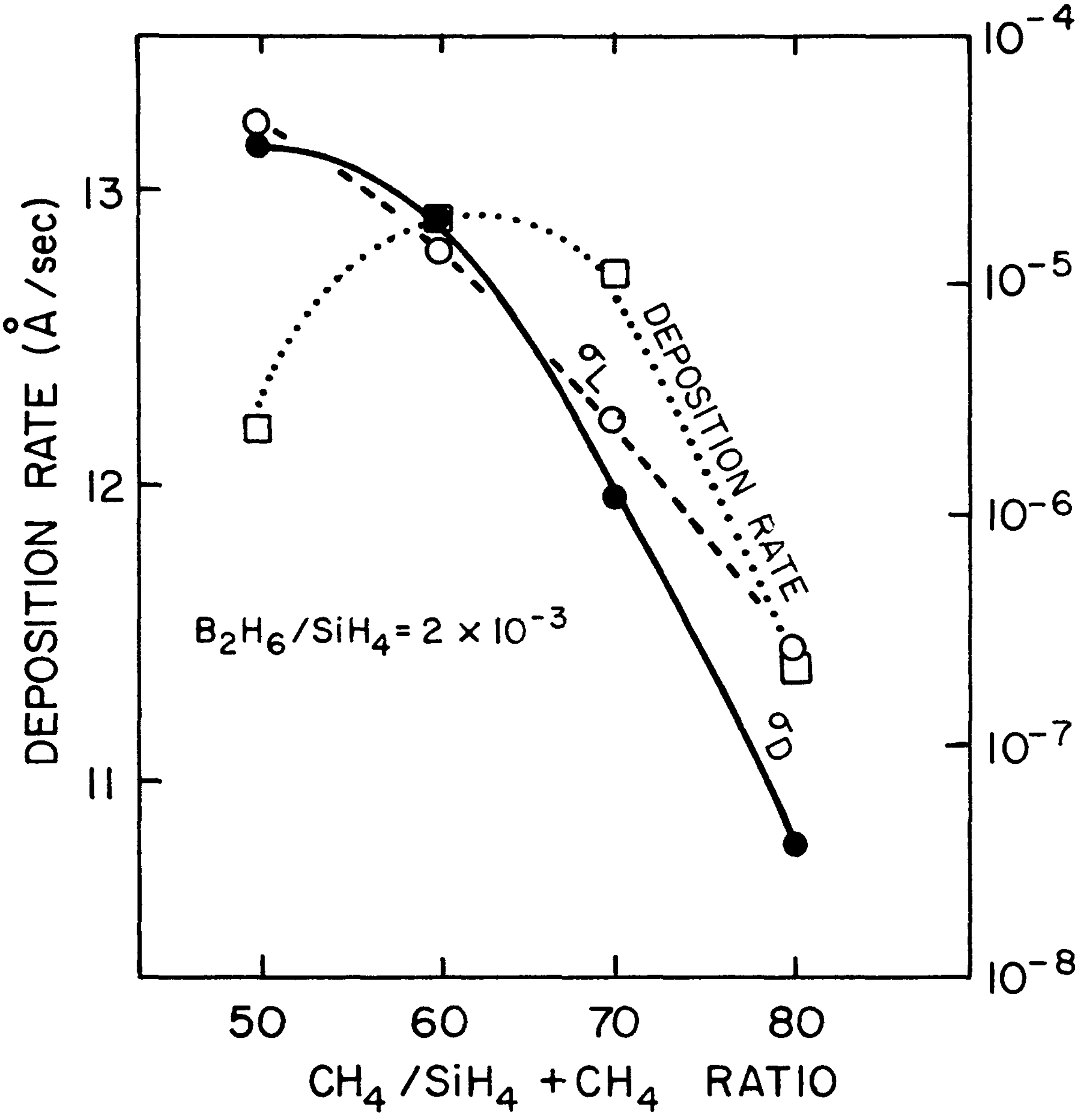

Figure 2-36. CH_4 Fraction Dependence Of Dark, Photoconductivity σ_D, σ_L And Deposition Rate

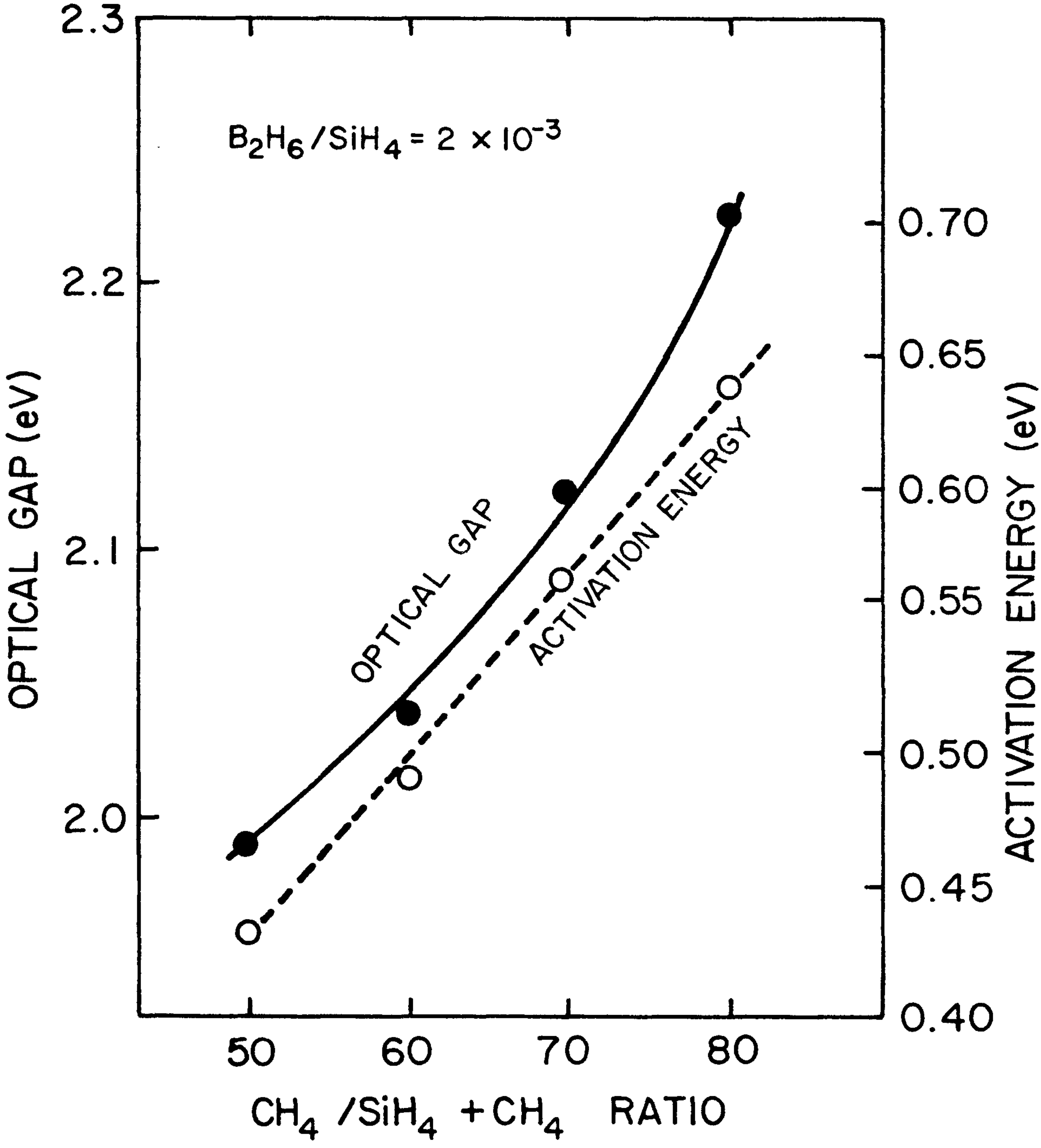

Figure 2-37. CH_4 Fraction Dependence Of Optical Gap And Activation Energy

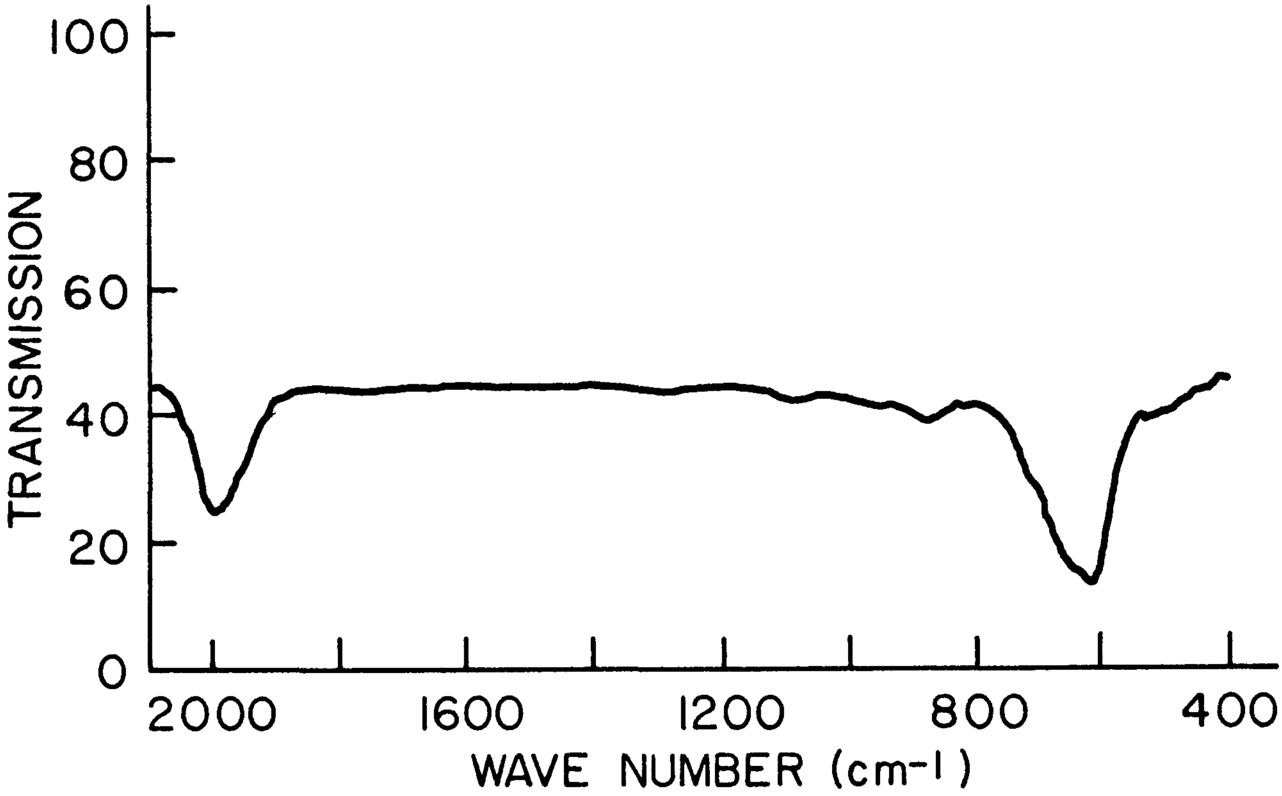

Figure 2-38. IR Spectra Of Undoped a-Si Films
Film thickness is 2 μm.

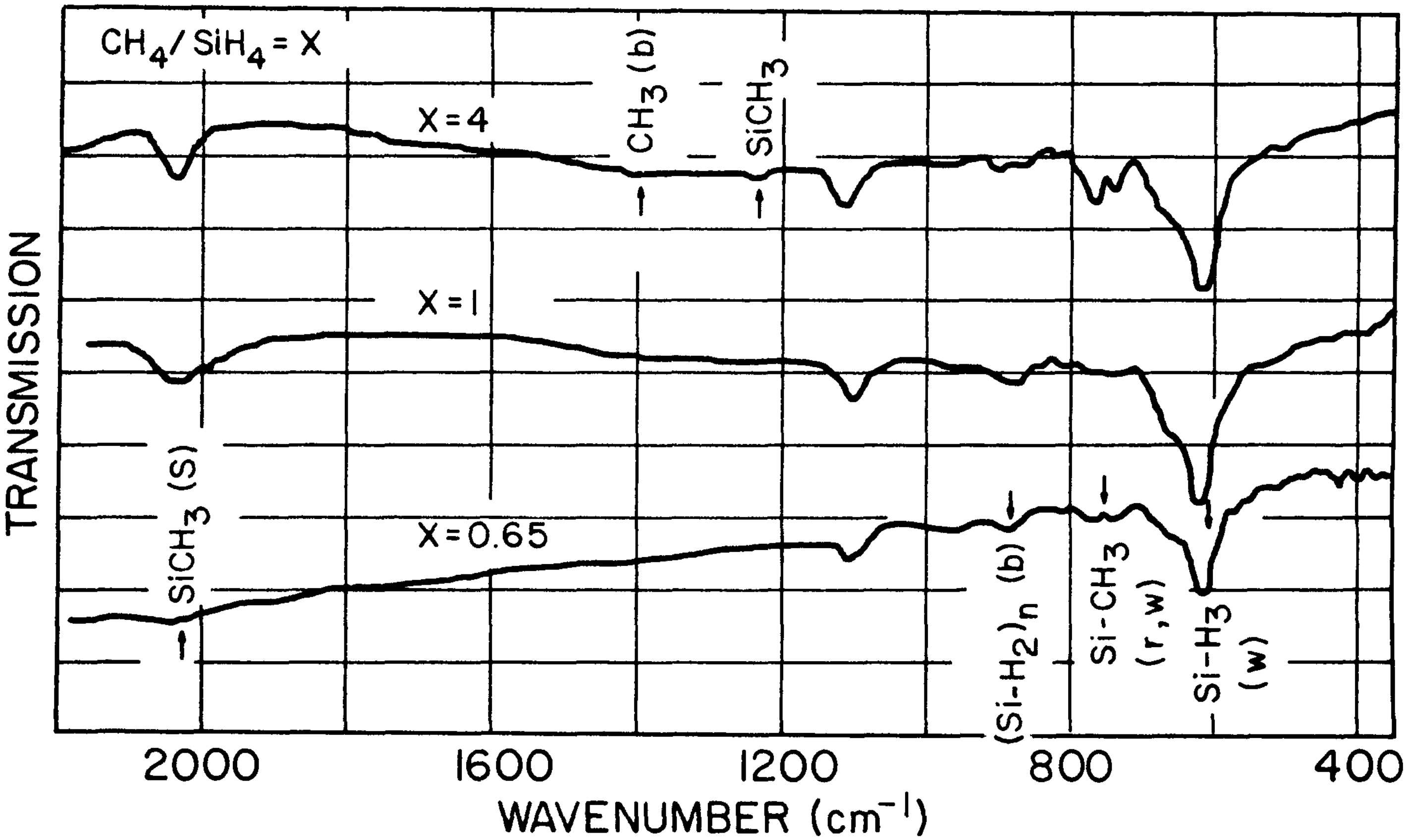

Figure 2-39. IR Spectra Of p^+ a-SiC:H
Film thickness if 1 μm.

3.0 TASK TWO - NON-SEMICONDUCTOR MATERIALS RESEARCH

3.1 Substrate

Polyimide continues to be the substrate of choice since attempts to make devices on other "high-temperature" polymers have not been successful. Vendors have made substantial improvements to the surface quality of polyimide film and shorting due to surface defects appears not to be a problem at this time.

3.2 Back Metal Contact

Efforts this year have been directed at improving the conductivity and reflectivity of the back conductive layer while maintaining compatible contact to the p^+ a-Si layer. For the metal depositions, a Vac-Tec diffusion-pumped roll coater equipped with two 5 inch x 15 inch cathodes is being used. The system is equipped with a 3 kW RF power supply and a 10 kW dc magnetron power supply. A gas flow controller for three separate gases provides the capability of reactive sputtering. Prior to deposition, the polyimide film is out-gassed by passing it through a radiant heater which is mounted in the vacuum system.

3.2.1 Nickel

Ni is used as the standard back metal contact and serves as a reliable contact to p^+ a-Si. It is not the ideal back metal contact because of its moderately high resistivity (7 μ ohm-cm) and poor reflectivity (40% at 600 nm). One method of increasing the reflectivity is to overcoat the metal with a dielectric such as SnO_2. Sputter deposited Ni films are specularly smooth as shown by the SEM photograph in Figure 3-1. When 600 Å of SnO_2 is sputter deposited on top of the Ni, it too is smooth as shown in Figure 3-2. With this 600 Å film interposed between the Ni and a-Si layer, the reflectivity is increased to 76% at 600 nm, according to optical modeling calculations.

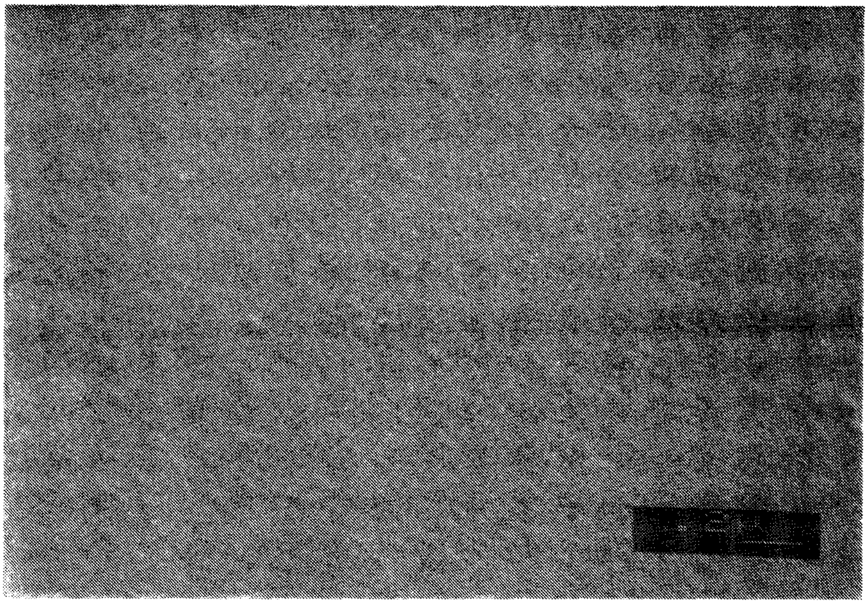

Figure 3-1. SEM Photograph Of 800 Å Ni On Polyimide This 50 KX SEM photo reveals an optically smooth surface.

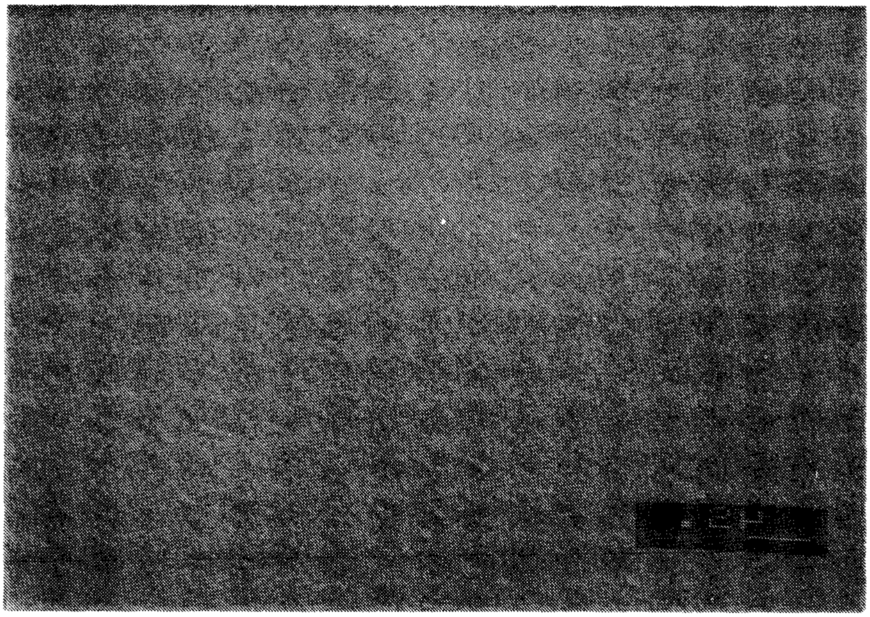

Figure 3-2. SEM Photograph Of 800 Å Ni/600 Å SnO$_2$ The SnO$_2$ uniformly covers the Ni film.

The I-V characteristics of a typical device constructed with Ni as the back electrode and Cr as the front contact are shown in Figure 3-3. Attempts to fabricate devices on Ni/SnO_2 were unsuccessful due to the SnO_2 being reduced to Sn during the glow discharge cleaning step and/or during the a-Si depositions.

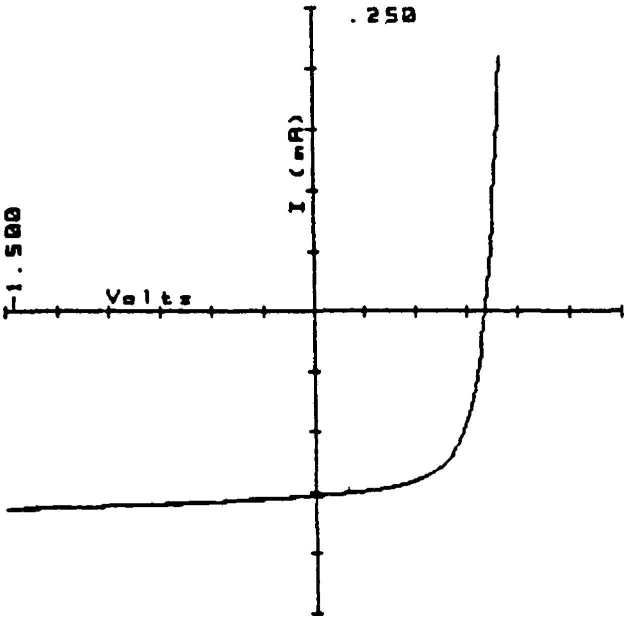

Figure 3-3. Current-Voltage Characteristic Of A Typical Ni/p-i-n/Cr Device
The open current voltage is 0.84V and the fill factor is 0.62.

3.2.2 Aluminum

Aluminum offers an improvement over nickel as the back metal contact. Its resistivity is 40% that of Ni and it reflects 72% at 600 nm, considerably more than nickel's 40%. In addition, aluminum does not form a specularly smooth surface. Due to its relatively low melting point of 660°C, aluminum can be deposited with a textured surface as shown in Figure 3-4. This textured interface causes diffused scattering of the light which penetrates the a-Si layer. This in turn increases the path length and thus the light absorption within the intrinsic layer, thereby increasing the red response and the overall efficiency.

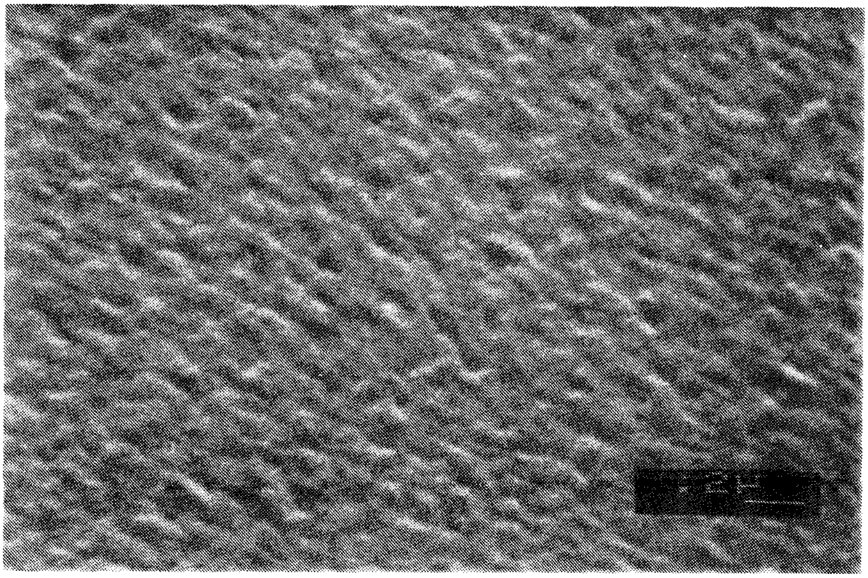

Figure 3-4. SEM Photograph Of 800 Å Of Aluminum On Polyimide Note the textured surface.

One major drawback of Al is that it does not form a suitable contact to p-type a-Si, probably due to diffusion of Al into the a-Si. Furthermore, if exposed to air before the a-Si deposition, Al forms a highly resistive oxide layer which later results in low device fill factor. The I-V characteristics of a typical Al/p-i-n a-Si/Cr device are shown in Figure 3-5.

3.2.3 Aluminum/Tin Oxide

In an attempt to solve the Al diffusion problem as well as to enhance the reflection from the back contact, 600 Å of SnO_2 was sputter deposited onto the Al film without exposing the Al film to air. The reflectivity is increased from 72% to about 90% for 600 nm light by introducing the SnO_2 film. The SnO_2 again conforms to the metal as shown in Figure 3-6, thus preserving the texture of the Al.

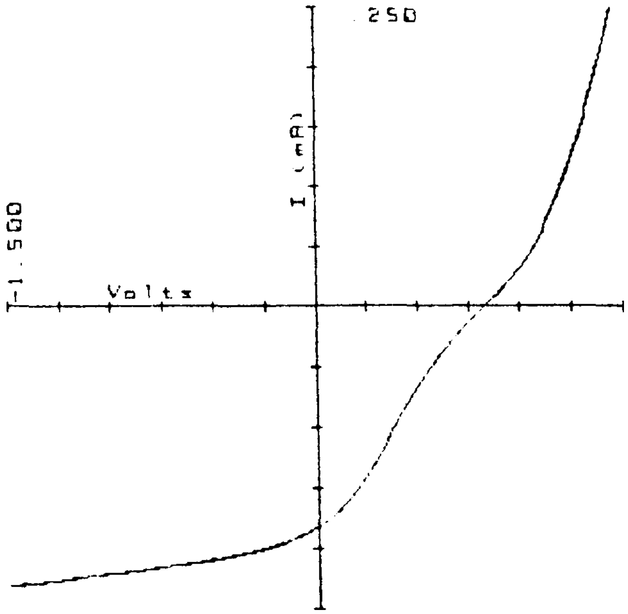

Figure 3-5. Current-Voltage Characteristics Of A Representative Al/p-i-n a-Si/Cr Device On Polyimide
Note evidence of a contact problem in the vicinity of V_{oc}.

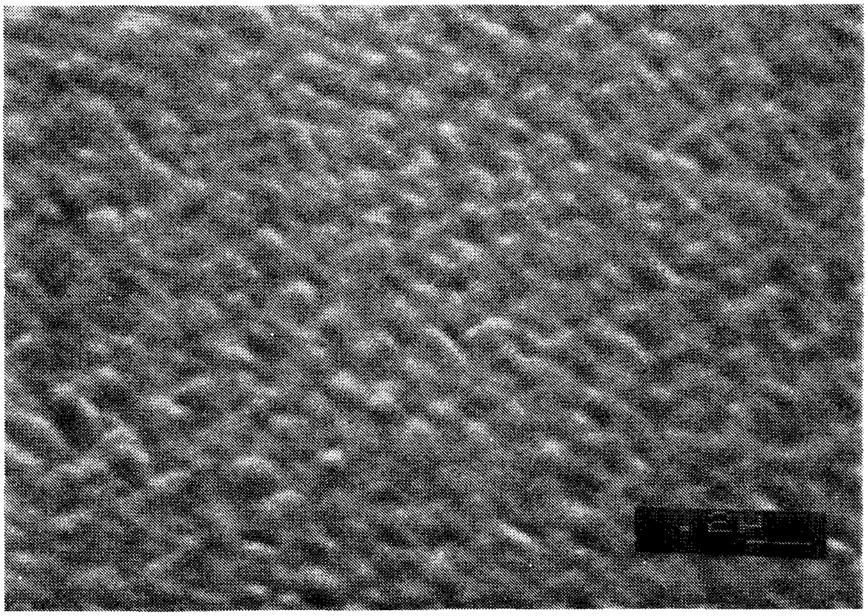

Figure 3-6. SEM Photograph Of 800 Å Al/600 Å SnO_2 On Polyimide
Note that the texture is similar to that of aluminum as shown in Figure 3-4.

The I-V characteristics of devices made on Al/SnO$_2$ show that this is not a good contact to p$^+$ a-Si. These devices typically have low fill factors ($\leq$ 0.50) as shown in Figure 3-7(a), or low fill factors and large shunt currents, as shown in Figure 3-7(b).

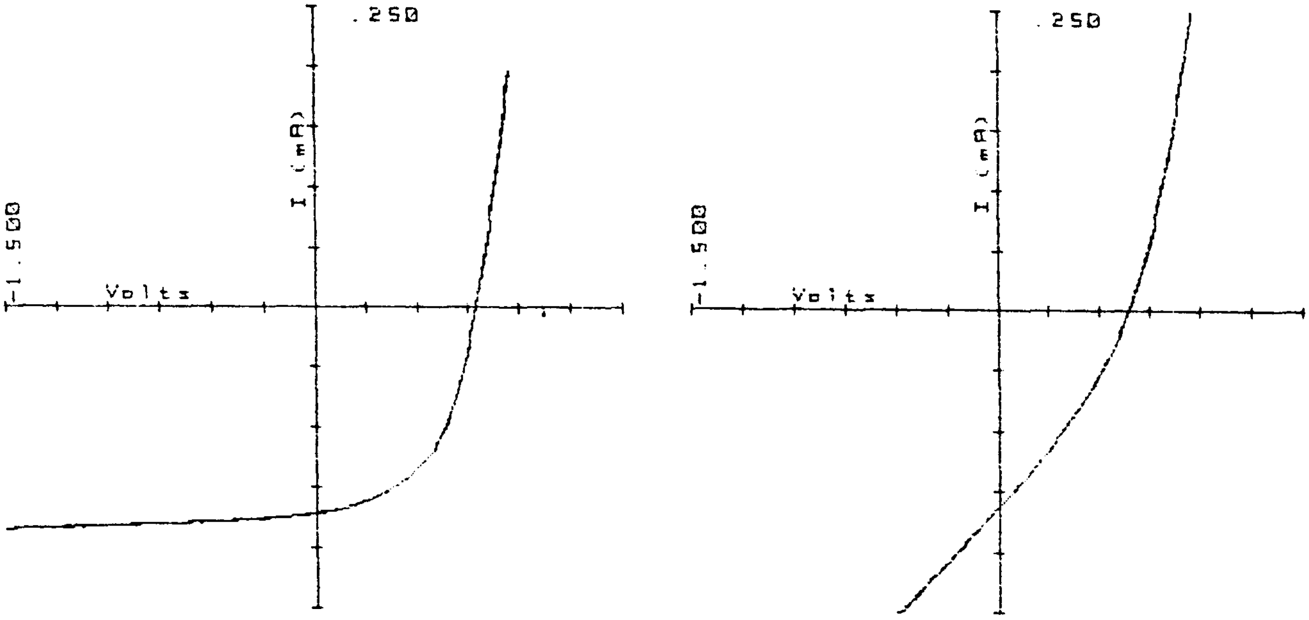

(a) (b)

Figure 3-7. Current-Voltage Characteristics For Representative Al/SnO$_2$/p-i-n a-Si/Cr Devices On Polyimide
Note the low fill factor and large shunt current.

3.2.4 Aluminum/Stainless Steel

The aluminum/stainless steel bilayer has been shown by Teijin to be an effective electrode for a-Si photovoltaic devices [16]. Stainless steel layers as thin as 25 Å are effective in preventing Al contamination of the a-Si but overall reflectance is reduced. For a 50 Å thick layer of stainless steel, the light absorbed by the back contact is increased by approximately 50%, while the advantages of high conductivity and the textured surface are maintained. A series of Al/stainless steel/p-i-n a-Si/Cr devices were constructed in which the stainless steel layer thickness was the only parameter varied. It was demonstrated that for stainless steel thicknesses of 25 Å, 50 Å, 100 Å, and 200 Å, devices were obtainable having fill factors in excess of 0.60. The current-voltage characteristics for a typical device incorporating a 25 Å stainless steel barrier are shown in Figure 3-8.

These studies have demonstrated that Al can be used for the back metal contact provided that a diffusion barrier is used.

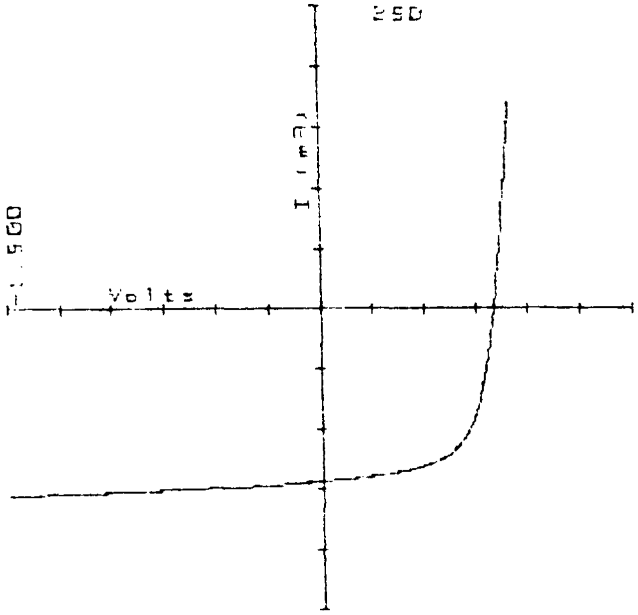

Figure 3-8. Current-Voltage Characteristics For A Representative Al/Stainless Steel/p-i-n a-Si/Cr Device
The Al and stainless steel thicknesses were about 700 Å and 25 Å respectively. The fill factor for this device was 0.63.

3.2.5 Aluminum/Titanium Nitride

Titanium nitride is a practical improvement over stainless steel as a diffusion barrier between Al and a-Si. TiN is highly conductive and much less absorptive than stainless steel. For wavelengths above 6500 Å, a 200 Å thick interlayer of TiN enhances the reflectivity of the back contact over the values for bare Al. The TiN is deposited by reactive dc magnetron sputtering. Typical sputtering parameters are:

Target: 5" x 15" x 0.25" titanium
Voltage: 400 Volts
Current: 2.0 Amps
N_2 flow: 5 sccm
Ar flow: 5 sccm
Substrate speed: 0.7 feet/minute

The current-voltage characteristics of such a device are shown in Figure 3-9.

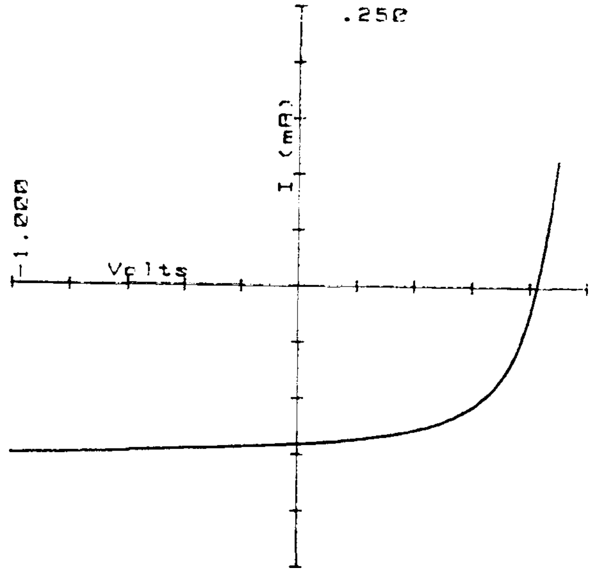

Figure 3-9. Current-Voltage Characteristics For A Representative Al/TiN/p-i-n a-Si/Cr Device
The Al and TiN thicknesses were approximately 1000 Å and 200 Å, respectively. The fill factor for this device was 0.62.

3.3 Transparent Front Contact

The low optical absorption and high electrical conductivity requirements of the front contact are accomplished most successfully by using indium-tin oxide (ITO). In the past, a major drawback in the use of ITO has been its tendency to yield free indium to the a-Si, thus causing degradation in cell efficiency. It is believed that this problem can be minimized by making use of a low-temperature sputter deposition technique for the ITO. This is the approach being pursued.

3.3.1 ITO Depositions

3.3.1.1 Batch Coater

A batch coater is being used to facilitate efficient and timely progress in small area device testing and interface studies. The batch coater is equipped with a shuttered 5 inch x 15 inch target driven by a 1 kW RF power supply. The samples to be coated are covered with a polyimide mask and clamped to a heater block which is mounted on a water-cooled table. The ITO films are deposited by reactive sputtering from an In/Sn target. The deposition rates are kept very low (approximately 10 Å/minute) in order to prevent damage due to excessive heating and high RF fields. Some films are deposited through a grounded copper screen mesh for the same purpose. Films of 700 Å thickness having less than 100 ohms/square sheet resistance have been routinely obtained with this system. Transmission of films deposited on glass is excellent (greater than 80% for wavelengths above 450 nm). The films are smooth and featureless as shown in Figure 3-10. When deposited on a-Si, the ITO conforms to the texture of the a-Si film as shown in Figure 3-11. ESCA analysis of these films indicates atomic composition of 63% oxygen, 33% indium and 3.7% tin. These ITO films are very stable under ambient conditions.

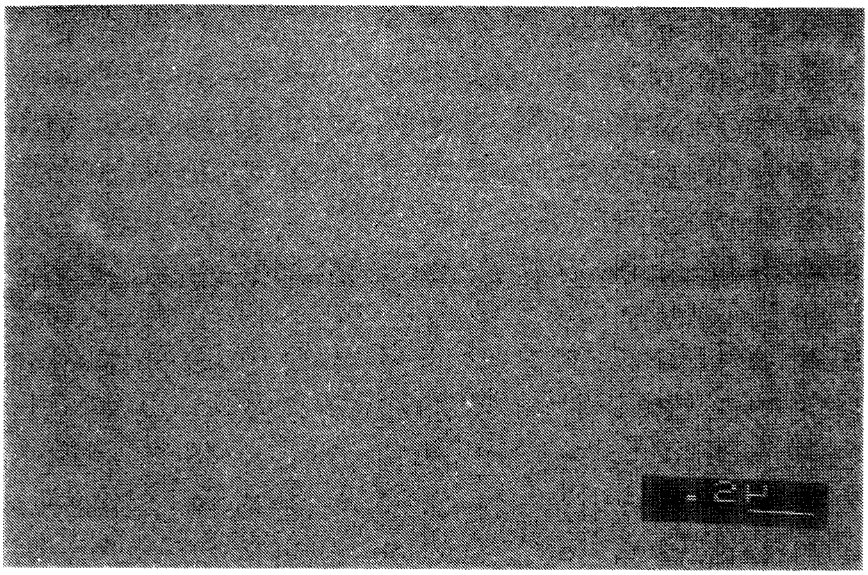

Figure 3-10. **50,000X SEM Of ITO On Glass From The Batch Coater**
This 700 Å thick film is smooth and featureless.

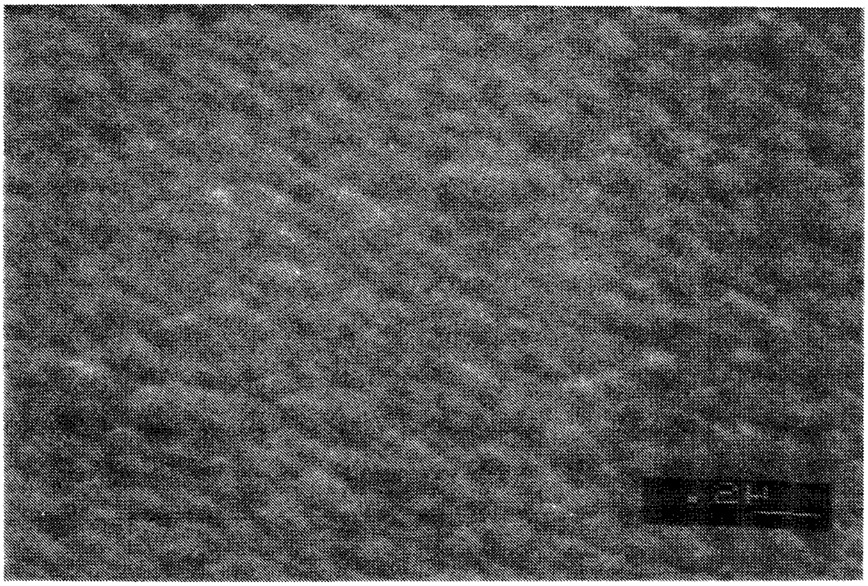

Figure 3-11. **50,000X SEM Of Device Using ITO From The Batch Coater**
The ITO replicates the texture of the a-Si film.

3.3.1.2 Continuous Coater

A 3M proprietary magnetically assisted process for sputter depositing high quality ITO films at low temperatures in a roll-to-roll deposition system has been developed. This sputtering system is capable of depositing ITO layers on unheated 4-inch wide rolls. Currently, 2100 Å thick films deposited in this system have a sheet resistance of approximately 30 ohms/square. The substrate temperature during deposition is estimated to be less than 60°C. Initially, devices made in this system suffered from unstable ITO, as the sheet resistance of the ITO increased rapidly in room air. Elemental analysis by ESCA revealed the composition of these films to be 54% oxygen, 32% indium, 1.8% tin, and 10% carbon. The instability was presumed to be due to the high carbon content; the source of the carbon was traced to the method of splicing the samples together and possible over-heating of the film edges. Measures were taken to minimize those problems and current films exhibit excellent stability.

These films are highly transparent as shown by the spectra in Figure 3-12, for one such film deposited on polyester.

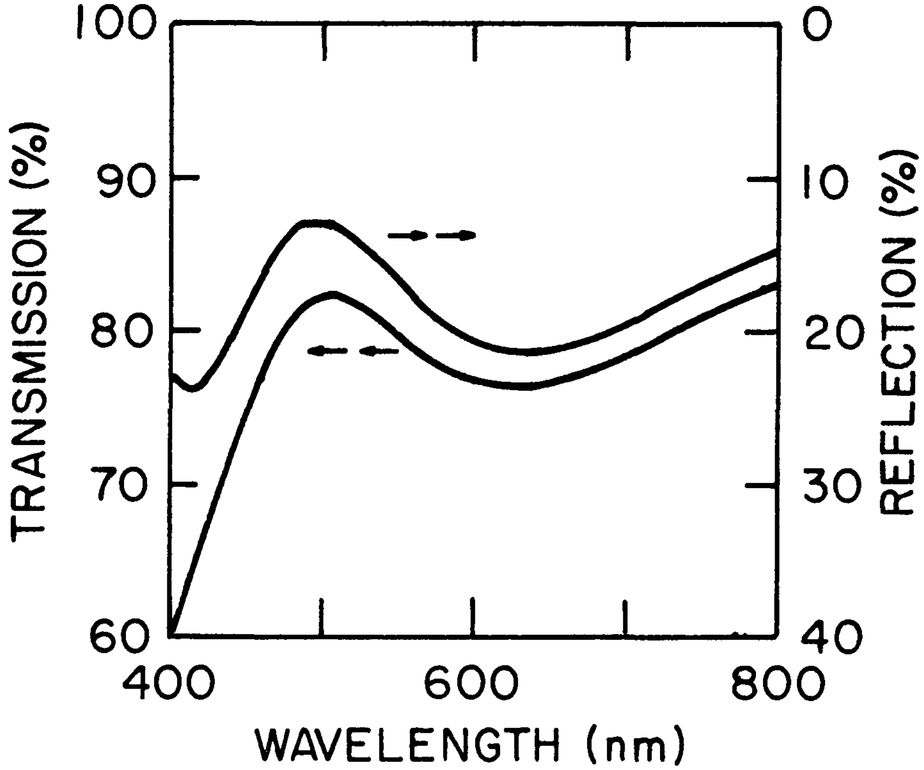

Figure 3-12. **Transmission And Reflection Spectra For 2100 Å ITO Film Produced In The Continuous Coater**
Note the absorption loss is 2-5% over the useful spectral range.

Significant differences exist between the texture of these films and those produced in the batch coater. As shown in Figure 3-13, the ITO films produced in the roll coater exhibit a fine texture with domains of about 200 Å in diameter. The coarser texture seen in this SEM of 0.2 to 0.3 microns is that of the a-Si.

3.3.2 ITO/Amorphous Silicon Interface

The most sensitive probe of the ITO/a-Si interface is the I-V characteristics of a device which incorporates this interface. In order to obtain useful information, however, one must establish what the contributions to the I-V characteristics are from other interfaces and from the materials. This is particularly true when heat treating or aging is involved since each interface and material could undergo a change.

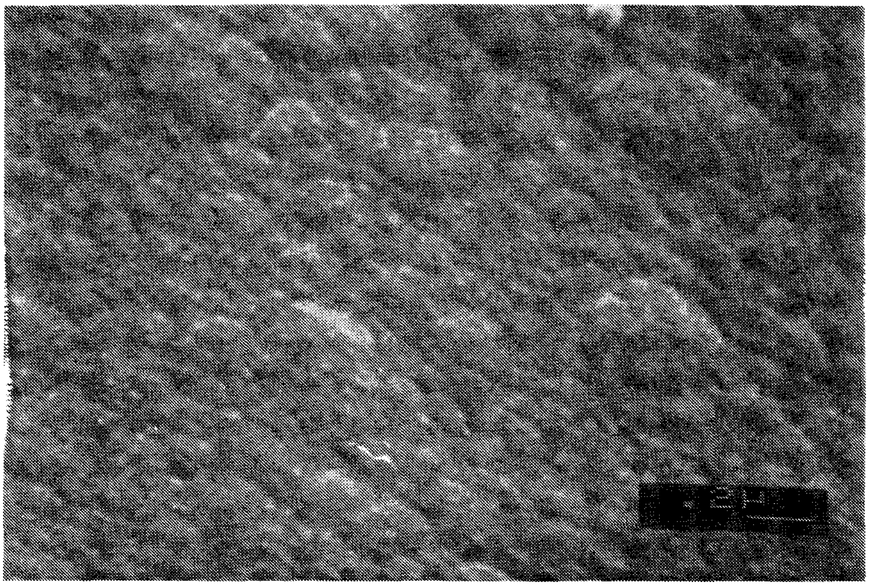

Figure 3-13. 50,000X SEM Of A Device Using ITO From The Continuous Coater
Notice the fine texture of 200 Å diameter domains.

In order to study the ITO/a-Si interface, devices were heat-treated at 130°C and device characteristics were compared before and after heat-treating. The choice of 130°C is not arbitrary. The temperature should be significantly above expected operating temperatures in order to be meaningful. On the other hand the temperature should not be so high as to introduce deterioration mechanisms that will be negligible at operating temperature. It was established that the other interfaces and materials involved were not affected by the heat-treatment. Control devices were constructed adjacent to the test device using semi-transparent Cr contacts in place of the ITO. No significant change occurred in the devices with the Cr contact subsequent to heat-treatment. The devices with ITO contacts deteriorated as shown in Table 3-1. We are evaluating diffusion barriers such as SiN to eliminate this problem.

Table 3-1. Device Characteristics Of Heat-Treated Ni/p-i-n a-Si/ITO Devices
The devices were held at 130°C for intervals of 1, 2 and 16 hours.

Cumulative time (hours)	0	1	3	19
Fill Factor (%)	42.2	40.7	29.5	22.2
Open Circuit Voltage (Volts)	0.82	0.84	0.84	0.84
Short Circuit Current (mA/cm^2)	8.49	8.52	7.97	4.11

3.4 Evaluation Of Light Loss Mechanisms

In principle, all of the incident radiation of energy which is higher than the i-layer band gap value, at a wavelength less than about 750 nm, could contribute to the I_{sc} and thus to the cell efficiency.

Losses other than recombination of carriers within the p-, i- or n-layer of the a-Si can be separated into the following areas:

1) reflection from the front contact
2) absorption in the front contact
3) absorption in the back contact
4) reflection from the back contact (and subsequent loss through the front contact)

The reflection loss of a 2000 Å thick ITO film on a-Si is less than 5% at 580 nm and less than 10% for 500 to 700 nm. Some improvement can be expected by engineering a bilayer or multi-layer anti-reflection coating which incorporates such an ITO layer. As shown in Figure 3-12, the absorption loss in a 3λ/4 ITO film is 2 to 5% for wavelengths above 500 nm. Little or no improvement over these values is possible.

Substantial losses can occur from absorption of long wavelength (> 600 nm) light by the back contact. For Ni, as much at 60% of the light not absorbed by the a-Si is absorbed at the back contact. By choosing Al, the loss is reduced to 28%. The loss can be reduced further to about 10% by inserting a nominal λ/4 thick transparent dielectric film. This film must be at least moderately conductive, compatible with Al and a-Si, and compatible with subsequent processing. TiN has been successfully used as this film but it suffers from a relatively high absorption loss.

Finally, most of the light that is reflected from the back contact may pass through the a-Si a second time and be coupled out of the cell by the 3λ/4 front contact. This loss can most effectively be reduced by causing the light to be scattered at large angles relative to the incident radiation. As discussed in Section 3.2.2, some scattering is achieved by having a textured back contact such as the Al film shown in Figure 3-4 and 3-6. Additional scattering may be obtained by texturing the substrate prior to metallization. Figure 3-14 is a SEM of a polyimide substrate that has been sputter-etched to produce a texture. The spectral response of a device made on this substrate is shown in Figure 3-15. For reference, the spectral response of a device having the same metal (Al/TiN) back contact on non-textured polyimide is super-imposed.

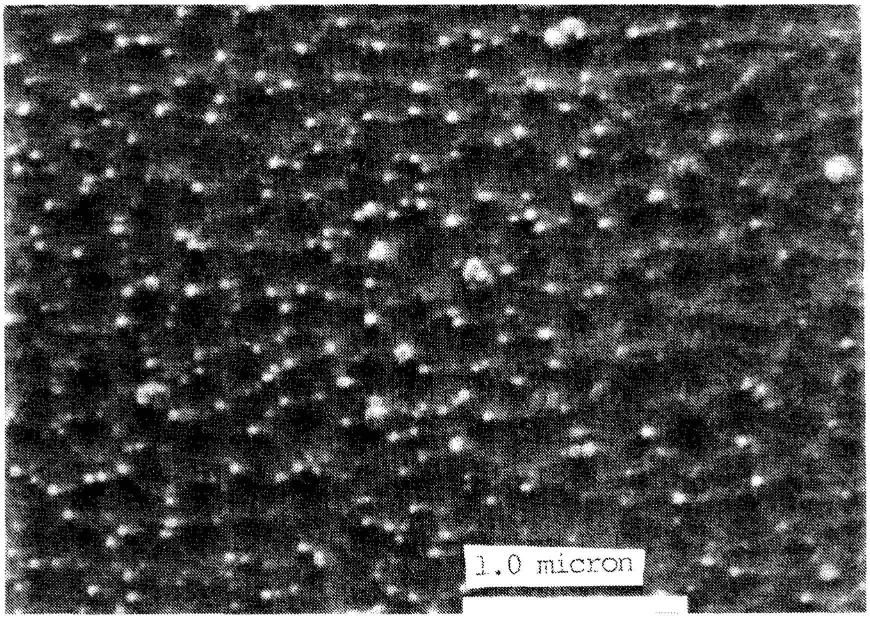

Figure 3-14. SEM Photograph Of Textured Polyimide
Texture was achieved by sputter-etching.

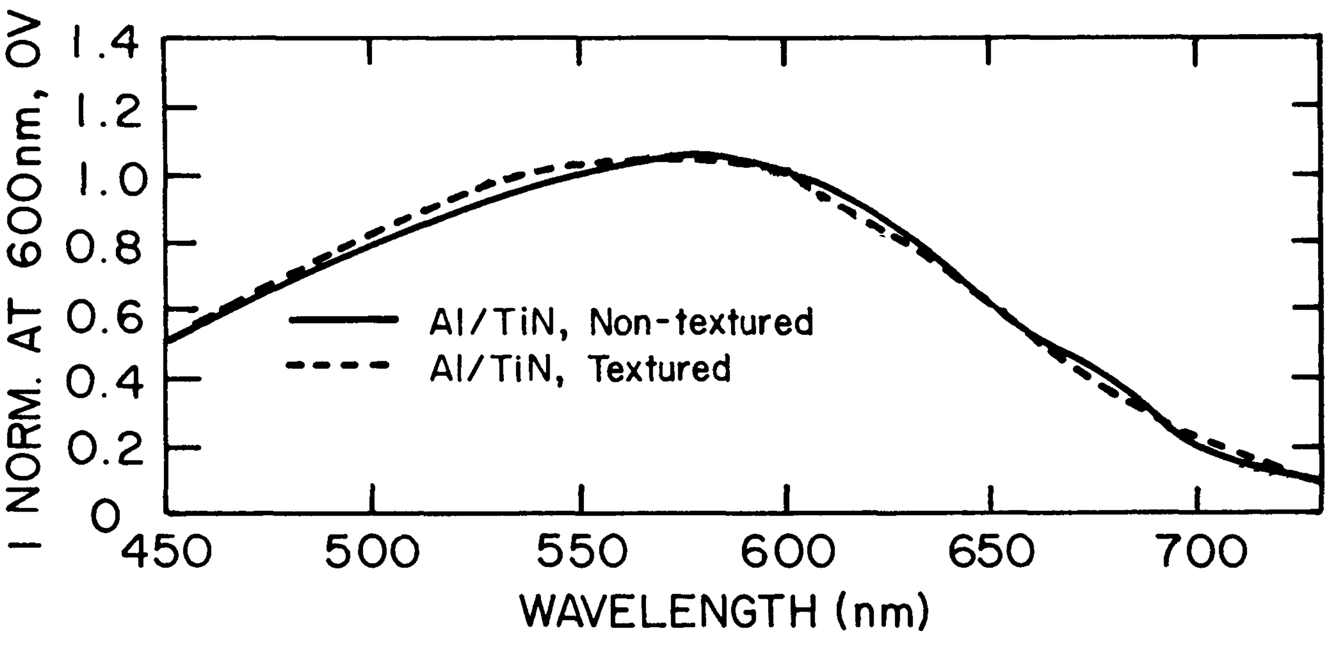

Figure 3-15. Comparison Of Spectral Responses Of Devices On Textured Versus Non-Textured Substrate
The structure of each device: is polyimide substrate/Al/TiN/p-i-n a-Si/Cr. There is little or no increase in red response of textured vs. non-textured polyimide.

4.0 TASK THREE - SOLAR CELL RESEARCH

4.1 Defect Characterization in Amorphous Silicon Solar Cells

A primary concern in fabricating a-Si solar cells on polyimide substrate involves the possibility that the higher surface defect density of the polyimide compared to glass will cause unacceptable shunting in large area cells. Figure 4-1 shows a micrograph of polyimide substrate and the defect density of polyimide is much higher than glass substrates. When proper substrate cleaning techniques are incorporated into the device fabrication process, the initially higher defect density of polyimide does not affect device quality.

A type 35C JEOL scanning electron microscope with a type 103B G&W current amplifier in the electron beam induced current (EBIC) mode is being used to investigate the relationship between substrate and fabrication induced defects, as well as charge collection efficiency in the solar cells.

In Figure 4-2, an EBIC image of a low resistivity shunt is shown. The bright areas represent the sites where all the generated current is being collected by the contacts. The shunt path is located in the middle of the dark area. The gray area radiating outward from the shunt indicates that a portion of the current is being collected and the remainder is being directed through the shunt path. The SEM image of this area shows no indication of substrate surface damage that accounts for the shunt.

Four different defect modes have been identified: 1) open or masking type defects, 2) shunts caused by dust particles on the substrate prior to deposition, 3) defects caused by inclusion of silicon dust into the device during deposition, and 4) surface damage.

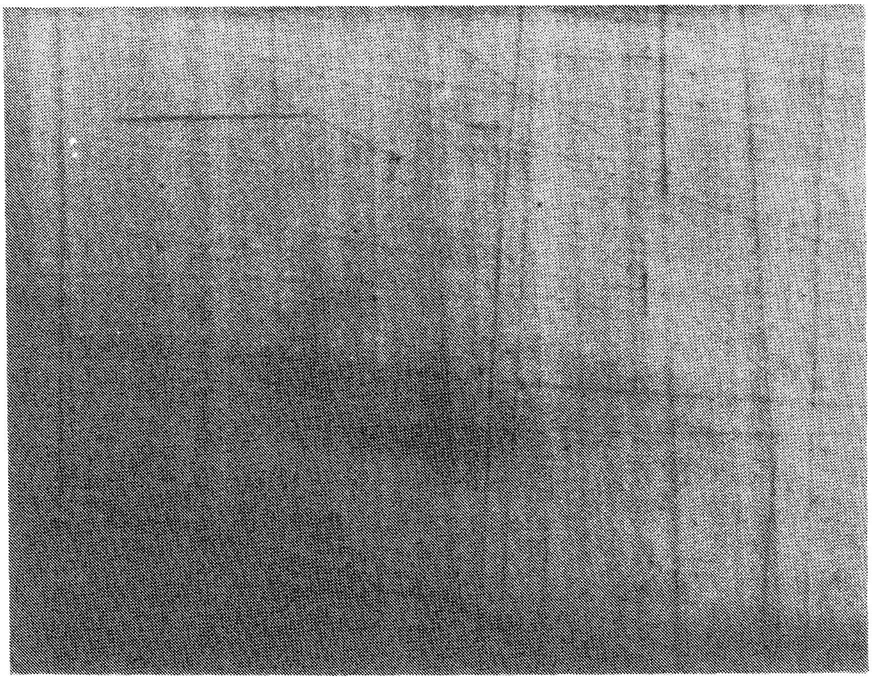

Figure 4-1. 75X Micrograph Of Polyimide Showing Line And Point Defects

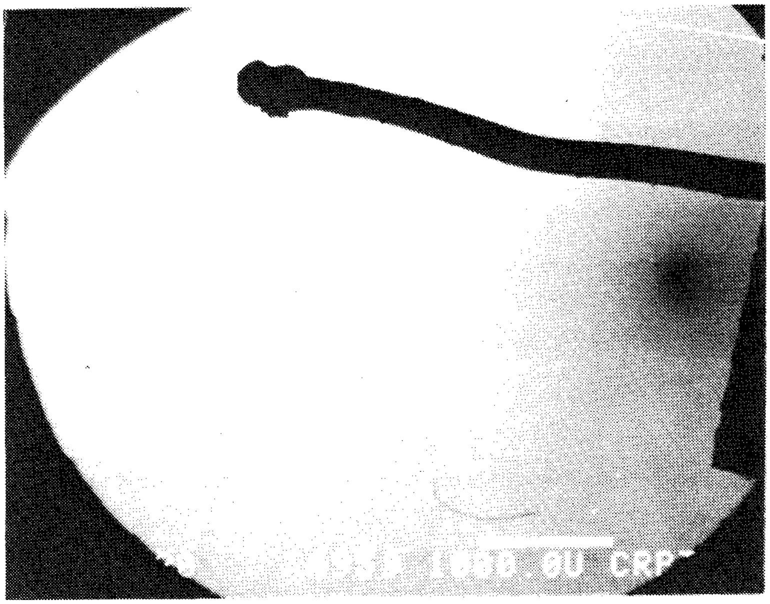

Figure 4-2. EBIC Image Of A PV Device Showing Classic Shunt Area

In Figure 4-3, the EBIC scan shows a distinct, dark area (no current collection) which is surrounded by a light area. In this type of open or masking defect, no current is drawn from the dark area. X-ray back scattering indicates that since there was a metal top coat in the affected area, the defect was caused by a non-contact condition on the bottom of the cell.

Figures 4-4a and 4-4b show an EBIC image and a high magnification SEM image of a classic shunt. It appears that a loose dust particle on the substrate surface caused a hollow area to form around its outer edges during deposition. This type of defect is the most detrimental to producing reliable large area devices. In this particular example, the V_{oc} was reduced by 50% on a 0.3 cm^2 sample.

Another type of shunt defect results from the inclusion of silicon dust into the active layers during device fabrication. This can occur when deposition conditions are not optimized and/or an improper reactor gas flow pattern is used. Under these conditions, large amounts of silicon dust are generated and incorporated into the devices (see Figure 4-5). Defects of this type are also of the masking or open variety and do not appear to have a detrimental effect on device characteristics unless a large number are present, causing the active area to be reduced significantly.

The last type of defect is caused by surface damage as shown in Figure 4-6. This defect results from either insufficient top contact or the presence of particulate contamination in the top layer. Masking defects of this type do not affect the V_{oc} of the device, however, current output is reduced because of the decrease in active area.

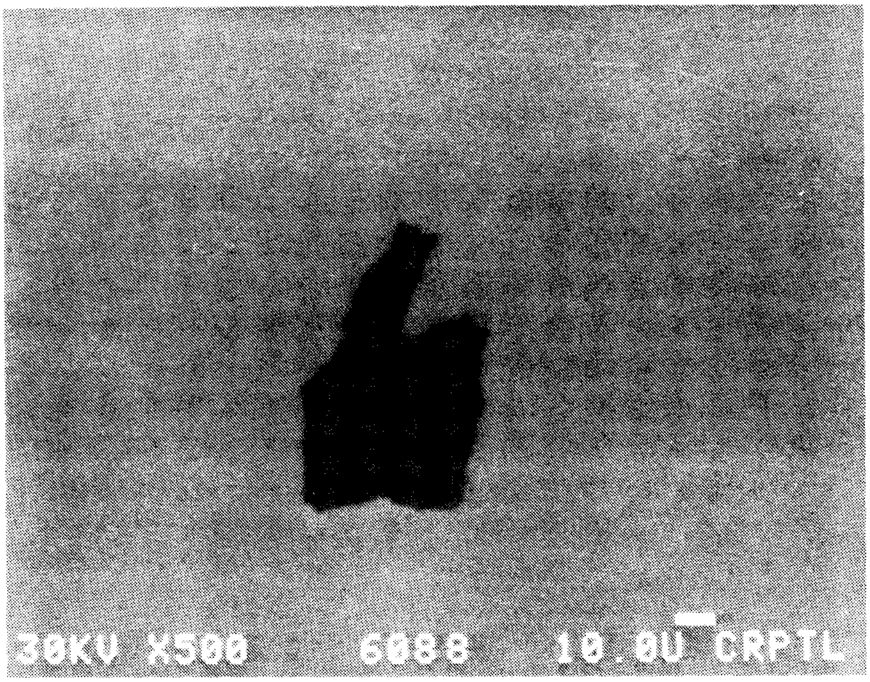

Figure 4-3. EBIC Image - Missing Contact On The Bottom Of The Cell

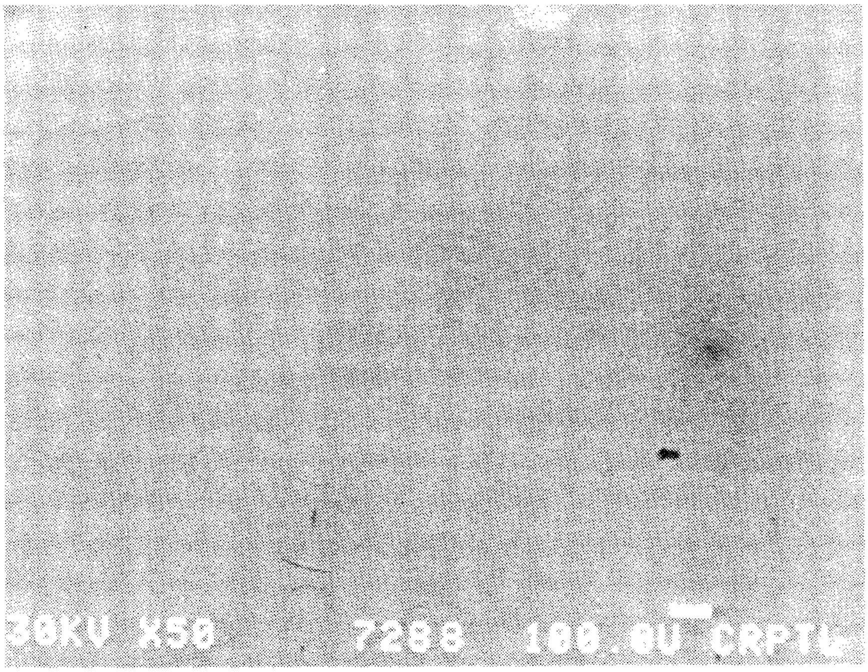

Figure 4-4 (a) EBIC Image Of A Classic Shunt Area On A PV Device

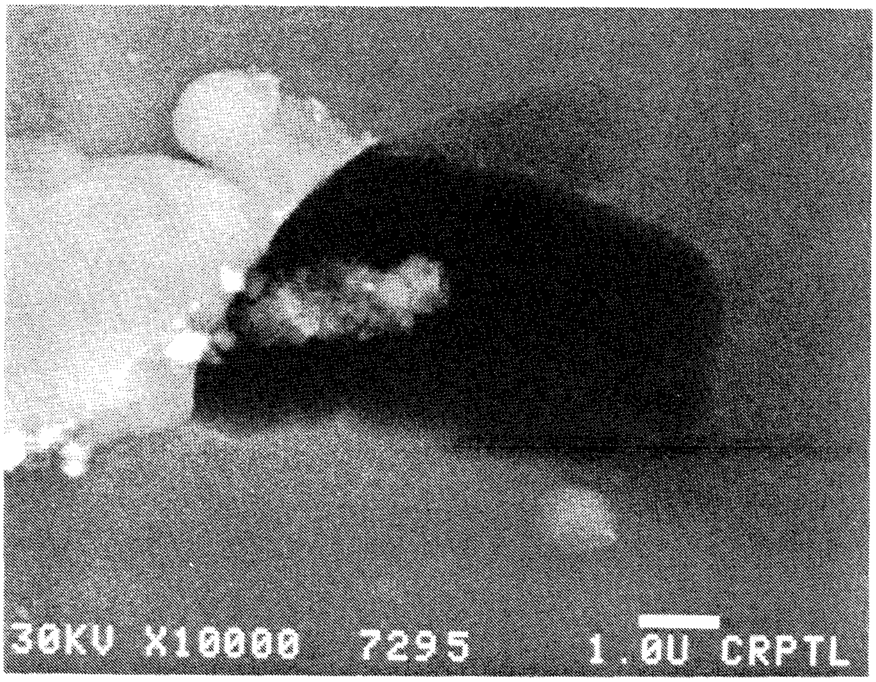

Figure 4-4 (b) 10,000X Magnification SEM Image Of Shunt Area Shown In 4-4 (a)

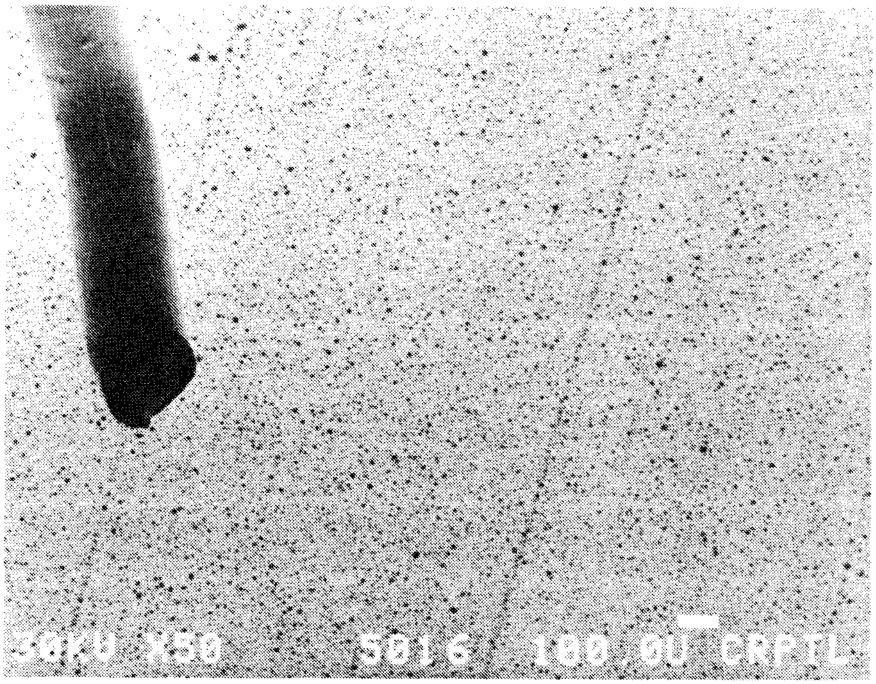

Figure 4-5. EBIC Image Of A PV Device Showing The Inclusion Of Silicon Dust Particles

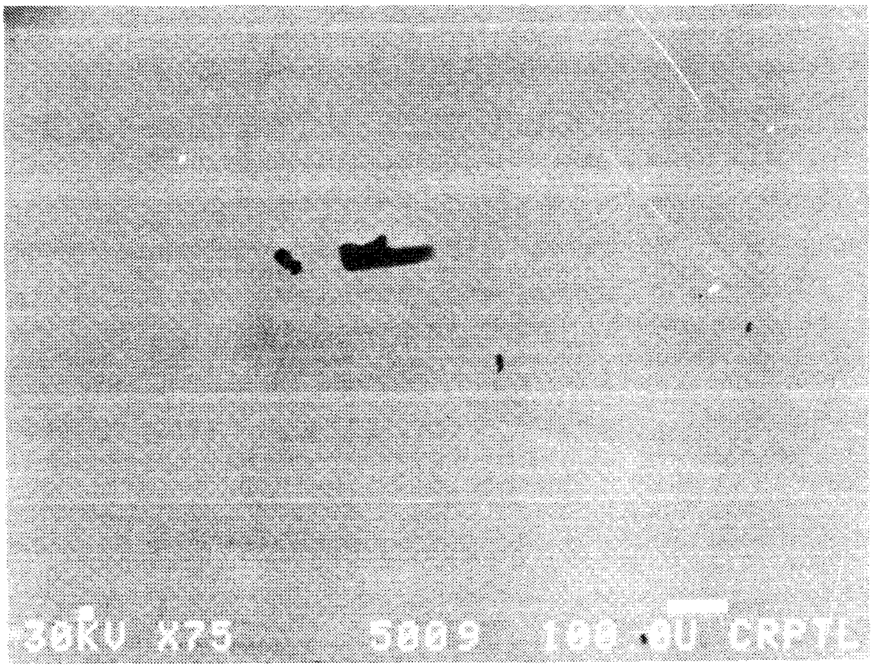

Figure 4-6. EBIC Image Of A PV Device Showing The Effect Of Surface Damage

From the above observations it has been determined that substrate surface cleanliness is the most important criteria relative to producing reliable a-Si devices. Shunt defects can result from dust on the substrate surface, as well as from loose particles of metal generated either during the deposition of the bottom metallized layer, or in the metal scribing step.

To determine the effect that substrate cleaning has on device yield, a study was performed in which Schottky barrier devices were fabricated on substrates which had been cleaned using various methods. In one technique, a 3M brand "Masterwipe" mechanical cleaner was used with ionized nitrogen. This cleaner consists of an upper and lower roll of soft nonwoven fabric through which the substrate is passed, followed by an anti-static device which neutralizes static charge with ionized air produced by alpha particles from a Polonium 210 source. The substrate surface was sprayed clean with ionized nitrogen and then subjected to an additional cleaning step a various number of times. Schottky devices were fabricated and the results are shown in Figure 4-7.

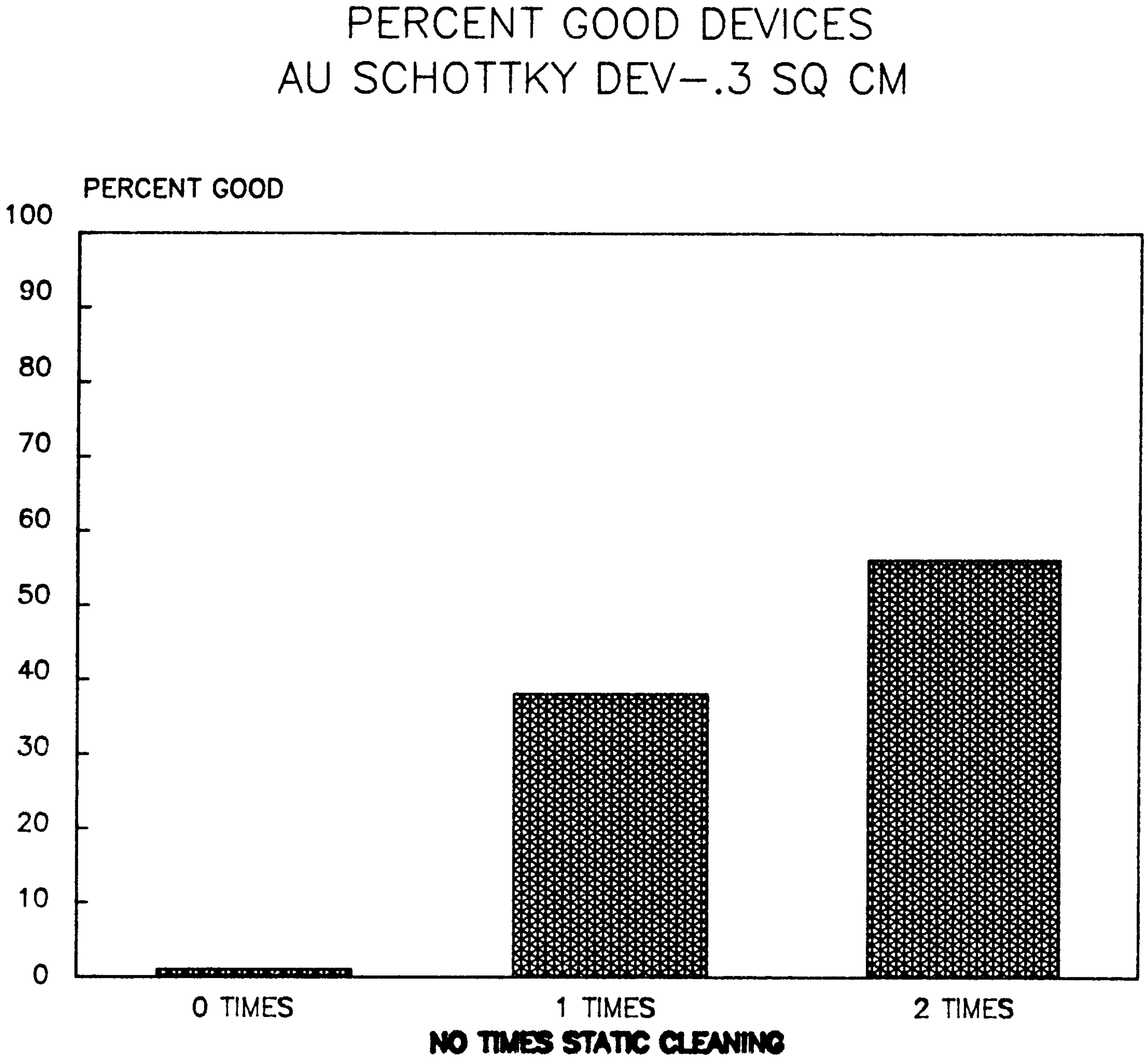

Figure 4–7. Effect Of Cleaning Procedures On The Percentage Of Good PV Devices

This experiment was performed prior to incorporating more stringent cleaning and handling methods into the device fabrication process, and demonstrates the need for such special procedures. Presently, all substrate material is handled in tightly wound rolls which are unwound only in a vacuum or in a glovebox with a nitrogen purge.

One important area which remains to be examined is the effect of polyimide substrate surface roughness on the charge collection efficiency of a-Si cells. An experiment has been initiated to analyze polyimide substrates of various defect density levels. The defect densities are determined by a method utilizing light scattering and EBIC, high magnification SEM, current-voltage, and laser scanning analysis.

Results obtained thus far indicate that even with an initial defect density much higher than that of glass, polyimide can be used as a flexible substrate provided that proper cleaning and handling procedures are followed. Future efforts will include completion of the substrate roughness study, followed by the initiation of studies pertaining to the relationship between high-quality device yield versus device area.

4.2 Device Fabrication in System Four

4.2.1 Substrate Effects

Series of devices have been fabricated on polyimide substrate obtained from two different vendors, referred to as Vendors A and B. The polyimide from Vendor A exhibits severe stress curling after silicon deposition. This curling problem is virtually non-existent with the Vendor B polyimide. In addition, the polyimide from Vendor B has a smoother surface topography. To date, no increase in device yield has been observed. This suggests that the device yield is limited by foreign particulate contamination.

Ni, Mo, and Al metallizations all yielded high percentages of shunt-free devices on polyimide substrate from both vendors. Devices made on Al coated polyimide showed very low fill factors, indicating a severe problem with the

Al/a-Si interface. Two different metallization layers were evaluated for use as a diffusion barrier between the Al/a-Si interface. One of the barriers examined was $\lambda/4$ thick SnO_2 and the other was stainless steel (200, 100, 50, and 25 Å layer thickness) deposited on the Al. In summary, a $\lambda/4$ thick layer of SnO_2 was not an effective barrier, whereas stainless steel barriers as thin as 25 Å, yielded devices with fill factors above 0.60.

4.2.2 Doping Effects

A dopant gas line was added to Systems Three and Four to permit compensational doping of the intrinsic layers with up to 5 ppm diborane. Devices were fabricated with intrinsic layers doped at levels of 0.1, 0.3, 1.0 and 3.0 ppm (ratio of B_2H_6 to SiH_4 flow rate) and intrinsic layer thicknesses ranging from 0.4 to 0.9 μm. Doping in the range of 0.3 to 3 ppm slightly increased the fill factor of the thicker devices (1 to 3% increase), but no improvement was observed in the thinner devices (0.4 μm intrinsic layer). It is probable that this result is due to the heavy boron carry-over from the deposition of the p^+ layer--the first deposited layer of the device.

To obtain a quantitative understanding of the boron carry-over, the photoconductance values of doped intrinsic layers on uncoated polyimide were compared to those of a nominally "undoped" intrinsic layer. The latter was deposited immediately following deposition of a p^+ layer on a previous frame of the polyimide web. Thus, the "undoped" intrinsic layer was deposited on fresh uncoated polyimide, but immediately following a typical p^+ layer deposition in the chamber.

The results show dramatic differences between the doped and "undoped" samples. In all of the doped samples without boron carry-over present, photoconductance values were approximately four orders of magnitude higher than those for dark conductance. Typical values were 10^{-7} ohms and 10^{-11} ohms, respectively. The nominally undoped samples with boron carry-over gave light and dark conductances of 1.0×10^{-6} ohms and 1.8×10^{-8} ohms, respectively. We conclude that boron doping of the i-layer cannot be effectively accomplished in our single chamber systems with a p^+-i-n^+ deposition sequence.

4.2.3 Effect of Geometry on Powdering

The severe powdering problem in System Four was eliminated by switching from the Teflon shield to a stainless steel shield, and by lowering the RF electrode-to-substrate gap spacing from 1 and 5/16" to 7/8". Spacings of 1 and 5/16", 1 and 1/16", 15/16", 7/8", and 3/4" were evaluated at a deposition pressure of 1.0 torr. The powder formation decreased significantly with decreasing distance between the shower head electrode. At a spacing of 3/4", deposition uniformity suffered, thus the spacing was reset to 7/8". Uniformity can be improved with carefully constructed shields which give the proper gas flow pattern, but not with the flexible stainless steel sheet metal currently being used. At 7/8" spacing the V_{oc} was low (0.82V). Upon increasing the spacing to 1.0", the V_{oc} was improved to 0.85V and powdering was held to an acceptable level.

With the present geometry of System Four, a smooth continuous 1 meter a-SiH deposition, or up to 10 separate depositions on 4 inch frames can be obtained.

4.3 Amorphous Silicon Nitride

The 3M solar cell utilizes an opaque substrate. If the p^+ layer is deposited first, as it must be in the single chamber system, an appropriate window material must be used for the n^+ layer. Although the microcrystalline n^+ layer forms a suitable window, the cell performance degrades when ITO is deposited as the top contact, as compared to using Cr as a top contact. The two possible failure mechanisms are indium diffusion and energetic particle bombardment of the cell during the ITO deposition. Very few material candidates exist for an optically non-absorbing, electrically conducting, protective barrier. Even the process of depositing a barrier such as SnO_2 by sputtering can damage the device. The only feasible candidate identified thus far is amorphous silicon nitride (a-SiN). This material is being evaluated as a window material that simultaneously acts as a diffusion/ energetic particle barrier. With its index of refraction intermediate between those of a-Si and ITO, a-SiN can also be used to improve the optical absorbance of the cell (see Section 4.4).

Another advantage of a-SiN is that it is easily deposited. The technique used is identical to that for depositing a-Si in the same chamber (System Four). Ammonia is added to the gases in the glow discharge. Previous researchers have shown that both the amount of nitrogen incorporated in the films and the a-SiN band gap, are linear with respect to the ratio of NH_3 to silane for low NH_3 content [17, 18].

The difficulty associated with utilizing a-SiN involves proper P-doping to achieve high conductivity at the highest possible band gap. Acceptable activation energies have been obtained only for NH_3/SiH_4 ratios $\leq$ 1/4, which corresponds to band gaps of $\leq$ 2.0 eV. For a 2.0 eV band gap, the lowest activation energy obtained thus far is 0.34 eV. Some of the optimization data are shown in Figures 4-8 and 4-9. Initially, work was done using silane/ammonia ratios of 4.5/1 ($E_g \sim 1.9$). Activation energies of $\leq$ 0.3 eV have been attained for this material. However, a band gap of 2.0 eV or higher is desirable and work has continued on those materials.

The reactor has a 1-inch electrode gap and the dimensions of the shower head electrode are 6 inches x 7 inches. Using a deposition pressure of 1.5 torr, and 15W RF power, an activation energy of 0.34 eV was achieved for the SiH_4/NH_3 flow ratio of 4/1, and $H_2/(SiH_4 + NH_3)$ flow ratio of 9/1. As the data in Figure 4-9 indicate, the optimum power settings (and probably the pressure and total flow rate) change with different SiH_4/NH_3 flow ratios. Work is continuing on studying the effects of the total flow rate and hydrogen ratio. Since ARCO Solar has a reported E_a = 0.25 eV, measured on material with a 4/1 SiH_4/NH_3 ratio [17], it should be possible to obtain a better doped a-SiN material than that produced thus far in our system.

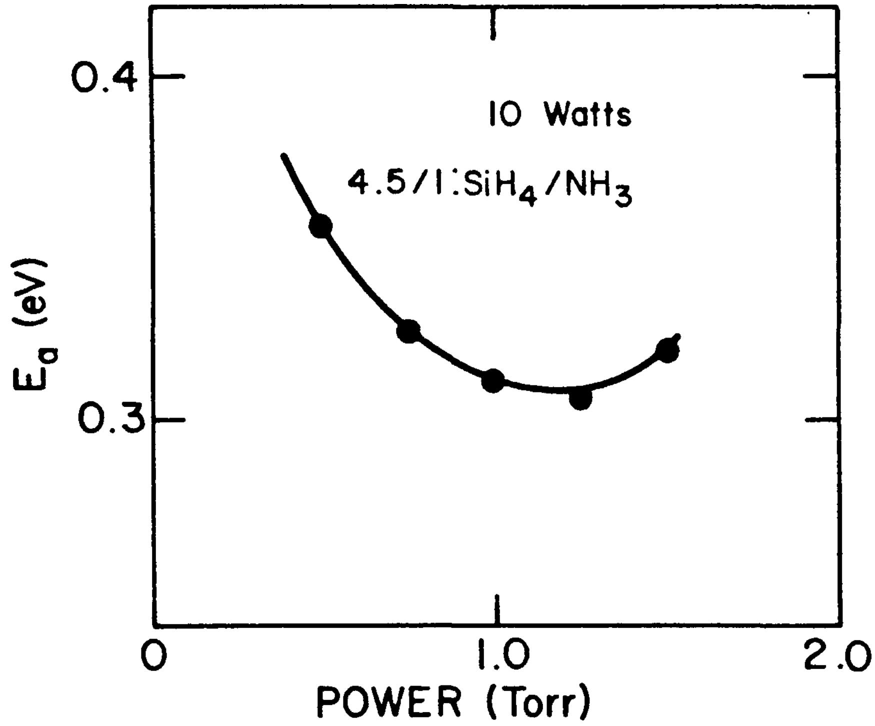

Figure 4-8. Activation Energy Of 1.9 eV Band Gap Amorphous Silicon Nitride Doped With Phosphorous, As A Function Of Pressure

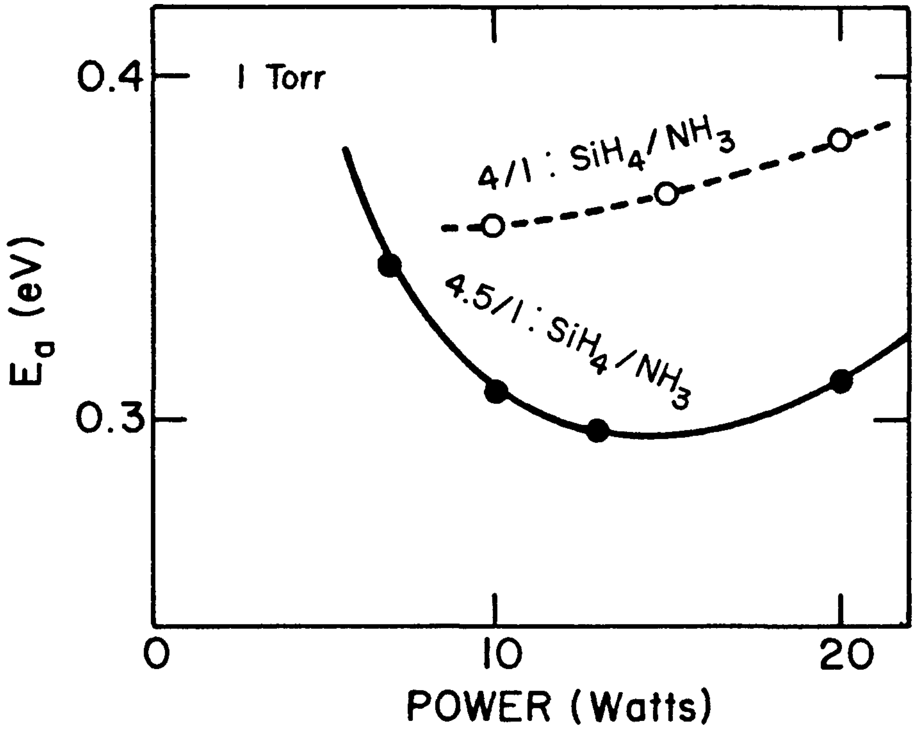

Figure 4-9. Activation Energy Of n^+ Doped a-SiN As A Function Of Power, For Two Different Ammonia/Silane Ratios

The I-V curve of a device (Cr dot contact, 0.05 cm^2) made with the a-SiN n^+ layer is shown in Figure 4-10. The a-SiN layer is 450 Å thick. The fill factor was measured at 0.65 and the V_{oc} voltage was 0.83V. Samples with a-SiN n^+ layers, such as that used on the device of Figure 4-10, are currently being examined with ITO top contacts.

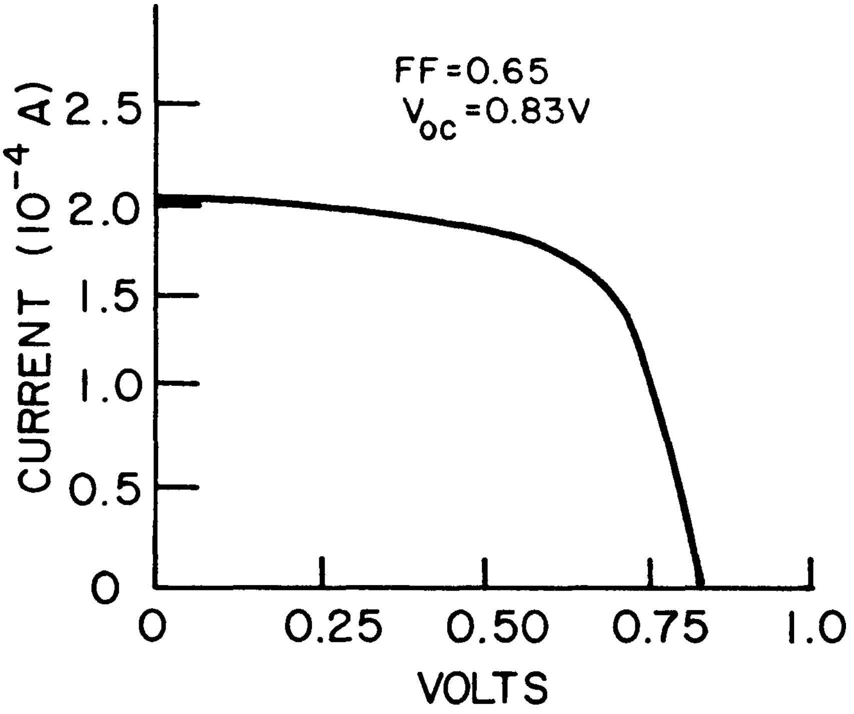

Figure 4-10. I-V Curve For A 0.05 cm^2 Amorphous Silicon Cell With An a-SiN n^+ Layer
Top electrical contact was made with a Cr dot.

4.4 Optical Modeling of Anti-Reflection Coatings

4.4.1 Introduction

The mechanisms which contribute to the loss of carriers in photovoltaic devices by limiting the short circuit current and the overall efficiency fall into two broad categories: optical losses and transport losses. This section concentrates on optical losses, which result whenever the incident flux is reflected from the front of the cell, or when the light is absorbed by a layer of the cell with high transport losses, such as the heavily doped layers of an a-Si:H photovoltaic device.

A standard 3M photovoltaic device is shown in Figure 4-11 and individual layer thicknesses are given in Table 4-1. The top contact is ITO which is a good transparent conductor with an index of refraction ($n = 2.0$). This value of n makes the oxide a good candidate for an anti-reflection coating as well. In order to be useful as an anti-reflection coating, the ITO layer must have an optical thickness given by $m\lambda/4$ where m is an odd integer, and λ is the wavelength at which the reflection is minimized [19]. Unfortunately, $\lambda/4$ thick ITO ($m = 1$) has a high sheet resistance (approximately 100 ohms/square) which limits the efficiency of the device due to voltage drops across the series resistance. Although the sheet resistance can be decreased to 30 ohms/square by increasing the thickness of the ITO layer, the bandwidth over which the layer serves as a good anti-reflection coating also decreases. Therefore, as the thickness of the ITO layer is increased--the simplest method of decreasing the sheet resistance--new strategies for minimizing reflective losses must be considered.

Table 4-1. Thicknesses Of The Deposited Layers Of The Standard 3M Photovoltaic Cell

Layer	Material	Thickness (nm)
d_0	MgF_2	Variable
d_1	ITO	Variable
d_2	n^+ a-Si	15
d_3	intrinsic a-Si	515
d_4	p^+ a-Si	20
d_5	nickel electrode	100
d_6	polyimide substrate	

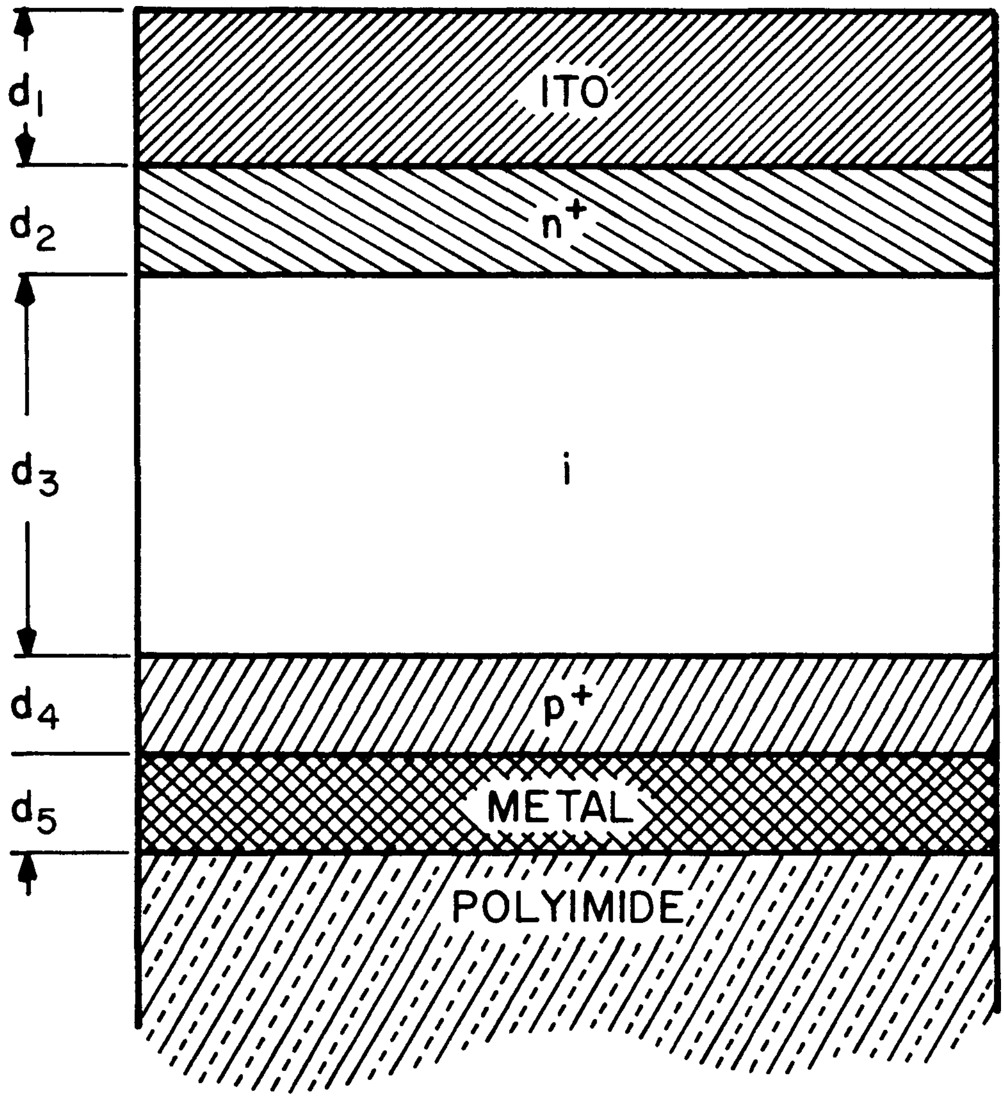

Figure 4-11. **The Standard 3M Photovoltaic Cell**
The layers are not drawn to scale: the thicknesses may be found in Table 4-1. The optical constants for the doped silicon layers were taken to be equal to the values for intrinsic a-Si.

Multi-layer anti-reflection coatings can incorporate ITO layers of 3λ/4 or thicker and still maintain low reflectance across the visible spectrum. For example, the reflectance of a cell with a very thick ITO overcoating can be lowered by overcoating with MgF_2 (n = 1.38) which acts as an anti-reflecting coating for ITO.

A further refinement involves inserting an intermediate optical layer between the Si and the ITO. A candidate material for this layer is a-SiN; currently under investigation as a possible indium diffusion barrier and n^+ layer. We have completely analyzed the first strategy (MgF_2 overcoating) and have begun modeling of the three-layer anti-reflection coating. Progress on the latter problem is currently awaiting measurements of the optical constants of the a-SiN material.

The questions which were answered by this theoretical study were the following:

- To what extent is the performance of the photovoltaic device hindered by thicker ITO layers?
- What fraction of the loss due to thicker ITO layers is restored by a MgF_2 overcoat?
- What is the optimum MgF_2 thickness for minimizing reflection losses?
- How sensitive are the results to the thickness of the ITO layer?

The last question addresses the problem of tolerances. If an improvement in the performance of a photovoltaic device were to require that an exact thickness of ITO be used, then the addition of a MgF_2 layer would be of no value.

As soon as the optical constants of the a-SiN layer are obtained experimentally, the same questions can be answered for the three-layer anti-reflection coatings. Preliminary results obtained by assuming the index of refraction n = 3 for a-SiN, are encouraging. These show reflections with 3λ/4 ITO to be as low as with the one-layer anti-reflection coating of λ/4 ITO.

4.4.2 Model

The objective of the calculation discussed in this section is to maximize the J_{sc} by minimizing the reflection from an a-Si:H photovoltaic device. The response of the cell under AM1 illumination depends on both optical and transport losses. The optical losses can be accurately modeled, and optical modeling is the major effort in the calculation. The transport losses, which are more difficult to model, are obtained from experimental data.

The standard cell shown in Figure 4-11 will serve as the model for the photovoltaic device. The optical modeling consists of solving Maxwell's equations for the multi-layer structure. In order to make the problem tractable, two simplifying assumptions are made: i) that the interfaces between the layers are perfectly smooth, and ii) that the light is incident normal to the photovoltaic cell surface. The only parameters required for the calculation are the optical constants n and k, and the thicknesses d_i of the various layers. The thicknesses are shown in Table 4-1. The solution of Maxwell's equations in the slab geometry of Figure 4-11 is straightforward; an excellent discussion may be found in Born and Wolf [19]. The computer program used was developed by internal personnel.

Although the discussion has dealt with reflection losses, the relevant question is: What amount of incident flux is absorbed in the intrinsic layer of the a-Si, where useful electron-hole pairs are created? A portion of the optical loss is due to reflection, but additional losses can occur. One loss mechanism involves absorption in the heavily-doped front layer where recombination lifetimes are short and recombination rates are correspondingly high. Even within the intrinsic layer not all of the electron-hole pairs, which are created, migrate to the terminals of the device, but recombine instead, and the calculation of the short circuit current density requires that the recombination losses be accounted for.

One way to account for recombination losses is to weight the results of the optical modeling using the short circuit spectral response of the device. The spectral response of a device is basically the current collected for illumination at a specified wavelength at a constant photon flux. Although several model calculations exist, we have elected to use an actual experimental spectral response curve in the optimization calculation. See Figure 4-12 . Since the experimental spectral response results also include an optical loss component, the spectral response must be normalized against the optical loss. For the particular response curve shown in Figure 4-12, the semiconductor layers were coated with a chrome dot, resulting in the cell structure shown in the inset. The result of the optical modeling on a chrome dot cell is shown in Figure 4-13.

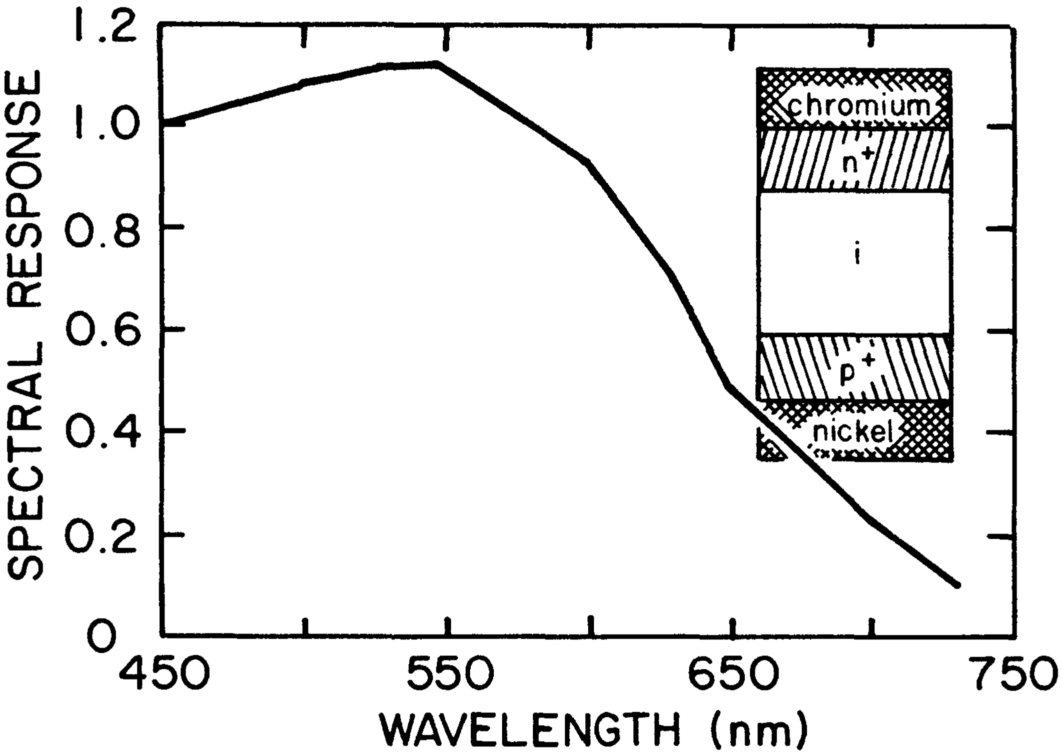

Figure 4-12. **The Spectral Response Curve For A Chrome Dot Cell**
The current is arbitrarily normalized to 1.0 at $\lambda = 600$ nm. For cells used in the spectral response measurement the ITO layer has been replaced by a thin (10 nm) layer of chromium as shown in the inset.

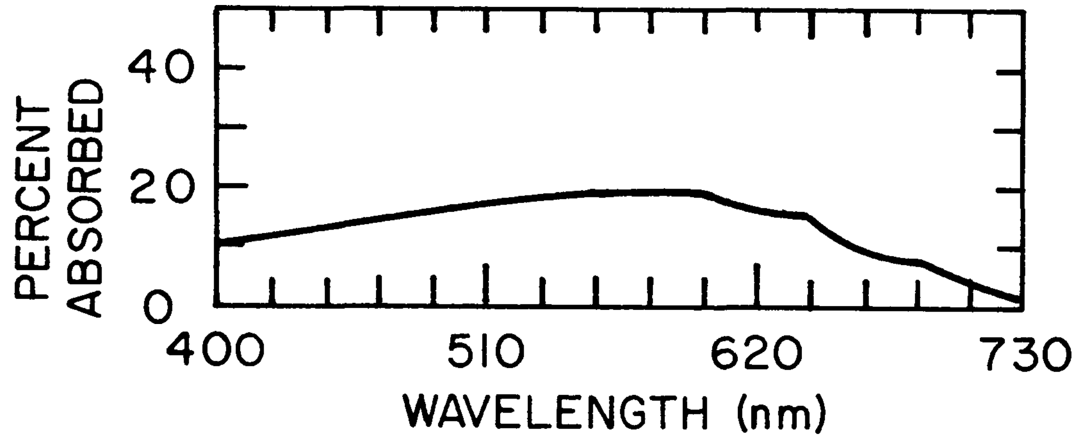

Figure 4-13. The Absorption In The Intrinsic Layer As A Function Of Wavelength For The Test Cell Shown In Figure 4-12
The low absorption in the intrinsic layer is due to high absorption in the chrome layer. The similarity between the absorption curve and the spectral response curve indicates minimal diffusion losses in the blue.

The final factor in the calculation is the spectral distribution of flux at AM1. The values obtained from Reference 20 were used as shown in Figure 4-14. The spectral distribution of flux is almost flat across the visible portion of the spectrum; therefore, a high order integration routine is not needed.

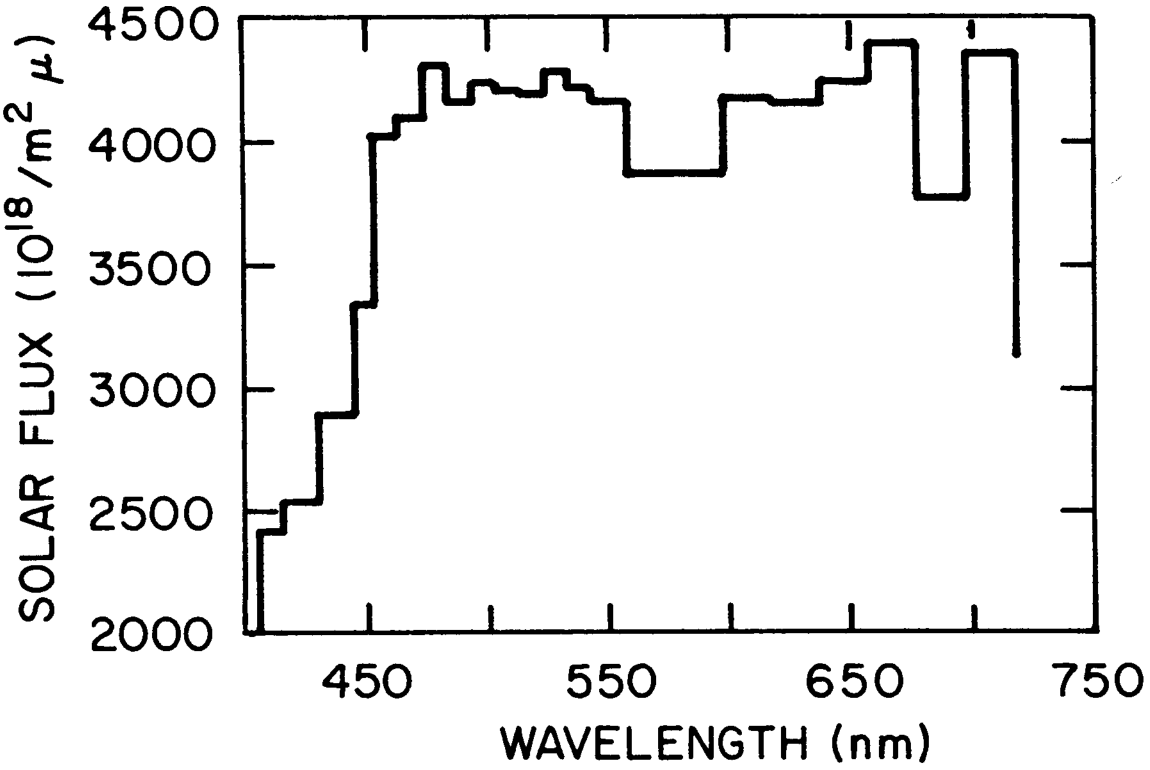

Figure 4-14. **The Spectral Distribution Of Flux At AM1**
Since the values fall rapidly below 450 nm, the solar spectrum determines the λ_{min} cutoff in the integral.

The three weights are multiplied together and integrated over all wavelengths to obtain the final result for the short circuit current density:

$$J_{SC} = \int_{\lambda_{min}}^{\lambda_{max}} \frac{\partial \eta_\odot}{\partial \lambda} R(\lambda) \frac{A_i(\lambda)}{A_i'(\lambda)} d\lambda \qquad \text{(Equation 4-1)}$$

$\partial \eta_\odot / \partial \lambda$ = spectral distribution of flux

$R(\lambda)$ = spectral response at λ

$A_i(\lambda)$ = percent of incident flux absorbed in the intrinsic layer of the ITO coated cell

$A_i'(\lambda)$ = percent of incident flux absorbed in the intrinsic layer of the chrome dot coated test cell

The integral was evaluated numerically using simple summation:

$$J_{SC} \approx \sum_i \left. \frac{\partial \eta_\odot}{\partial \lambda} \right|_{\lambda_i} \cdot R(\lambda_i) \cdot \frac{A_i(\lambda_i)}{A_i'(\lambda_i)} \Delta_i \qquad \text{(Equation 4-2)}$$

and a more complicated Simpson's Rule integration:

$$J_{SC} \approx \sum_i \left. \frac{\partial \eta_\odot}{\partial \lambda} \right|_{\lambda_i} \cdot \int_{\lambda_i - \Delta_i/2}^{\lambda_i + \Delta_i/2} R(\lambda) \frac{A_i(\lambda)}{A_i'(\lambda)} d\lambda \qquad \text{(Equation 4-3)}$$

that is sensitive to the rapid variation of A_i. Both techniques yielded identical values.

Before discussing the results of the calculation, a return to the issue of optical constants is in order. The optical functions are obtained from a variety of sources. For Ni and Cr, values tabulated from careful bulk measurements are used [21]. The index of refraction of ITO and MgF_2 are assigned the values 2.00 and 1.38, respectively. The absorption coefficient, k, is assumed to be small and constant (0.001) for both materials. The optical constants for a-Si:H are more difficult to obtain since the values reported in the literature and in internal laboratory measurements vary widely. (Indeed, the variation in optical constants is very likely due to differences in materials preparation. This fact suggests the need for careful optical measurements on laboratory samples.) Finally, values from Reference 22 were chosen as representative. The lack of unambiguous optical constants prohibits an absolute calculation of the current density; nevertheless, it is believed that the calculation will be useful in determining the relative merit of various cell overcoat layers.

4.4.3 Results

The results of the calculation attempt to answer the four questions posed in the introduction. They are summarized in Figures 4-15 through 4-20.

In Figure 4-15, the J_{sc} is plotted as a function of the ITO thickness for a cell without a MgF_2 overcoat. The current at a $\lambda/4$ thickness of ITO, which is nominally 550 nm, is arbitrarily normalized to 1. The current is clearly maximized for a $\lambda/4$ cell with local maxima at $3\lambda/4$ and $5\lambda/4$. The current is decreased by 13% for a $3\lambda/4$ coating and by 20% for a $5\lambda/4$ coating. An appreciable decrease in carrier pair creation results as the ITO thickness is increased in order to lower the sheet resistance.

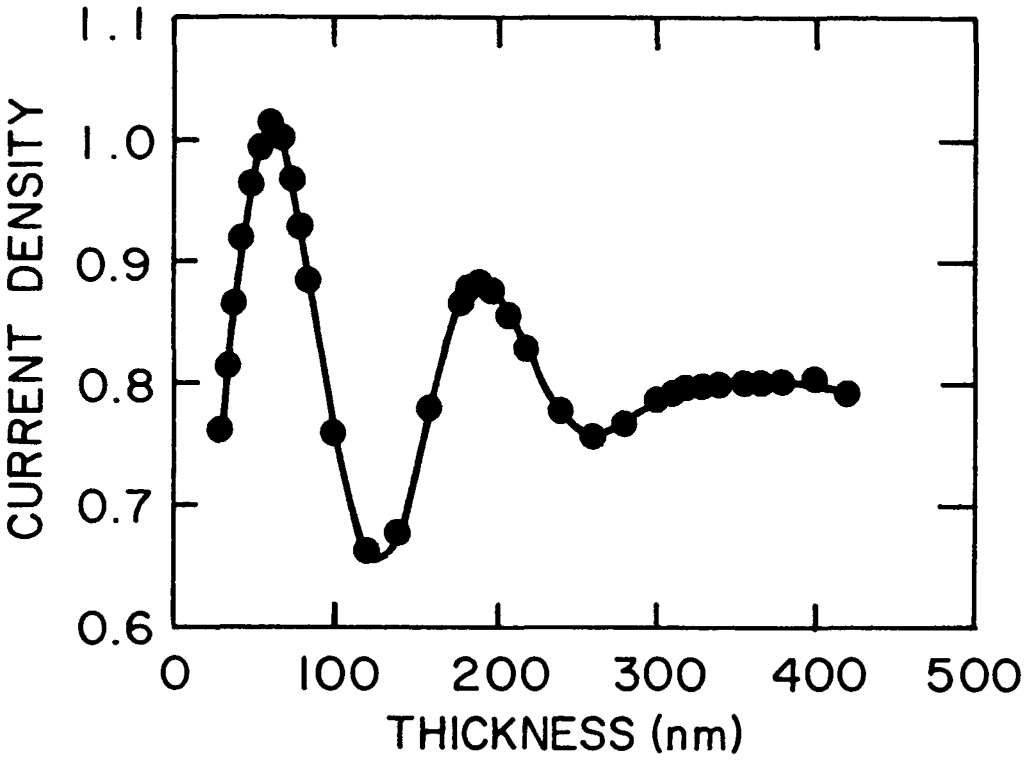

Figure 4-15. The Short Circuit Current Density As A Function Of ITO Thickness
In this case, no MgF_2 layer is used. The peaks occur where ITO is a good anti-reflection coating.

One question arising from the discussion of optical losses in a-Si:H solar cells is: Where do the losses occur? This question can be answered by considering Figure 4-16. The lower curve in the figure represents the percentage of light absorbed as a function of wavelength for a cell with a $3\lambda/4$ ITO layer without MgF_2. The upper curve shows one-minus-the-reflection. At 400 nm only 22% of the light is absorbed within the intrinsic layer, and only 48% of the light is reflected from the cell. Since α is large ($\alpha \sim 0.057$ nm^{-1}), no light penetrates to the back of the intrinsic layer; therefore, the remaining 30% of the light is absorbed in the n^+ layer. At 550 nm the light still does not penetrate beyond the back of the intrinsic layer. Although almost no light is reflected, only 86% is absorbed in the intrinsic layer. The remaining 14% is absorbed in the n^+ layer. The situation at 715 nm is different. The reflection is again almost 0, but α is small and the silicon is only weakly absorbing. Very little of the remaining 78% of the light is absorbed in the heavily doped layers. Instead, the light is absorbed in the Ni bottom electrode layer.

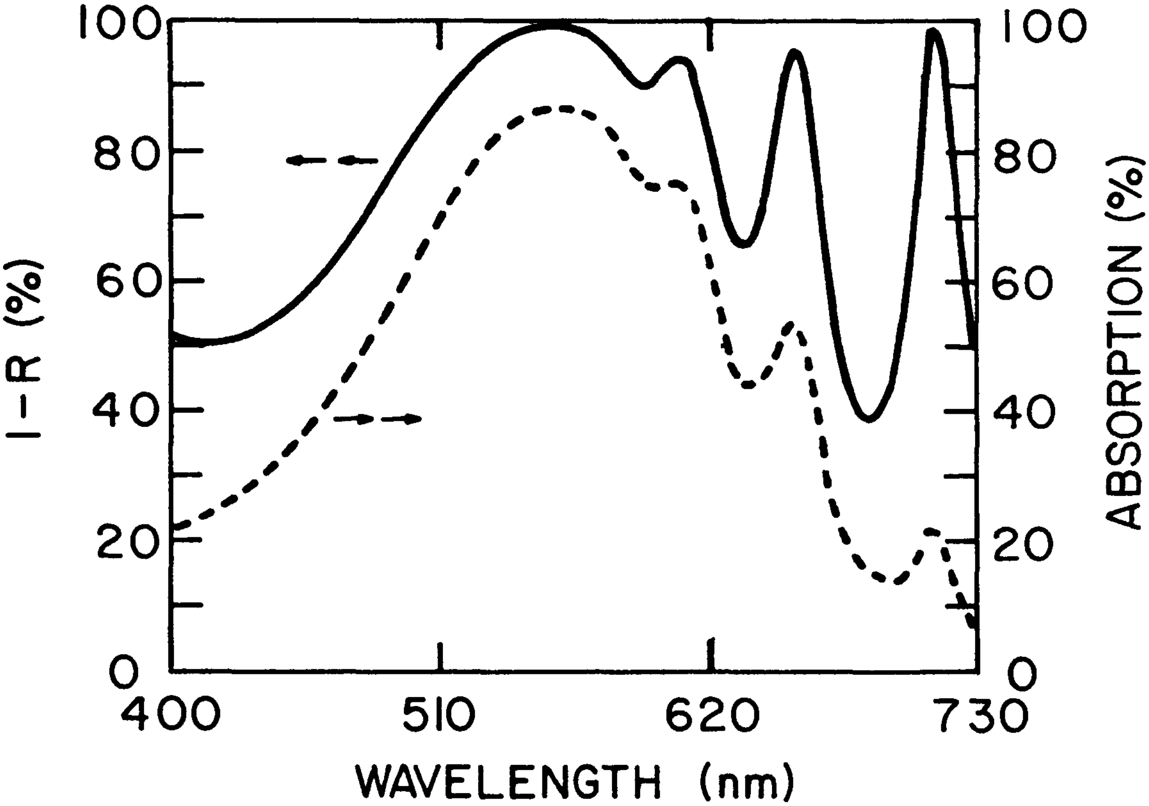

Figure 4-16. Absorption And Reflection As A Function Of Wavelength At short wavelengths (< 550 nm) the difference between absorption in the intrinsic region and reflection is a measure of the absorption in the n^+ layer. At very long wavelengths, the difference is due to absorption in the metal back reflector.

In Figure 4-17, the calculated results for cells with various MgF_2 overcoat thicknesses are shown. For λ/4 ITO, the cell performance is actually diminished by any thickness of MgF_2 overcoat considered. For 3λ/4 ITO, the cell performance is maximized by 103 nm of MgF_2. For 5λ/4 ITO, the cell performance is maximized by 93 nm of MgF_2. In neither case does the cell recover what is lost in going to thicker ITO. The striking feature of these results is that only a 3.8% gain in J_{sc} can be expected from overcoating a 3λ/4 cell, but a 9.4% gain can be achieved when overcoating a 5λ/4 cell, which yields a performance equal to the 3λ/4 cell. All other considerations being equal, a 5λ/4 cell with lower sheet resistance and equal optical performance is preferable to a 3λ/4 cell.

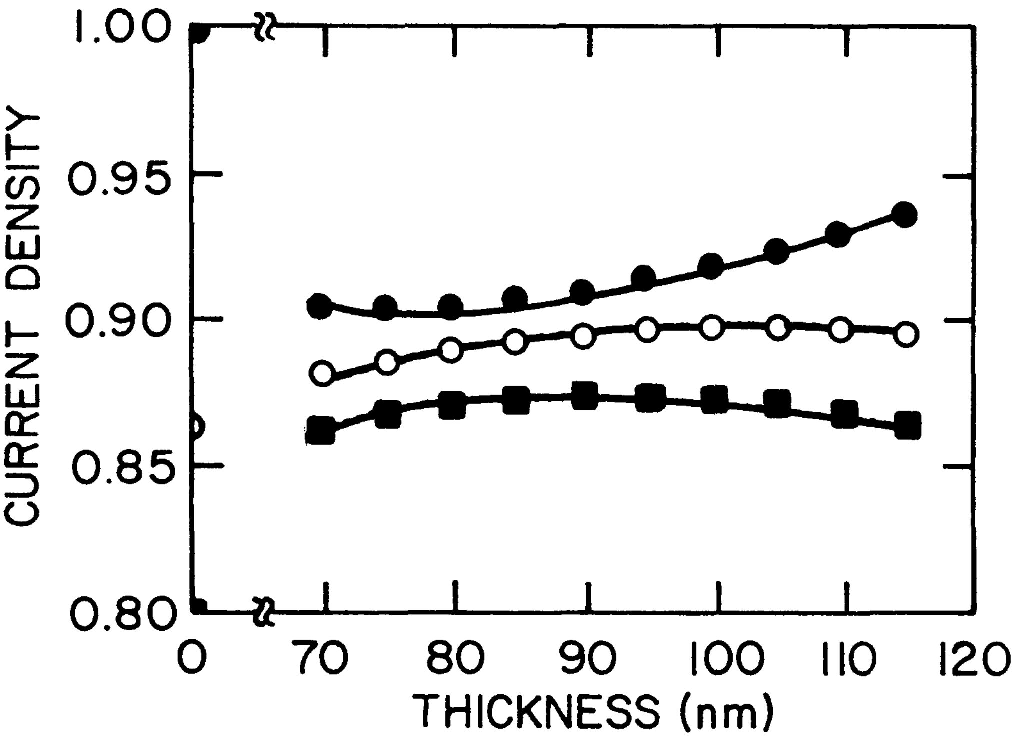

Figure 4-17. **Short Circuit Current As A Function Of MgF_2 Overcoat** The results are normalized to 1.0 for $\lambda/4$ ITO. The absorption for ITO only is shown along the left axis. The ●'s are $\lambda/4$; the o's are $3\lambda/4$; and the ■'s are $5\lambda/4$.

Figures 4-18, 4-19 and 4-20 address the question of how sensitive the results are relative to the thicknesses of the various layers. As was shown in Figure 4-17, cell performance is not sensitive to the thickness of the MgF_2 over a range of ±10 nm. If the cell is similarly insensitive to the ITO thickness, then we may hope to realize the improvements discussed above without excessively restrictive tolerances. It is also useful to compare the dependence of J_{sc} on the ITO thickness for cells with ITO only, and cells with an MgF_2 overcoat. The results of varying the ITO thickness by $\pm$ 20 nm with no MgF_2 overcoat are shown in Figure 4-18. Figure 4-19, shows the results for a nominal $3\lambda/4$ cell. Without a MgF_2 layer, the current varies by 8%, however, with a 103 nm thick layer of MgF_2, the variation is only 2%. Even though the MgF_2 overcoat improves the performance of high quality $3\lambda/4$ cells only marginally, it ensures optimal performance from cells with a less-than-optimal ITO thickness. The results for a nominal $5\lambda/4$ cell are different, as shown in Figure 4-20. Cell performance is independent of the ITO thickness over the range of ±20 nm for both cases—ITO alone and ITO with an MgF_2 overcoat. In this case, the conclusion is that the enhanced performance of a MgF_2 coated cell is not sensitive to the ITO thickness.

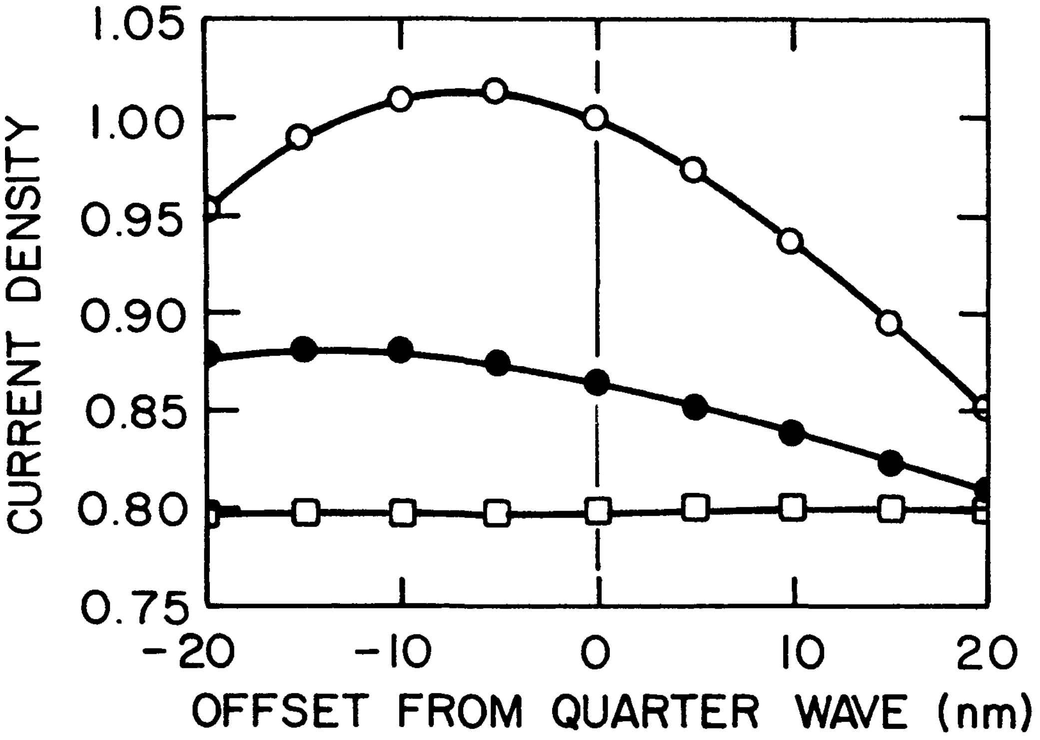

Figure 4-18. Short Circuit Current As A Function Of ITO Thickness With No MgF_2 Overcoat
The o's are the variation about λ/4; the •'s are the variation about 3λ/4; and the □'s are the variation about 5λ/4.

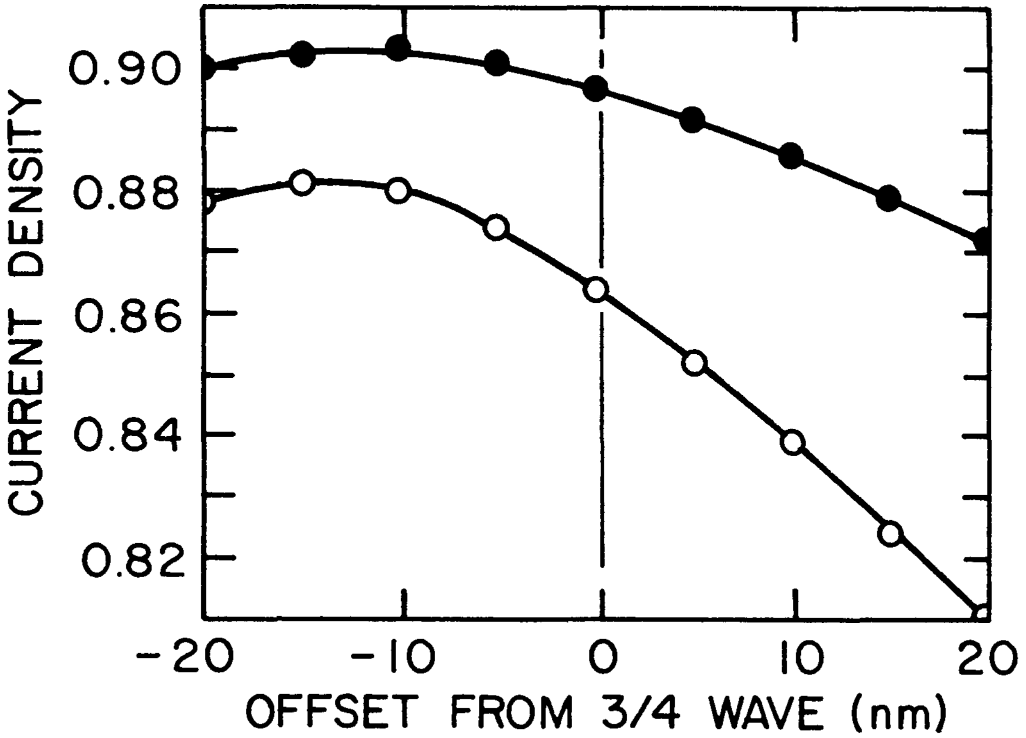

Figure 4-19. Variation In The Short Circuit Current As ITO Thickness Varies For ITO Only (o) And A 102.25 nm (●) Thickness of MgF_2 The ITO thickness varies about $3\lambda/4$.

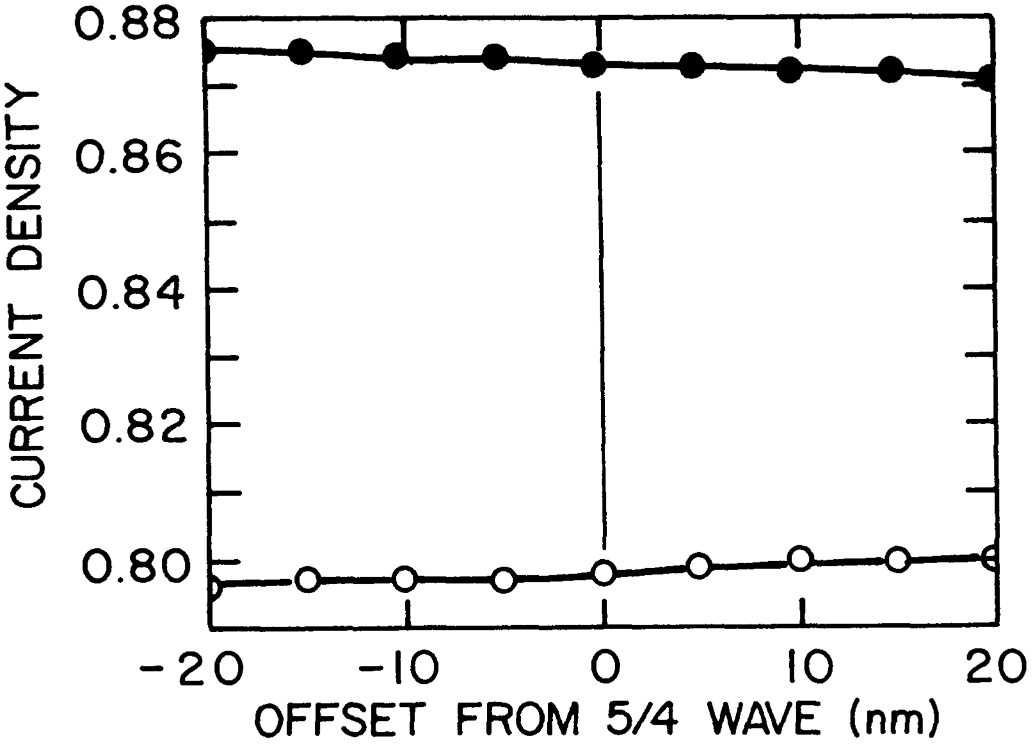

Figure 4-20. Variation In The Short Circuit Current As ITO Thickness Varies For ITO Only (o) And A 92.25 nm (●) Thickness of MgF_2 The ITO thickness varies about $5\lambda/4$.

Figure 4-21 shows the reflectance from the standard cell (Table 4-1), with a three layer anti-reflection coating consisting of $\lambda/4$ a-SiN, $3\lambda/4$ ITO and $\lambda/4$ MgF_2. We assumed that $n = 3.0$ and $k = 0.1$ for the a-SiN. These are good approximations for n and k from 550 to 700 nm, but not for the blue region of the spectrum, where n and k increase slightly. More accurate modeling and experimental verification will be performed after completion of the a-SiN work.

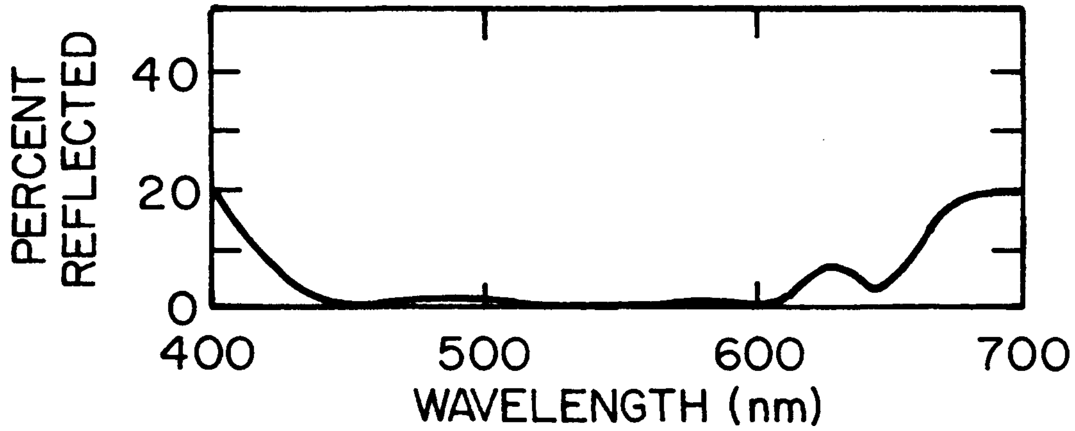

Figure 4-21. **Calculated Reflectance From The Standard Cell (Table 4-1) But With a-SiN n^+ Layer, $\lambda/4$ Thick, $3\lambda/4$ ITO And $\lambda/4$ MgF_2**
λ = 560 nm.

4.4.4 Conclusions

4.4.4.1 Two-Layer Anti-Reflection Coating

The results of optical modeling indicate that the best J_{sc} occurs for a $\lambda/4$ thickness of ITO. Thicknesses greater than this give lower J_{sc}, even when the cell has a MgF_2 overcoat. The decision to increase the ITO thickness must be determined by balancing series resistance losses against optical losses.

The results of optical modeling indicate that the loss in J_{sc} need not be larger than 12.5%. In fact, the optical losses for $5\lambda/4$ thick ITO layers with optimized MgF_2 overcoat layers are only marginally greater than $3\lambda/4$ thick ITO layers. All other considerations being equal, the $5\lambda/4$ thickness with a MgF_2 overcoat is preferred to the $3\lambda/4$ thickness of ITO because of its lower sheet resistance.

The results of our calculation indicate only one case when a $\lambda/4$ thick ITO layer is present, where the MgF_2 overcoat actually reduces the cell performance.

4.4.4.2 Three-Layer Anti-Reflection Coating

Preliminary results indicate that a three-layer anti-reflection coating with $3\lambda/4$ ITO can achieve reflectances as low as the single layer $\lambda/4$ ITO layer.

4.5 Two Chamber System

For the single deposition zone chambers used in previous work, dopant carry-over from the n^+ and p^+ layers into the intrinsic layer was common. As discussed in Section 4.2.2, an intrinsic layer deposited after a p^+ layer has as much boron in it as if the gas mixture contained 20 ppm of diborane. This cross-contamination is believed to have an appreciable effect in reducing the fill factor of our devices. A multiple deposition chamber system is required to control this problem.

A two chamber system (System Five) was designed and made operational. In this system, the substrate passes from a feed roll through conductance limiting slits between the deposition chambers, and finally onto a take-up roll. The conductance limiting slits, through which the web enters and leaves each deposition chamber, prevent back diffusion of impurities into the deposition zones. During operation, the pressure in the deposition chambers is held at 1 torr while the pressure outside the slits is 100 to 200 millitorr. Using data that was generated from the back diffusion studies, contaminants in the deposition zone should be five orders of magnitude less than the contamination level outside the deposition zone.

In System Five the fabrication of a device begins with a hydrogen etch of the substrate in the doped layer chamber followed by the deposition of a p^+ layer. The web is then wound forward into the intrinsic layer deposition chamber where a 5000 Å thick intrinsic layer is deposited. Finally, the web is wound backwards so that the device area is once again in the doped layer chamber where the n^+ top layer is deposited.

Figures 4-22a through 4-22d show SIMS depth profiles of a device made in a single chamber system and of one made in the new two-chamber system, respectively. The curves show the boron, phosphorous, oxygen, carbon, and nitrogen profiles for the devices. The key feature is the boron level within the intrinsic layer. As expected, the drop-off is much more abrupt for the two-chamber system than for the single chamber system.

System Five will be used exclusively to develop devices. Boron composition studies will be performed to allow efficiency and stability characteristics to be evaluated. The design of the two small deposition chambers is similar to that used in the Task Five multi-chamber deposition system. Different internal geometries will be evaluated as design candidates for application in the larger system. Deposition conditions developed in the two-chamber system will continue to be used for guidance in establishing deposition conditions in the multi-chamber system.

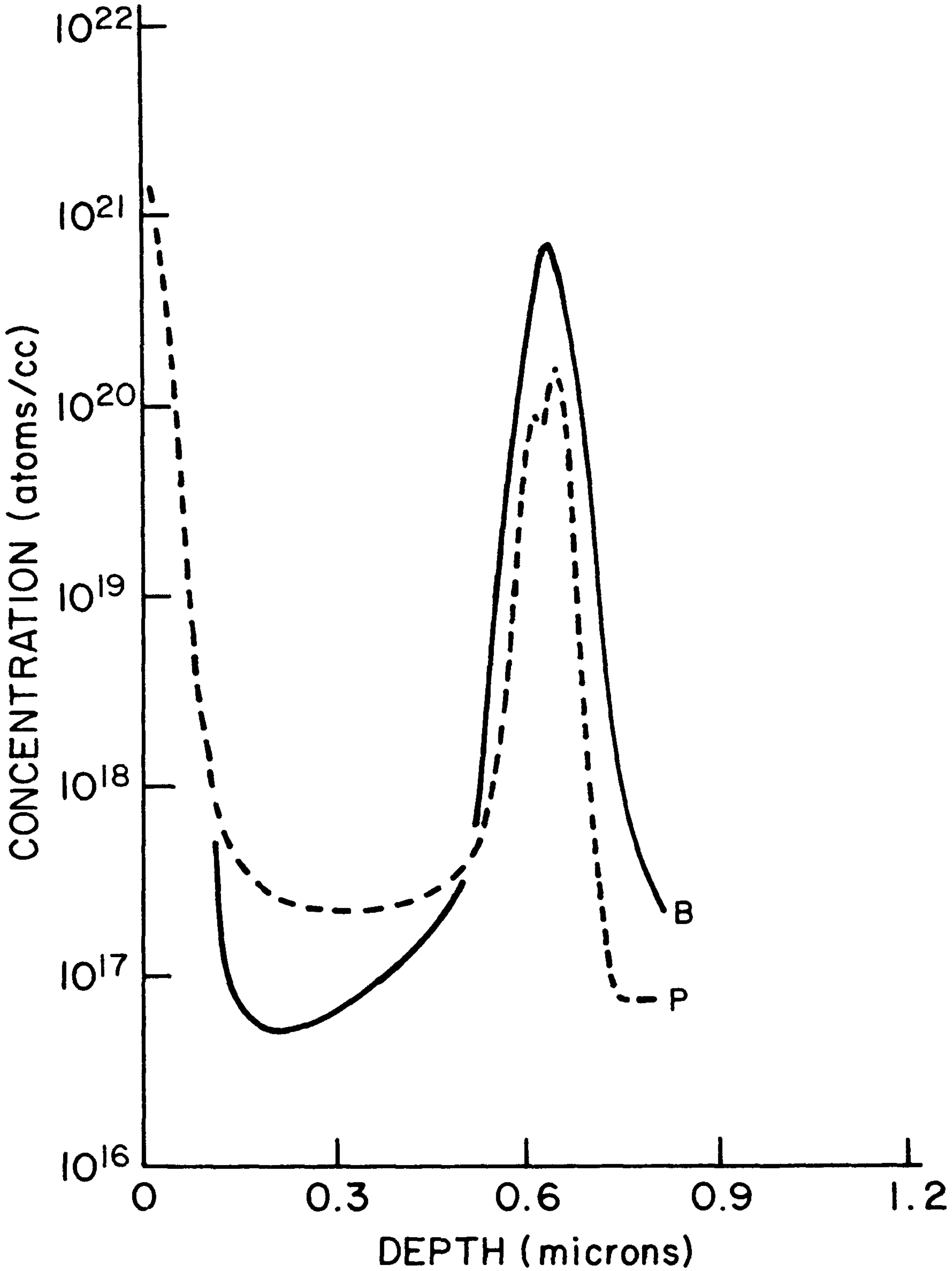

Figure 4-22. (a) SIMS Depth Profile Of Device Made In Single Chamber System

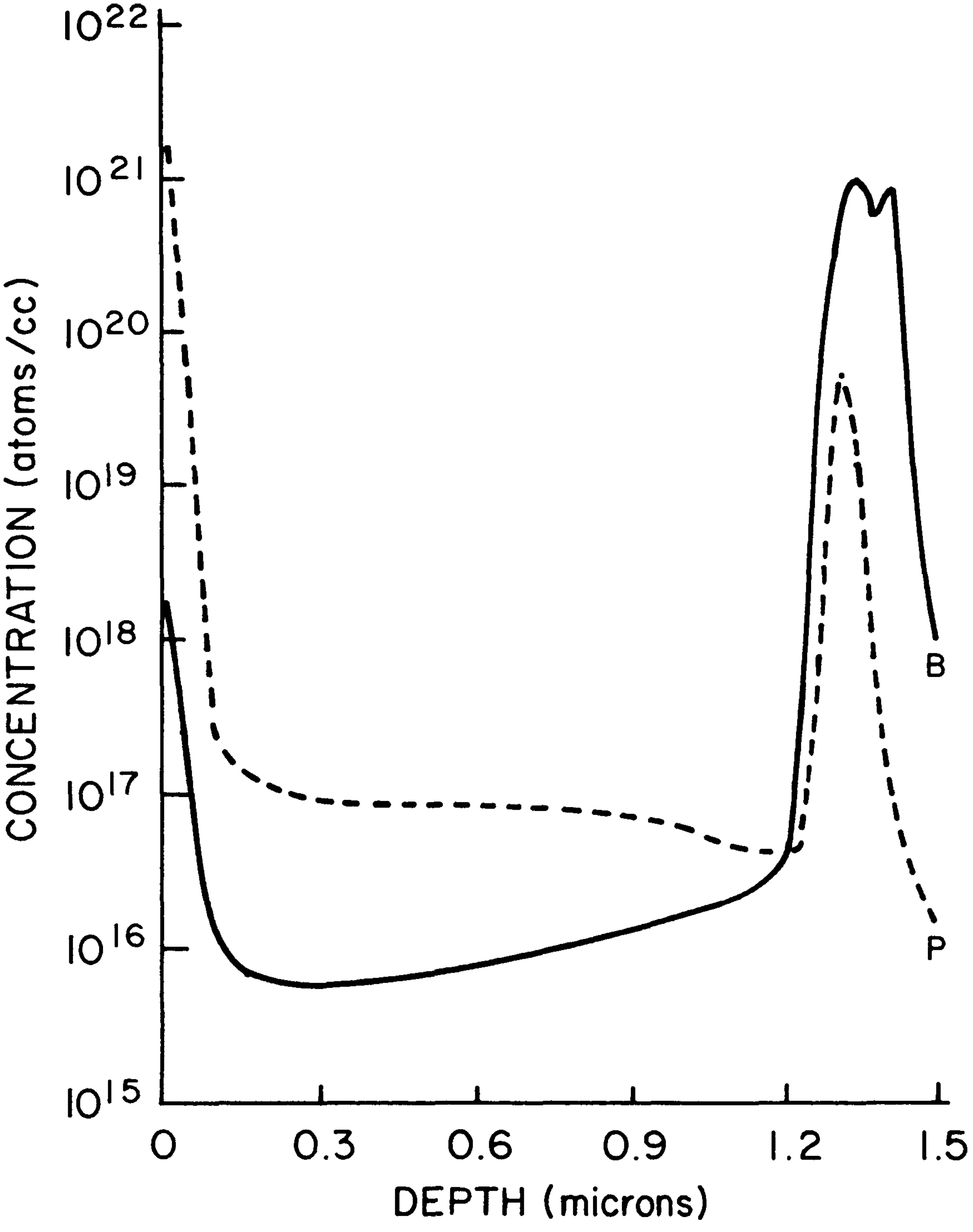

Figure 4-22. (b) SIMS Depth Profile Of Device Made In Two-Chamber System

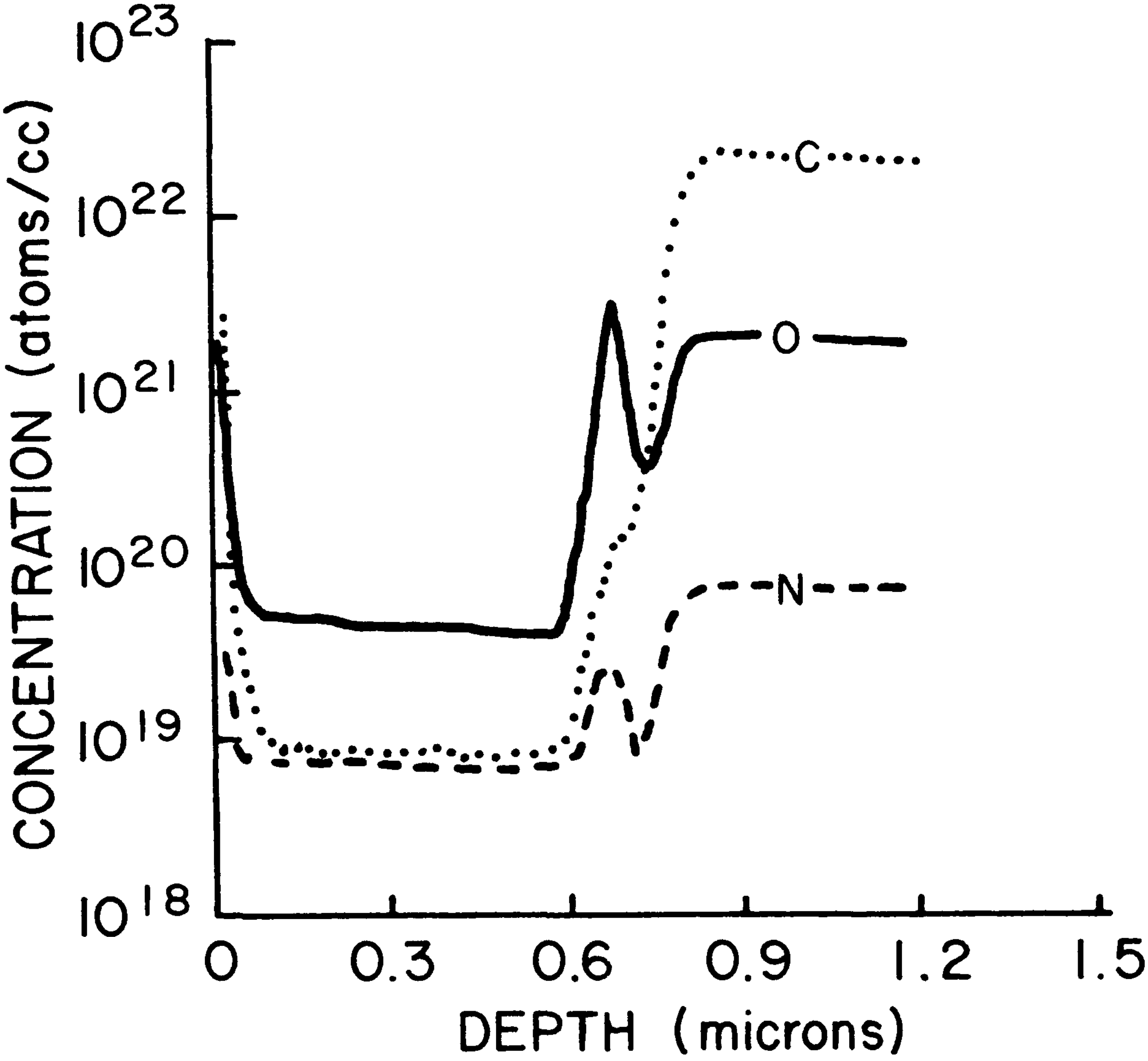

Figure 4-22. (c) SIMS Profile Of C, O, And N For Device Made In Single Chamber System

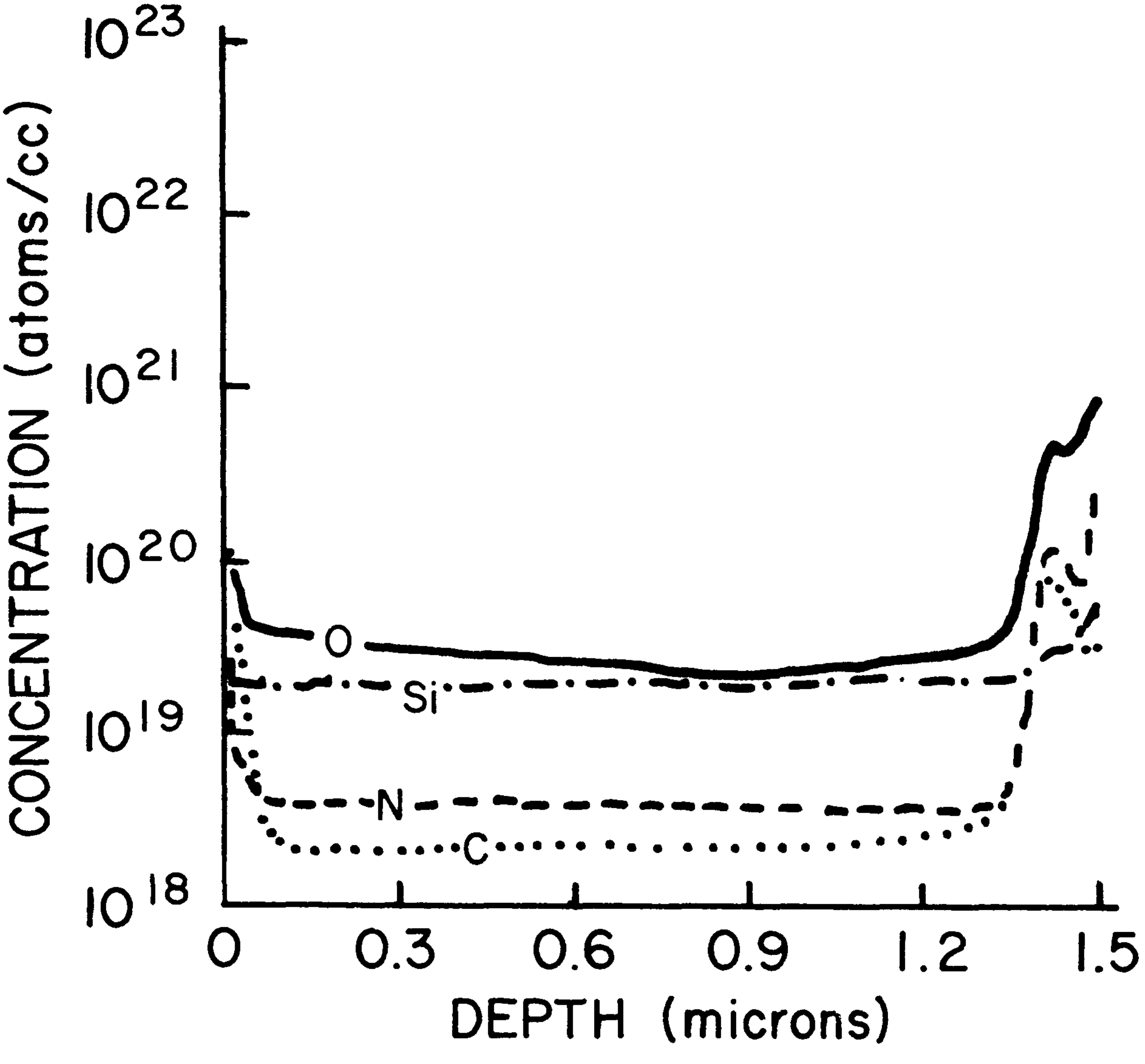

Figure 4-22. (d) SIMS Profile Of O, C, And N For Device Made In Two Chamber System

One of special design features in System Five, which is an improvement over the other single chamber systems, is the incorporation of removable mandrels for holding the substrate web. These mandrels are interchangeable with those used in the metallization system. As discussed in Section 3.1, dust attracted to the web is the prime source of shunt defects. By using interchangeable mandrels, transfer steps are eliminated, thus ensuring that the web surfaces are only exposed when in a vacuum system or a dust-free glovebox. This process greatly reduces the possibility of dust particles contacting the web and this should reduce defects in the devices.

4.6 The Effects of Boron Profiles on the V_{oc} of P-I-N and N-I-P a-Si Devices

Considerable amounts of data [23] have been published in recent years showing a difference in the V_{oc} between the p-i-n and n-i-p a-Si solar cell configurations. Likewise, there have been a number of explanations for the effect [24, 25, 26]. In this section, data on the effect of boron profiles on V_{oc} are presented and various models in view of that data are discussed.

Explanations for differences in the V_{oc} have included effects which depend on whether the illumination comes through the n^+ or p^+ layer, such as the Dember effect. Other explanations are based on differences in the device structure, such as dopant trailing into the intrinsic layer or differences in the layers depending on the order of growth. Kanagai et. al. [27] have shown that devices on glass, with a transparent layer for both contacts, show little dependence of V_{oc} whether the cell is illuminated from the n or p side. The conclusion follows that the differences in V_{oc} must arise from physical differences within the p-i-n and n-i-p devices. The remaining possibilities are: i) boron profiling into the i-layer from the p/i interface enhancing the V_{oc}, ii) phosphorous profiling from the n/i interface degrading the device, and iii) differences in the structure or defect level in a given layer depending on the order of growth. To further investigate this, it is important to focus on the mechanism which limits V_{oc}. V_{oc} is the point where some carrier loss mechanism (recombination current or forward bias diode current) equals the photogeneration rate. The most detailed modeling to date has been done by Hack and Shur [26]. They conclude that for devices with low built-in potentials (V_{bi}), the V_{oc} is controlled by the forward bias current characteristics of the diode and may be affected by boron profiling. For devices with a high V_{bi}, V_{oc} is controlled by recombination within the i-layer and should not be affected by the boron profile. They predict that boron profiling may increase the V_{oc} of low V_{bi} devices by about 50 mV. In general, the results presented here confirm the predictions of the model, but also suggest other factors.

To test the effects of profiling, a system was utilized which consists of separate chambers for depositing the doped and intrinsic layers. This allows sharp interfaces to be created between each of the doped layers and the intrinsic layer. Thus, starting with no carry-over of dopant into the i-layer, a series of samples was produced with boron and phosphorous profiles of well specified concentrations and depths into the i-layer by introducing ppm levels of dopants in the intrinsic chamber during deposition.

Figure 4-23 is a plot of the V_{oc} versus the boron profile depth of a fixed concentration for p-i-n and n-i-p devices. The B_2H_6 level in the deposition chamber, while depositing the profile, was 100 ppm relative to the SiH_4.

Even at this low level of doping, a very narrow profile is required to bring the V_{oc} up to a saturation level. It should be emphasized that the n-i-p device configuration has a boron profile with a very sharp onset associated with turning the B_2H_6 flow on, while the p-i-n configuration has a more smeared, decaying profile associated with turning the B_2H_6 flow off. This difference would easily explain the offset between the p-i-n and n-i-p curves shown in Figure 4-23.

The first noteworthy item is that for p-i-n and n-i-p devices with no dopant carry-over, the V_{oc} values were identical. This shows firstly, that it is indeed the carry-over, rather than a deposition sequence related variation that causes the normally observed differences in V_{oc}. Secondly, there was no observed effect on V_{oc} from adding a phosphorous profile from the n-interface. This leaves the boron profile as the primary cause of variation in the p-i-n and n-i-p devices.

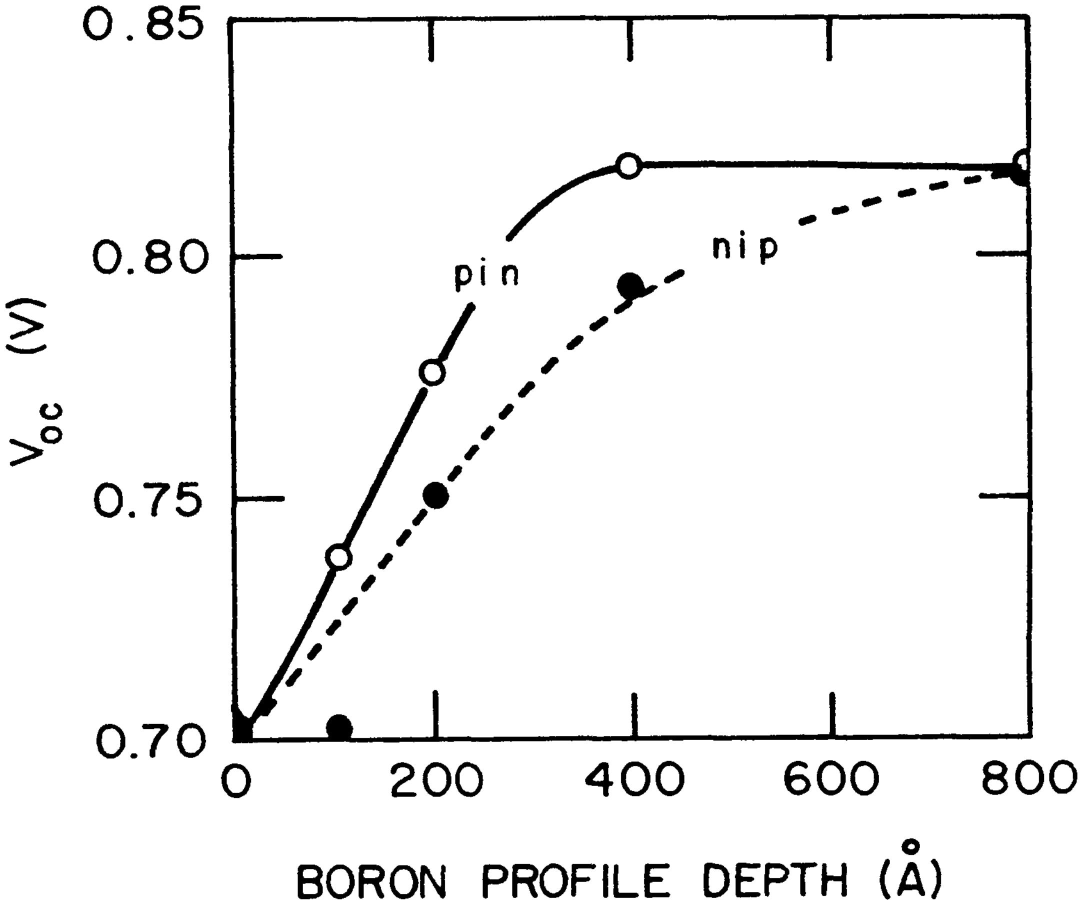

Figure 4-23. **V_{oc} Versus The B-Profile Depth Of A Fixed Concentration For p-i-n And n-i-p Devices**

To further investigate this effect, a series of samples were fabricated having a fixed profile depth of 200 Å and variable boron concentrations. The results are shown in Figure 4-24. It appears that a profile depth of 200 Å is adequate to reach the saturation level of V_{oc} if the B concentration is high enough. Clearly then, for the samples without boron profiling, V_{oc} is not limited by the bulk recombination current, or modification of 5% of the intrinsic layer would not have such a great effect. The V_{oc} must then be controlled by either the forward biased diffusion current or a high recombination current at or near the p/i interface.

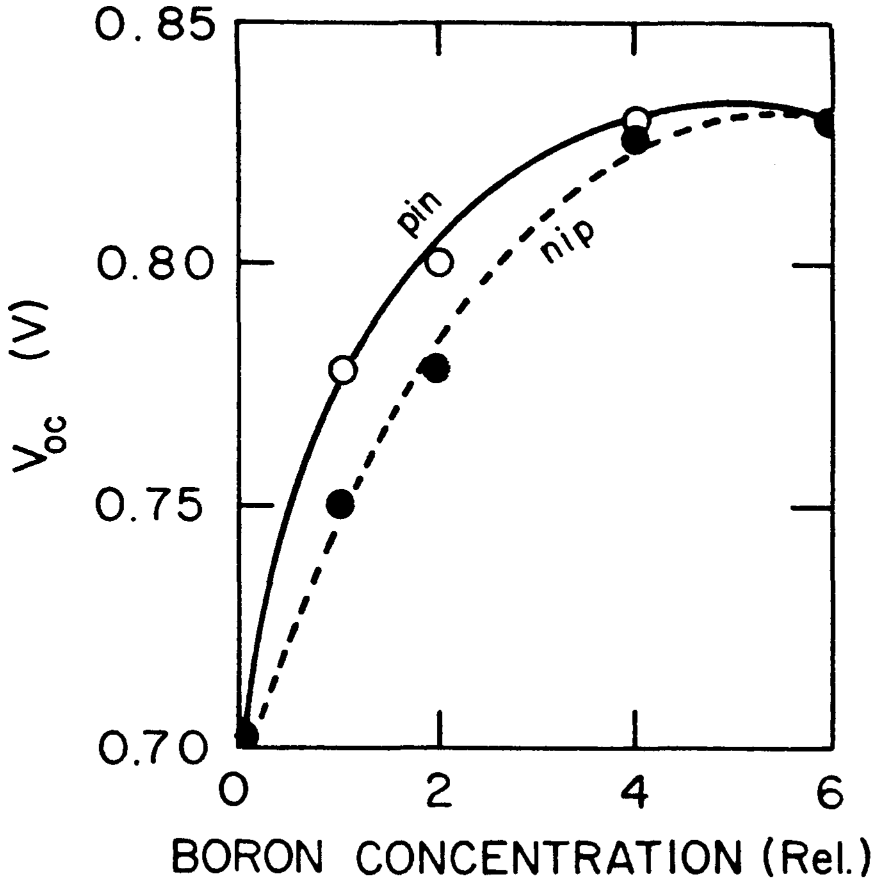

Figure 4-24. V_{oc} Versus B-Concentration For A 200 Å Deep B-Profile

As mentioned earlier, Hack and Shur predict that for a low V_{bi}, the V_{oc} will be controlled by the forward bias diffusion current which is determined by the effective barrier potential of the device (the largest barrier of the two interfaces). If the effective barrier potential is increased, V_{oc} will rise and ultimately be limited by the bulk recombination current. This can be accomplished either by increasing the total V_{bi} or modifying the field distribution within the intrinsic layer using a dopant profile so that some potential drop is moved from the lower interface barrier to the higher one.

Qualitatively, our results agree with this model, however, the model predicts the maximum effect of the boron profiling to be 50 mV. Additionally, it is questionable whether such a narrow, abrupt profile would cause the necessary change in the two barrier heights.

An alternative possibility would be that the current controlling the V_{oc} in the low voltage case is due to surface recombination of electrons which tunnel to the p-i interface. At V_{oc} conditions, the depletion width collapses, leaving a very narrow E field spike at the interface, thus the electron density in the conduction band near the interface increases greatly. A narrow boron profile adjacent to the interface in the i-layer would extend the field region and reduce the density of electrons available for recombination near the interface. A higher V_{bi} would also reduce the surface recombination by producing a larger E field spike at the interface. Surface recombination controlling V_{oc} would also explain the sensitivity to contaminants at the p-i interface.

Further work will be required in order to make a determination of the relative importance of surface recombination current and forward bias diffusion current. It does, however, appear that bulk recombination creates an upper limit to V_{oc}.

4.7 Device Performance Characteristics

The table below shows electrical characteristics measured at 3M for photovoltaic devices fabricated on polyimide substrates. The first column shows typical device values which were observed on a routine basis. The second column shows the best values observed to date on our standard structure. Currently, the two main factors limiting efficiency are low red response due to the absence of light trapping and low fill factors which are believed to be due to contaminants in the i-layer.

Table 4-2. Typical And Best Characteristics For Photovoltaic Devices On Polyimide Substrates

Parameters	Typical	Best
FF	0.61	0.65
J_{sc} (mA/cm^2)	11.5	13.5
V_{oc} (Volts)	0.88	0.90
Eff (%)	6.5	7.2

5.0 TASK FOUR - MONOLITHIC, INTRA-CONNECTED CELLS/SUBMODULE RESEARCH

5.1 Series Connected Submodule Design

A feasible design candidate for a monolithic, series-connected sub-module structure is shown in Figure 5-1. Using this configuration, electrical power losses due to the series resistance of the individual solar cells, and light blockage resulting from conductive grid structures are minimized.

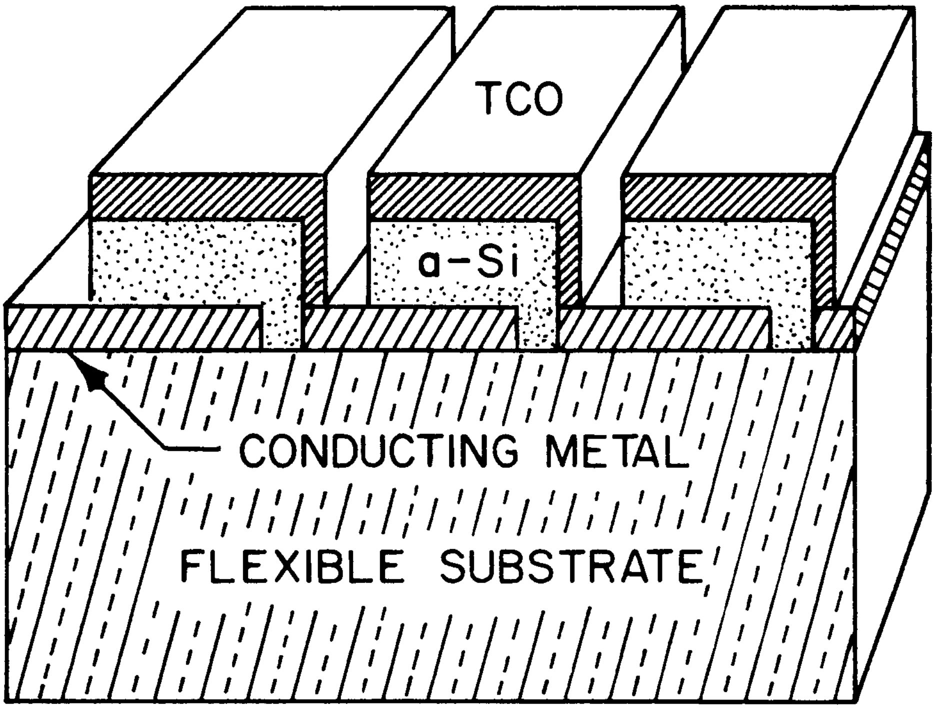

Figure 5-1. Submodule Design Concept
TCO refers to Transparent
Conductive Oxide.

The submodule design shown in Figure 5-1 is the preferred type of structure for large area flat arrays. In the finished device, the dimensions to be used can be estimated from the materials properties. Of greatest concern will be the overall efficiency of the finished submodule. The resultant efficiency can be calculated assuming that the losses in the top and bottom conductive layers are exclusively ohmic in nature [28-32] . The transparent conductive oxide (TCO) layer is responsible for most of the ohmic loss. This is because the sum of the sheet resistances of the conductive layers is almost entirely due to the TCO sheet resistance and the interconnect resistance of the TCO layer to the bottom (metal) conductive layer of the adjoining cell. In the Semi-Annual Report No 2, under subcontract ZB-4-03056-2, dated June, 1985, the design parameters were established which are expected to be used in solar cell construction. These parameters were derived in order to establish a baseline submodule design goal, and are given in Table 5-1 [33].

Table 5-1. Target Submodule Parameters

web length	up to 100.00 cm
web width	= 10.00 cm
scribe width	= 0.02 cm
sheet resistance of top contact	= 10.00 ohm/sq
short circuit current density	= 16.00 mA/cm^2
small area power output (AM1)	= 11.10 mW/cm^2
cell width	= 0.50 cm

5.2 Series Connected Submodule Construction

To produce the series connections in the submodules, two of the techniques which appear to be the most favorable are chemical etching and laser scribing [33]. While chemical etching is well suited to submodule prototype fabrication, the laser scribing approach will be utilized in future large-scale production [34]. The laser scribing technique has been demonstrated with submodules on glass substrates [30, 35] and these processing steps are also applicable to flexible substrates. The most suitable method for laser scribing is illustrated in Figure 5-2.

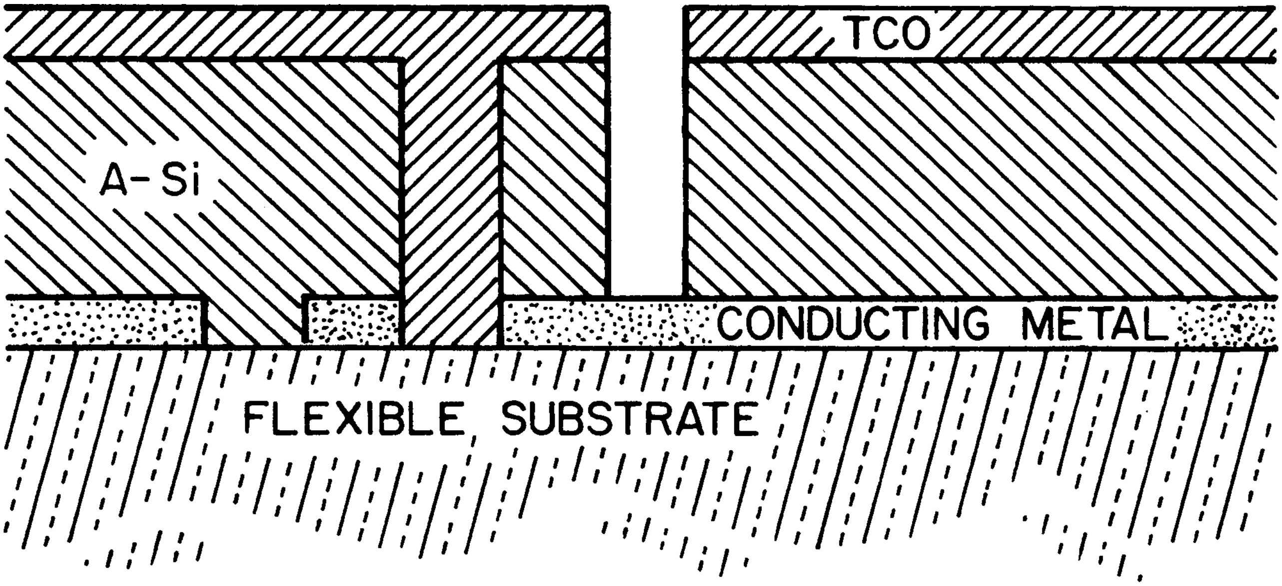

Figure 5-2. Submodule Interconnect Region For Laser Scribing

In Figure 5-3, optical micrographs of YAG laser cuts are shown for each of the three types of scribes on successive layers of the ITO/a-Si/Ni/polyimide device construction. The equipment used to laser scribe the submodules is shown in Figure 5-4.

The He-Ne laser and a photodetector are used to sense the position of the first scribe in the metal layer which serves to index the second and third cuts. Presently, the scribe line produced by the frequency doubled YAG laser is the preferred method for scribing all three layers in our solar cells. Below the 532 nm wavelength, polyimide becomes very absorptive and is damaged by the laser radiation.

5.3 Solar Simulation

A major goal of this project is to produce submodules of area greater than 1000 cm^2 and with an efficiency of greater than 8%. A small solar simulator consisting of a single ELH bulb light source has been used to evaluate devices in Task 3.

Figure 5-3. Optical Micrographs Of YAG Laser Cuts

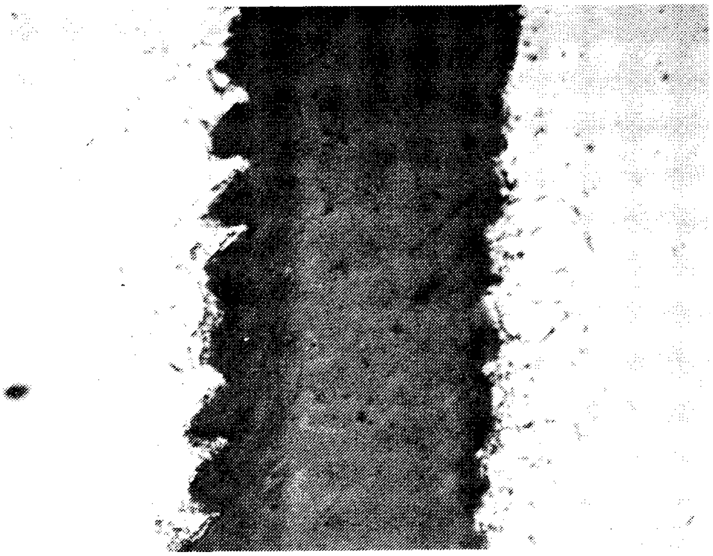

(a) Scribed Ni on polyimide

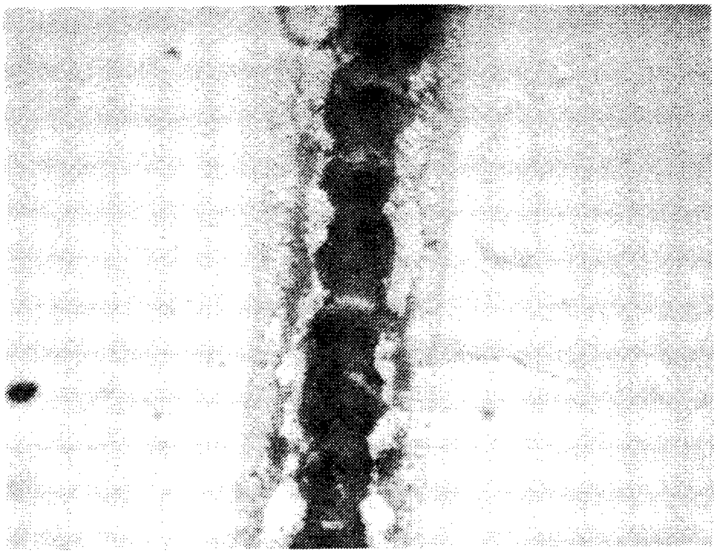

(b) Scribed a-Si on Ni

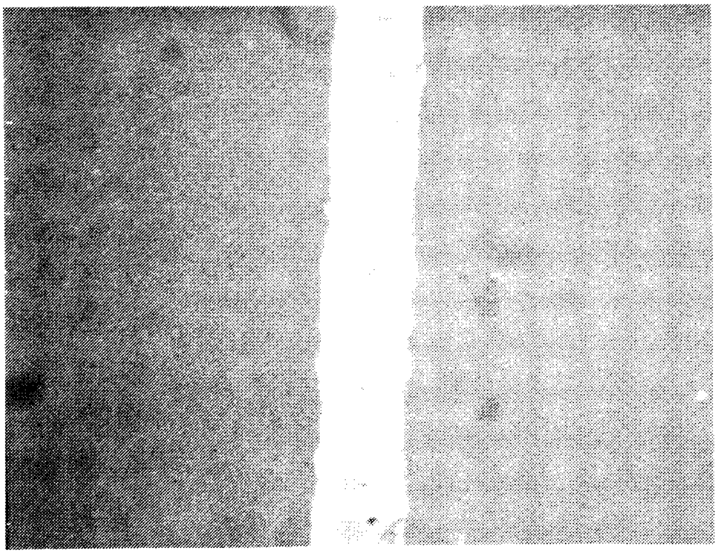

(c) Scribed ITO on a-Si

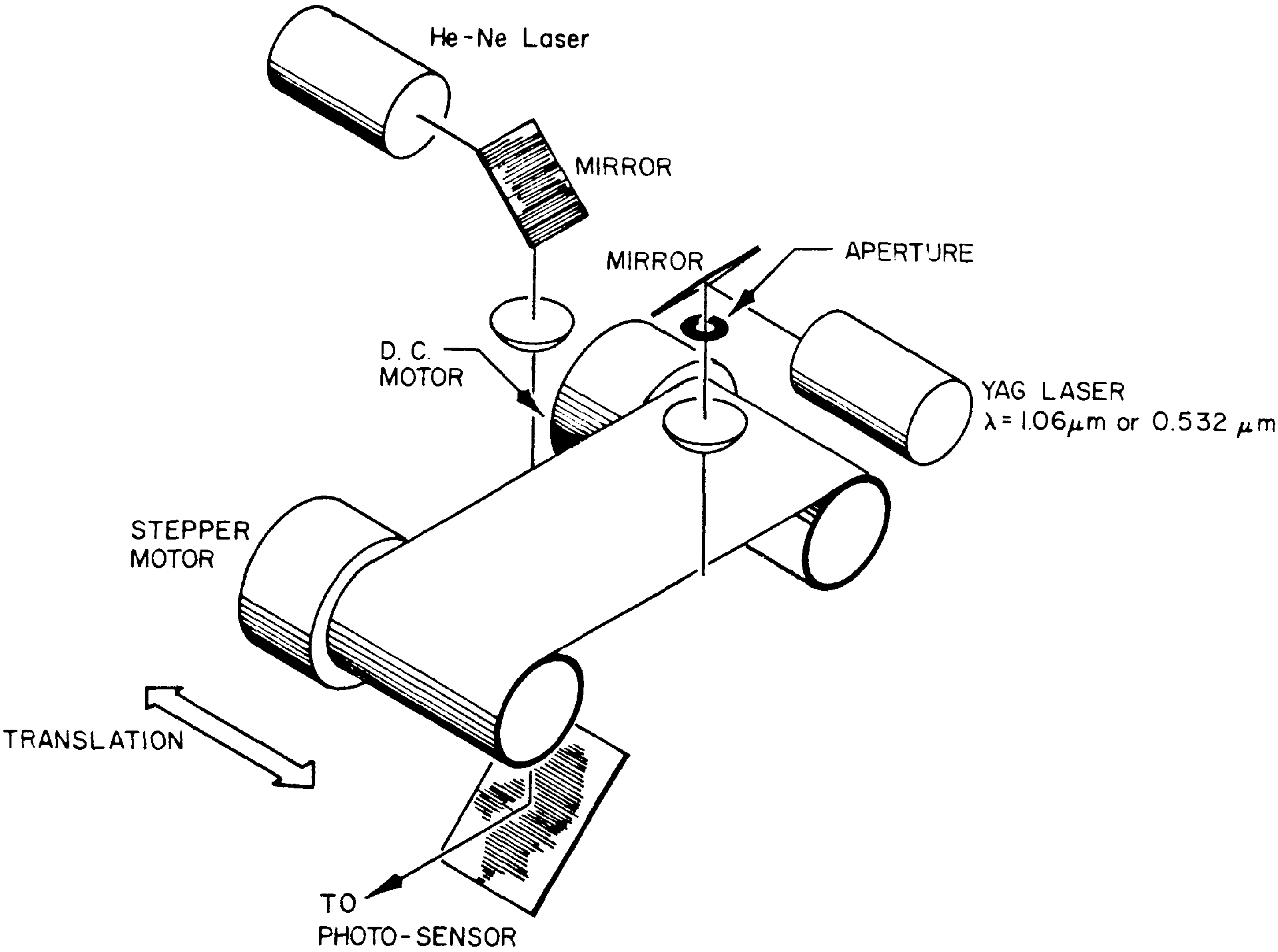

Figure 5-4. Equipment Used To Laser Scribe Submodules

A large area (10 cm x 10 cm) 5 bulb ELH solar simulator was constructed by the Institute of Energy Conversion at the University of Delaware. Representative output data from this system are shown in Figure 5-5. Calibration of the solar simulator is accomplished by performing a combination of measurements using radiometers, and standard single crystal cells, both with and without wavelength filters. For cell/submodule efficiency measurements, two basic types of reference cells are available: filtered Si cells and Hamamatsu silicon photodiode cells.

```
HAM-1      -  3         3-APR-85          TEST # 1003
  AREA= 0.660E-01sqcm         .00 hr     0 deg C

   VOC       JSC       VMP       JMP       RESVOC                          GOOD
  .5152    10.05       .3964    9.248       7.94     28.3 deg C   A fact.=1.000
  .0014   0.0000E+00   .0021   0.5379E-01          87.50    mW/sqcm  CALIB

    FF     EFF      R        G         JL          J0           # PTS  # ITER  ERROR
   70.83  4.19    5.338    .290   10.06        2.418E-06      3E3      4       0
```

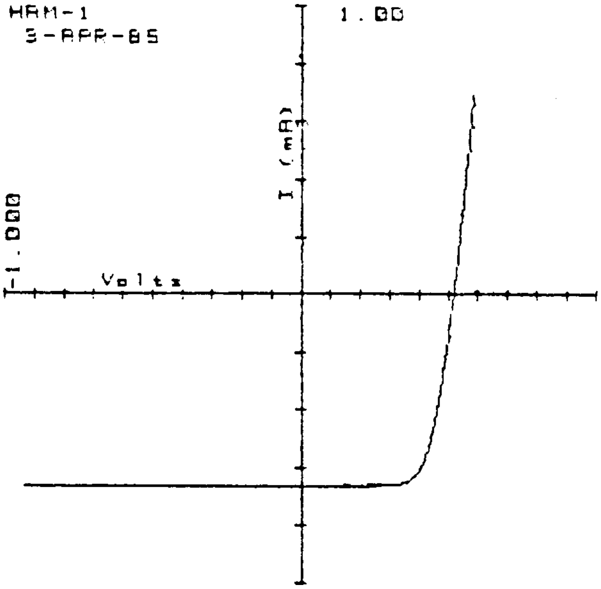

Figure 5-5. Representative Solar Simulator Output

The filtered Si reference cells are 4.0 cm^2 in area and were calibrated by SERI for spectral mismatch.

The Hamamatsu cells (S1087 type) are 0.016 cm^2 in area and are used for probing illumination uniformity. Cell temperature is maintained at 25°C by a thermoelectric cooler. Test cells are placed on the cooled test stage and held tightly to the stage platen by means of vacuum. The simulator lamps are turned on and the current/voltage is measured and recorded. One or more reference cells are used to establish the desired flux (e.g. AM1), by varying the test stage height until the calibrated short circuit current is obtained from the test cells. The calibration cell(s) are removed and the test cell is inserted into the solar simulator.

The submodules show poor performance, characterized by poor fill-factors (resistor-like linear behavior), low V_{oc}, and low J_{sc}. Using the solar simulator, high resistance in the cell interconnect regions, and shunted cells have been identified as causes for this poor performance. The average V_{oc} per cell in a 20-cell submodule is approximately 0.25 V and the effect of the interconnect is to reduce the J_{sc} substantially through the series-connected cells while leaving the V_{oc} unaffected. This is indicative of a large interconnect resistance, on the order of several hundred ohms. Efforts to reduce the interconnect resistance have been promising, although, the source of the low V_{oc} is not yet been determined. A more complete discussion relating to submodule performance is presented in Section 5.5.

5.4 Laser Scanning

A laser scanner, which has a line scan output has been used to evaluate the submodules and to detect small area defects [33, 36, 37]. The scanner uses a He-Ne laser as the light source with the beam focused to a 100 μm diameter spot. Results from laser scanning and EBIC have been useful in providing early indications of the defect types and the defect density in the submodules. This information will be utilized to improve the deposition and materials properties of the TCO and a-Si layers. Furthermore, it may be useful in designing methods to subdivide the submodule to minimize the effects caused by defects [35].

The Semi-Annual Report (June, 1985) contains a thorough discussion of laser scanning optics and the diagram of the apparatus shown in Figure 5-6.

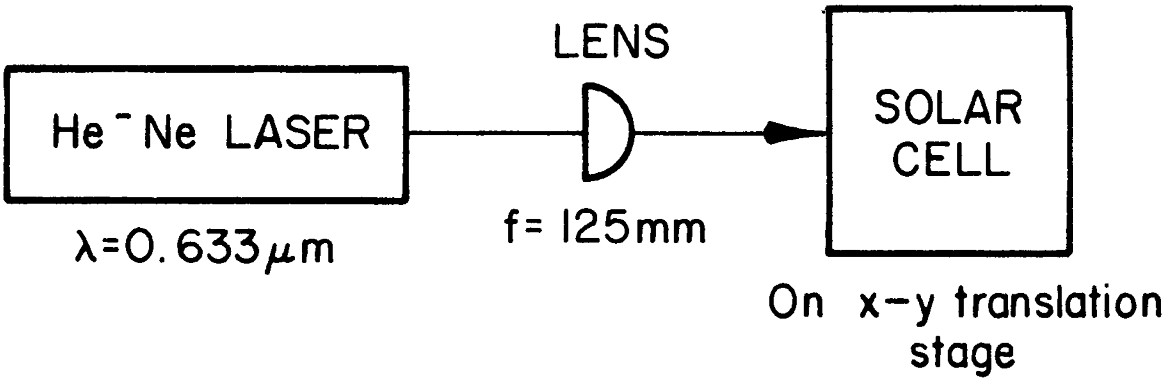

Figure 5-6. Laser Scanner System Configuration

The utility of the laser scanner system, as shown in this figure, can be expanded by adding a roll-to-roll web feed assembly to the x-y translation stage so that a 10 cm wide x 100 cm long web can be scanned. An interface to an x-y pen recorder allows two-dimensional representations of the solar cell response to the laser scan as shown in Figure 5-7.

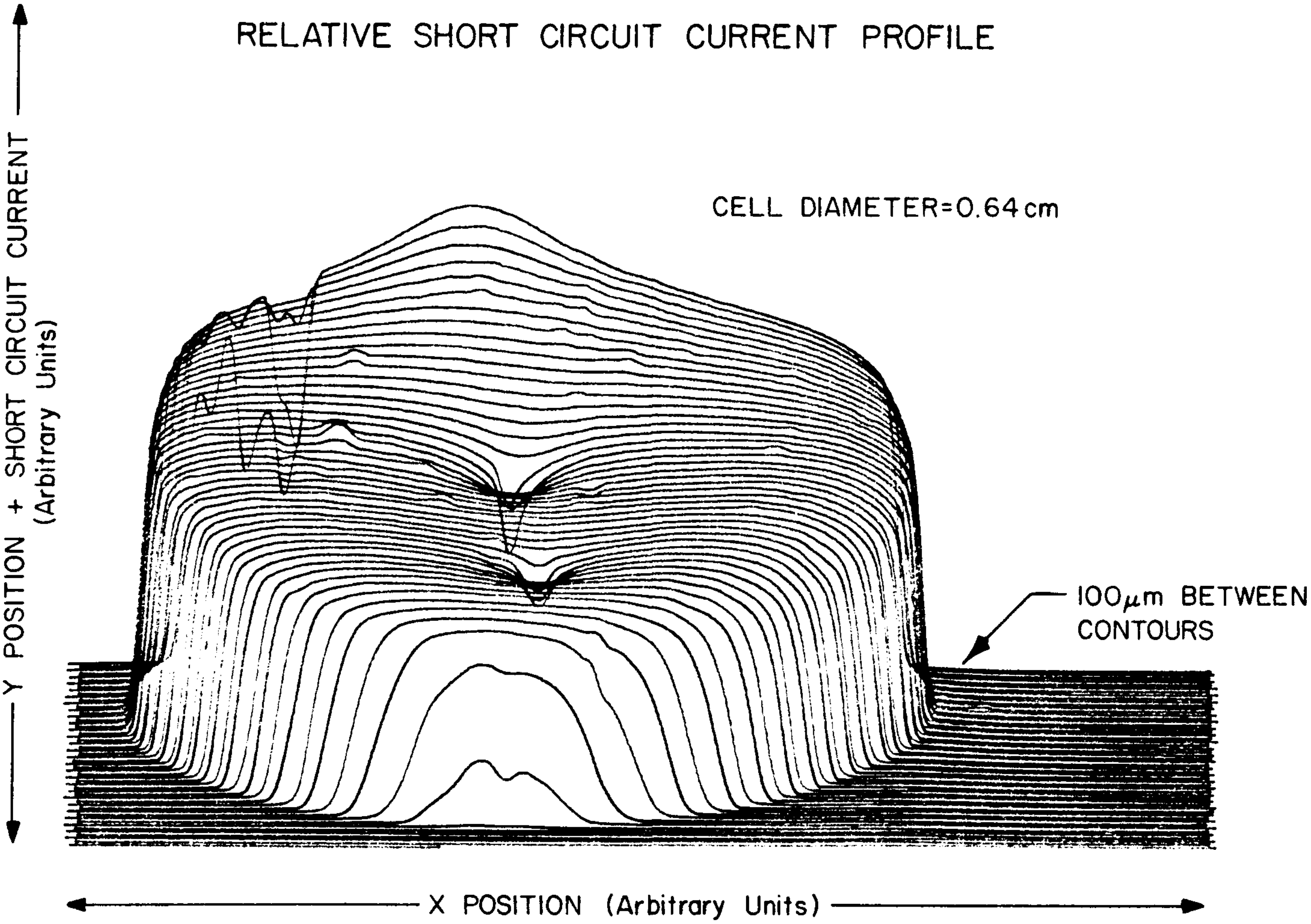

Figure 5-7. Short Circuit Current Profile

5.5 Analysis Of The Cell Inter-Connect Region, And Methods Of Interconnect Improvement

The laser scribing process can possibly damage the scribed film layer as well as introduce contamination to the succeeding film layers. The intense power of the laser rapidly heats and vaporizes the material being removed. It also causes rapid, local thermal expansion of adjacent materials creating film stress cracks, and is responsible for the deposition of the ejected material onto surrounding film surfaces. Precautions must be taken to minimize these problems.

In laser-scribed series-connected submodules, the first and third scribes, through the back metal contact and front TCO contact, respectively, serve to isolate the individual cell strips.

The second scribe, through the p-i-n a-Si device layers, serves as a connecting region between the back metal contact and front TCO contact of adjacent cell strips. Submodules which were produced initially, including the 100 cm x 10 cm submodule sent as an earlier program deliverable in June of 1985, used a second scribe that cut through the a-Si and metal layers. Contact with the subsequent TCO layer, therefore, was made with the cross-section through the back metal contact film (nickel). (The first scribe was cut through this metal layer and partially into the polyimide below, and the third scribe was through the TCO and perhaps some of the a-Si, but not through the metal layer.) Two problems were identified with the submodules produced in this manner: i) the series resistance was very high, on the order of 150 to 200 ohms across any given scribe region, and ii) the devices appeared to have a large number of shunts, most of which were probably along the interconnect scribe region. A laser scan of individual cells cut from the submodule revealed a low density of pin-hole shorts across the surface area, indicating that the problem was in the interconnect region. However, because the V_{OC} is low, the sensitivity with the laser scan is also low. Poor contact, through the second scribe, between the back Ni contact and the front TCO contact also results in the contact from one cell's TCO layer to the next cell's metal layer. This contact is made primarily through the small mini-cell (of reverse polarity) created by the region between the second and third scribe, as shown in

Figure 5-8. The effect of this reverse-polarity mini-cell is to substantially reduce the V_{oc}, as was determined from submodule pieces in which the interconnect region was masked from illumination with tape. These mini-cell effects can be reduced but not entirely eliminated.

An analysis of film surface regions surrounding both sides of the first and second scribes revealed a considerable amount of debris. In the case of the second scribe of a-Si over Ni, the scattered debris is visible particularly when overcoated with ITO. Auger analysis identified the material to be Si. No evidence of Ni was found. Pressurized N_2 gas was used to blow the debris free from the scribe region and a vacuum system was used to collect the debris, with limited effectiveness. This approach has been somewhat useful, however, in the scribing operation involving the back Ni contact and a-Si layers. For the a-Si scribe, post-treatment with compressed N_2 gas followed by a Kimwipe cleaning step has proven effective in removing the a-Si/Ni debris.

Provided that the Ni layer is not removed, carbon contamination should not be a problem with the second scribe, as in the past when the scribe went all the way through the a-Si and the Ni, into the plastic. After several experiments to investigate the conductivity through the second scribe, between the back contact and the ITO, techniques have been developed which should eliminate this problem. Resistances of 5 ohms have been measured across the Ni/ITO interconnect (second) scribe.

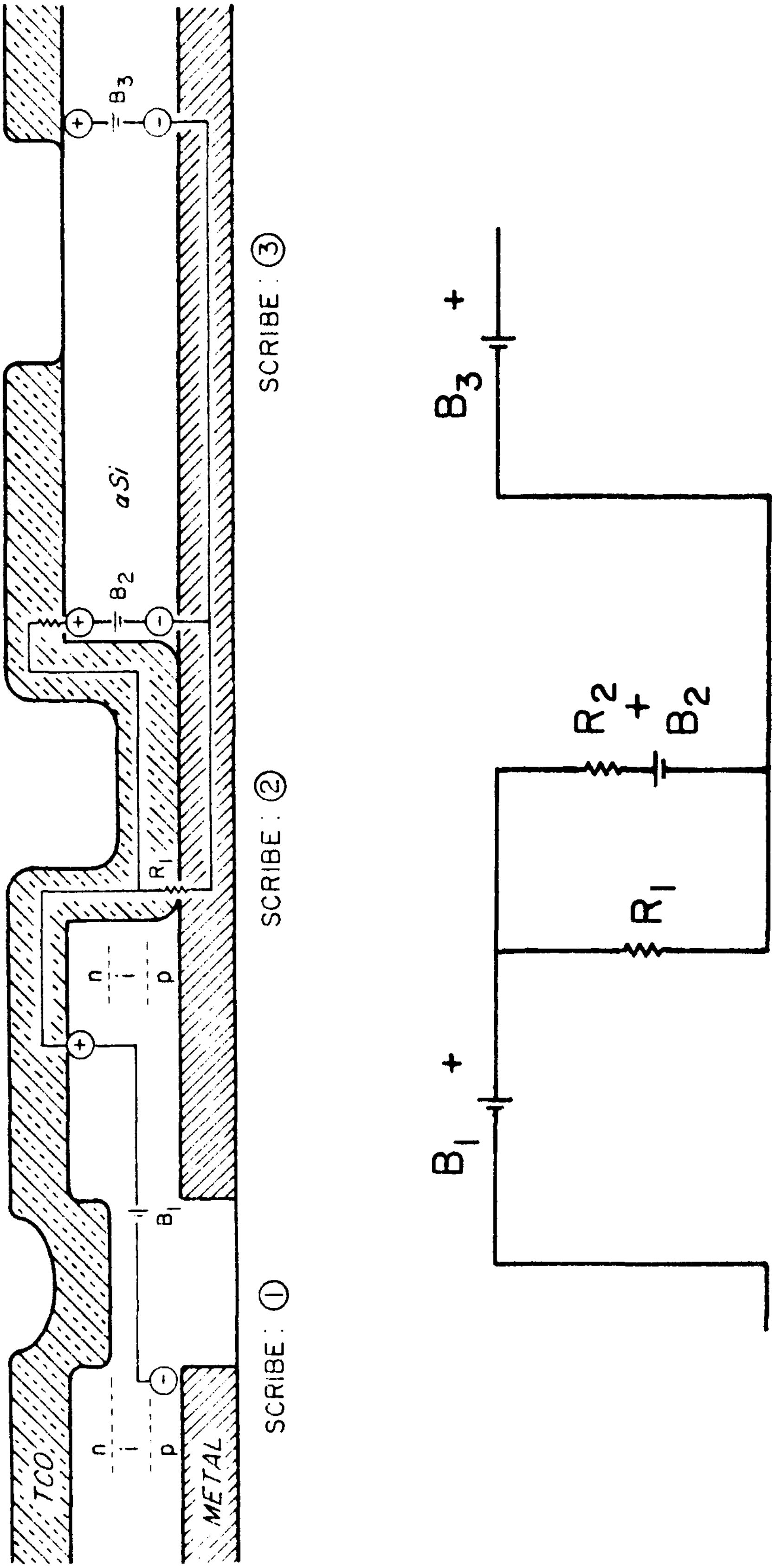

Figure 5-8. Schematic Representation Of The Effect Created By High Interconnect Resistance Through Scribe #2

The first scribe presents more difficult problems. In addition to carbon contamination from the heated plastic, molten metal droplets cause potential shunt regions to occur along the scribe edge. These shunts are formed from metal debris that is not removed in the dry wipe process (See Figure 5-9). Ultrasonic cleaning has been considered, but not used due to the problems of introducing a wet-cleaning process into a vacuum deposition line. The low heat capacity of a thin plastic substrate, as compared to a 1/8" thick glass substrate may be part of the problem. Undoubtedly, vapor generated from the heated polyimide promotes material droplet ejection. The approach used for p-i-n devices made on glass superstrates, produced by other manufacturers, involves scribing the TCO first, followed by the a-Si, and usually the deposition of the metal back contact is masked to prevent damage from laser scribing to the underlying a-Si layers. The scribe of the initial TCO layer on glass probably does not leave spot-welded debris on the surface of the scribed layer, as apparently occurs with scribing metal layers first. In addition to using wet-bath cleaning as a post-treatment, there are also water-soluble liquid surface coatings which are applied before scribing, and later allow debris to be collected from the scribe. Removal of the protective coating can be accomplished with a distilled-water bath.

An alternate approach to post-scribe wet-bath treatments, is to avoid scribing the metal layer entirely, and instead deposit the metal film by a dry process using appropriate wire masks. Alternatively, a wet film process involving photolithographic masks can be used.

There is also evidence of crystallization out to several hundred microns, from the scribe through a-Si. Raman spectroscopy experiments revealed the increased presence of the single crystal Si peak at ~520 cm^{-1} in the vicinity of that scribe. Those scribes that showed no re-melt material, but did show material removed by vaporization, displayed the least crystallization. Repeatable, high-power, short duration pulses are evidently the key to successful laser scribing.

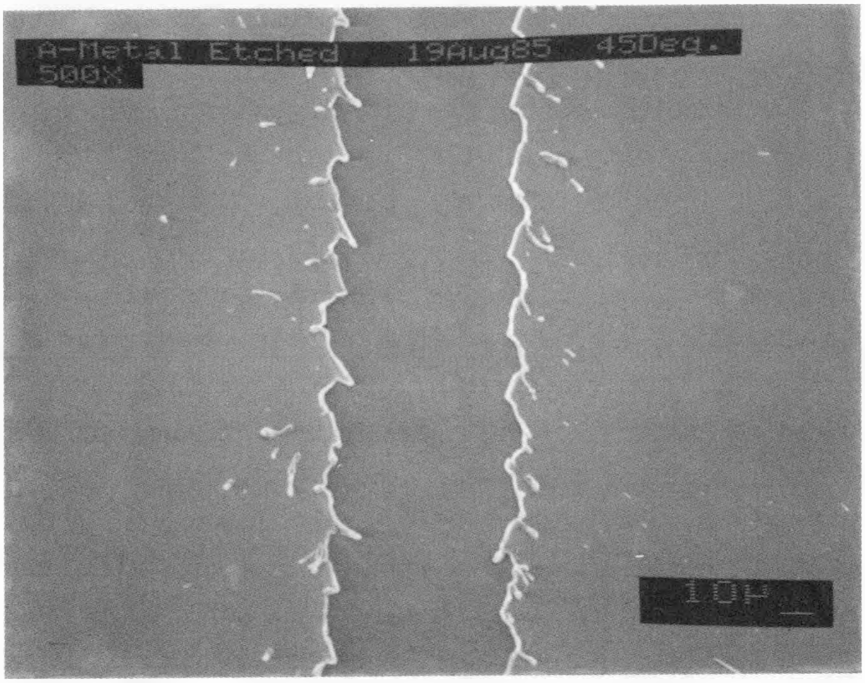

Figure 5–9. **Scribe Through Ni On Polyimide**
Note metal droplets on both sides of the scribe, despite post-scribe etching with H-plasma. Cleaning with a Kimwipe does not remove these droplets.

6.0 TASK FIVE - MULTI-CHAMBER DEPOSITION SYSTEM

The multi-chamber deposition system was made operational in June, 1985. Numerous single and multi-layer films have been deposited since that time. One series of deposition runs demonstrated that the level of cross-contamination between the deposition chambers is negligible. Experimental results are presented in Section 6.1.

Deposition rates of 5 ± 1 Å/second for all three deposition chambers have been obtained using a pressure of 1.0 torr in each of the chambers, a reactant gas mixture of 10% silane in hydrogen, 10 watts RF power in the p- and n- chambers, and 20 watts in the i-chamber. Using these deposition parameters, good quality intrinsic and doped p^+ and n^+ films have been produced. Some p-i-n multi-layer films were deposited onto metallized polyimide and small area cells were prepared by evaporating semi-transparent chromium contacts. Initially, these p-i-n layers were deposited under static web conditions. Following this, semi-continuous web conditions were used. Most recently, depositions have been made by continuous deposition processing. The p- and n-layer deposition conditions were modified to reduce their deposition rates prior to making continuous deposition runs. Although p-i-n deposition conditions have yet to be optimized, some of the small area solar cells produced to date have shown reasonably good I-V characteristics.

6.1 Cross-Contamination Experiment

A series of a-Si deposition runs were performed specifically for the purpose of determining the amount of cross-contamination between the p, i, and n deposition chambers. The experimental procedure consisted of depositing both doped and undoped a-Si films onto polyimide web as shown in Table 6-1.

Table 6-1. Cross-Contamination Experiment

Run Sequence	p-chamber	i-chamber	n-chamber
1	I	I	I
2	B_1*	I	I
3	B_1	I	I
4	I	I	P_1
5	B_1	I	P_1
6	I	I	I
7	B_2	I	I
8	I	I	P_2
9	B_2	I	P_2
10	I	I	I

I = undoped, 10% SiH_4 in H_2 all chambers
B_1 = 1% B_2H_6 in SiH_4, 10% SiH_4 in H_2, 10W
B_1* = 1% B_2H_6 in SiH_4, 10% SiH_4 in H_2, 0W
B_2 = 2% B_2H_6 in SiH_4, 10% SiH_4 in H_2, 10W
P_1 = 1% PH_3 in SiH_4, 10% SiH_4 in H_2, 10W
P_2 = 1.7% PH_3 in SiH_4, 10% SiH_4 in H_2, 10W

In each of these runs, a-Si was simultaneously deposited onto a stationary web in all three chambers for 30 minutes. After each deposition run and, without breaking vacuum, the web was advanced to expose uncoated polyimide in all three chambers prior to the next run. As noted in Table 6-1, dopant gases were used in only the p- and n-chamber. RF power was not used in the p-chamber in the second run because it was suspected that a-Si might be deposited by CVD, however a-Si film did not deposit. The series of ten deposition runs produced a total of twenty-nine film samples for analysis. The properties of the i-films would be expected to vary from run to run if substantial cross-contamination did occur. For example, if diborane used in the p-chamber diffused into the i-chamber, then i-layer films would be expected to exhibit p-type characteristics. On the other hand, if i-layer properties do not vary, then one can assume that cross-contamination is very low. Following this series of runs, samples were cut from the web and analyzed for activation energy (E_a), room temperature dark conductivity (σ_D) and conductivity under AM1 illumination (σ_L).

Activation energy data are presented in Figure 6-1. The data shows that the activation energy of films deposited in the p- and n-chambers showed considerable variation among the runs, while E_a values for films deposited in the i-chamber did not. Variations of only a few hundredths of an eV were observed for the i-layer films. Activation energies of doped p-layer films ranged between 0.4 to 0.5 eV, depending on the dopant level used. Doped n-layer films had an E_a value of 0.20 eV, independent of the dopant level. Films with the highest activation energy were those deposited in the p-chamber following a B_2H_6 dopant run. These films are believed to be lightly B_2H_6-doped due to carry-over from the previous run.

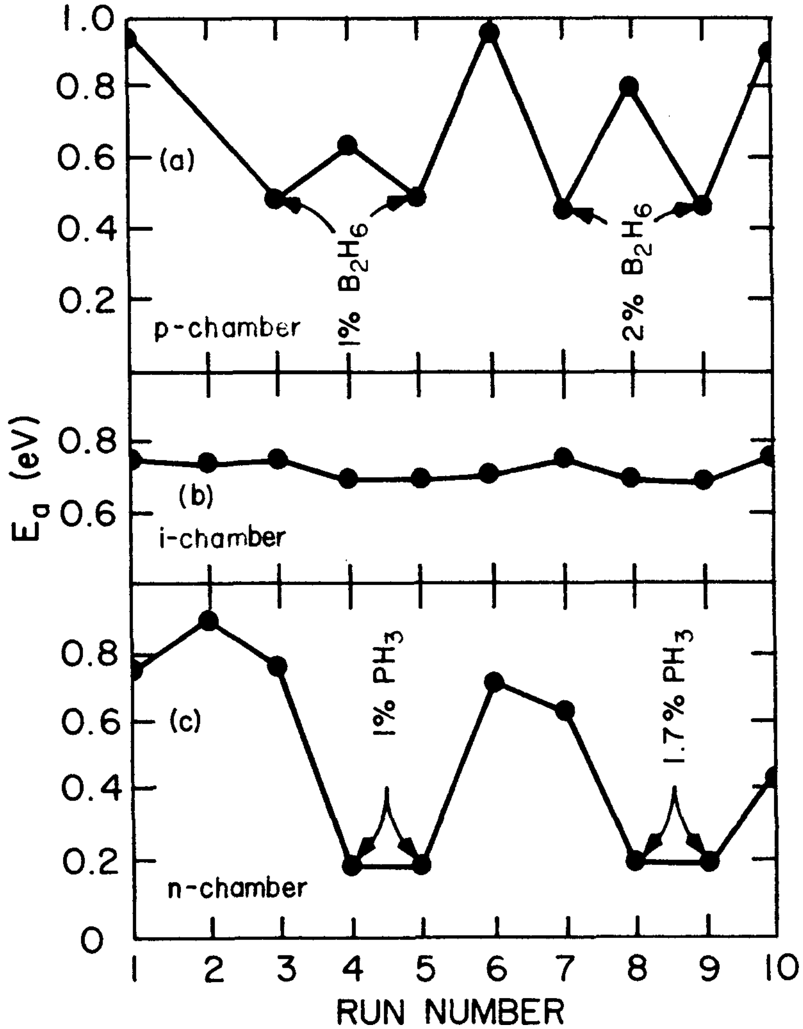

Figure 6-1. Activation Energy For Films Deposited In The (a) p-Chamber, (b) i-Chamber, and (c) n-Chamber

Dark conductivity data are found in Figure 6-2. Conductivity values vary by six to seven orders of magnitude depending on whether or not the films were doped. On the other hand, the conductivity values of films produced in the i-chamber vary by no more than a factor of two or three. The lowest conductivity films were produced in the p-chamber immediately following dopant runs. Here again, diborane carry-over is believed to be responsible for this. Figure 6-2c suggests carry-over of phosphine from the increasing conductivity of non-doped films.

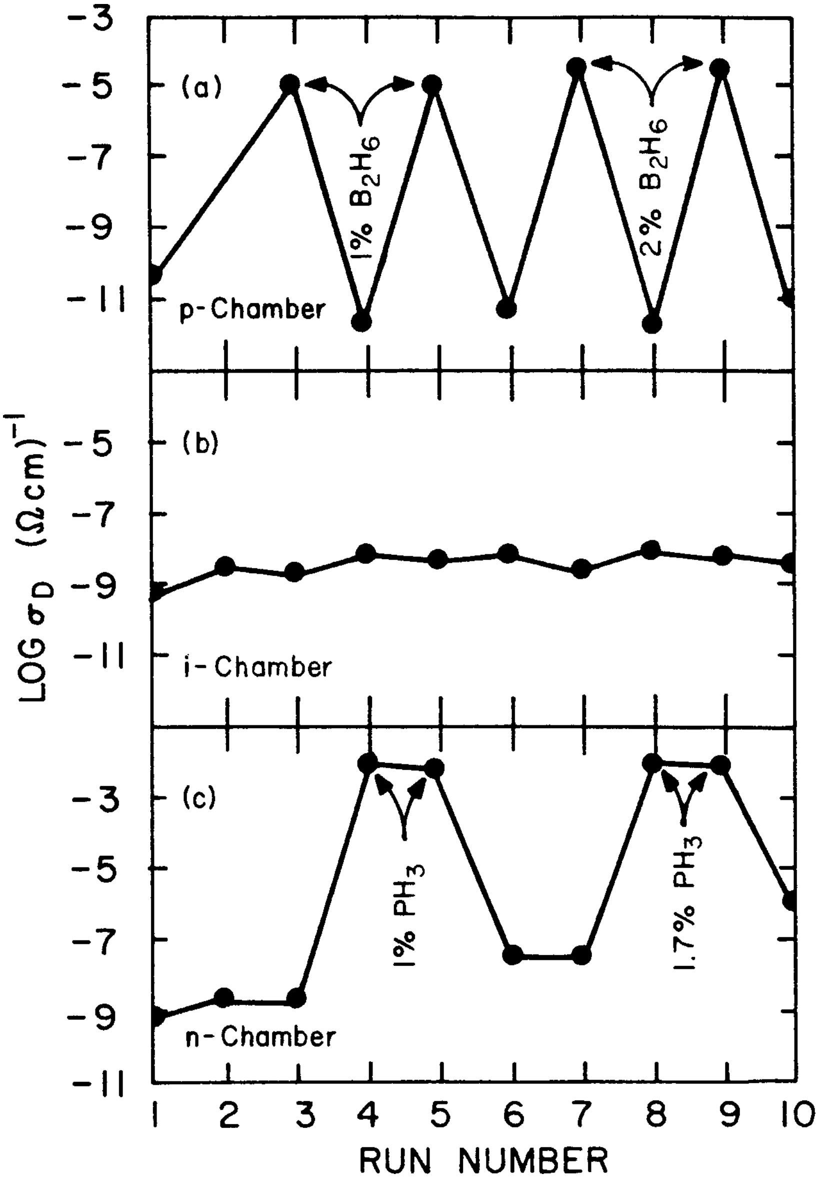

Figure 6-2. Dark Conductivity For Films Deposited In The (a) p-Chamber, (b) i-Chamber, and (c) n-Chamber

Light conductivity data are found in Figure 6-3. Interestingly, the lowest conductivity films under illumination were deposited in the p-chamber following each dopant run. These films also had the highest light to dark conductivity ratios. Notice also that i-layer films had conductivities greater than 1 x 10^{-4} $(\text{ohm cm})^{-1}$, indicative of good quality intrinsic films.

In conclusion, the level of cross-contamination in the multi-chamber deposition system is very low. Cross-contamination is believed to be less than 1 ppm in the i-chamber when 1% dopant levels are used in the p- and n-chambers. Furthermore, the system produces intrinsic and doped films of good quality as evidenced by the measured electrical characteristics.

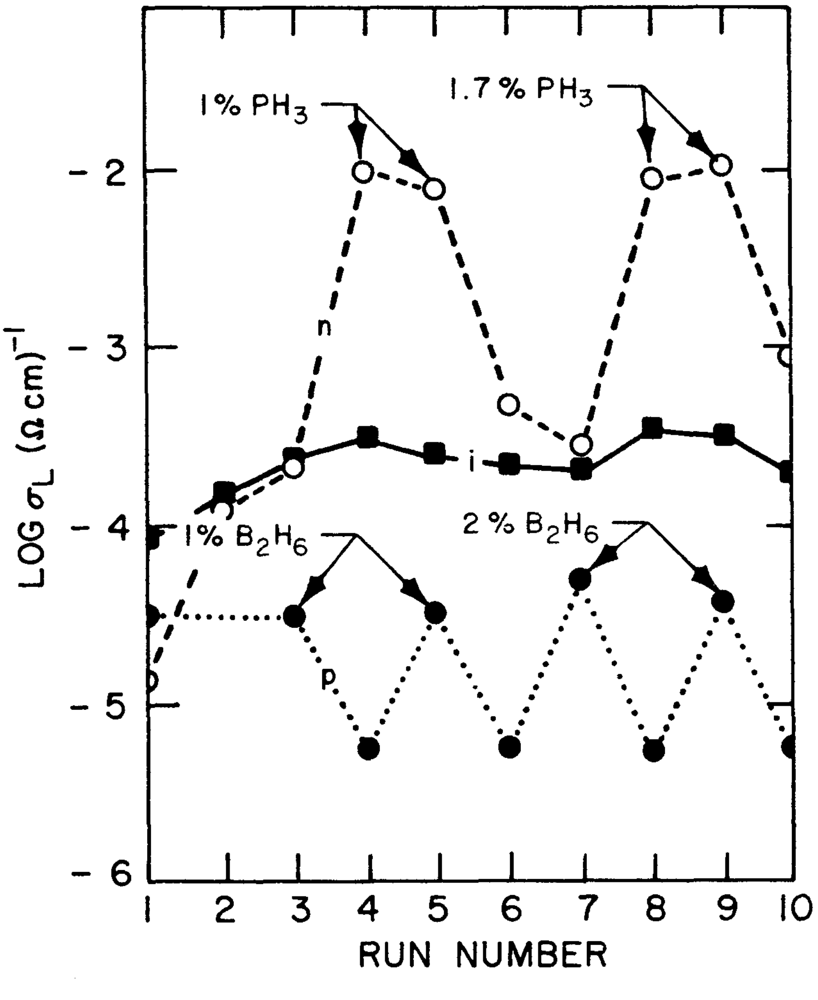

Figure 6-3. Light Conductivity Measured Under AM1 Illumination For Films Deposited In The p, i, And n-Chambers

6.2 Fixed Frame Deposition of P-I-N Layers

Some multi-layer a-Si p-i-n films were deposited onto Ni-coated polyimide using the same deposition conditions employed in the above cross-contamination study. It was of interest to observe whether these films would produce good I-V characteristics under illumination. Semi-transparent Cr contacts were used as the top electrodes. The p-i-n films were deposited by a fixed frame process, i.e., first p-type film was deposited in the p-chamber under stationary web conditions, the web was then moved to the i-chamber for the i-layer deposition, and finally to the n-chamber for the n-layer deposition. The deposition time in each chamber was chosen to give the desired film thickness. The thickness of the p-layer films was 500 Å, the i-layer films were 5000 Å thick, and the n-layer films were 250 Å thick. The fixed frame deposition method allowed the deposition conditions employed in earlier studies to be used since deposition rates in all three chambers were 5 ± 1 Å/second. One variation to the above deposition procedure was to deposit the undoped i-layer in the p-chamber. This was accomplished by shutting off the diborane flow after the deposition of the p-layer and continuing the deposition in the p-chamber until the i-layer deposition was complete. The polyimide web was then advanced to the n-chamber to complete the p-i-n film sandwich.

A large number of p-i-n layers were fabricated in one pump-down by using a length of metallized web in excess of 60 feet. This permitted some parameters such as web pre-treatment and substrate temperature to be varied. The deposited web was removed from the multi-chamber; samples were cut from the web and then overcoated with small Cr contacts for I-V measurements. Transmission of the Cr contacts was ~50%.

A wide variety of I-V characteristics were measured on these p-i-n cells. The best I-V characteristics were obtained from cells which had the i-layer deposited in the p-chamber. V_{OC} usually ranged between 0.80 and 0.87 volts, and the FF typically measured about 0.60. Cells with the i-layer deposited in the i-chamber invariably had lower V_{OC} (0.25 to 0.70 volt) and FF ($\leq$ 0.55). Two typical I-V plots are shown in Figure 6-4.

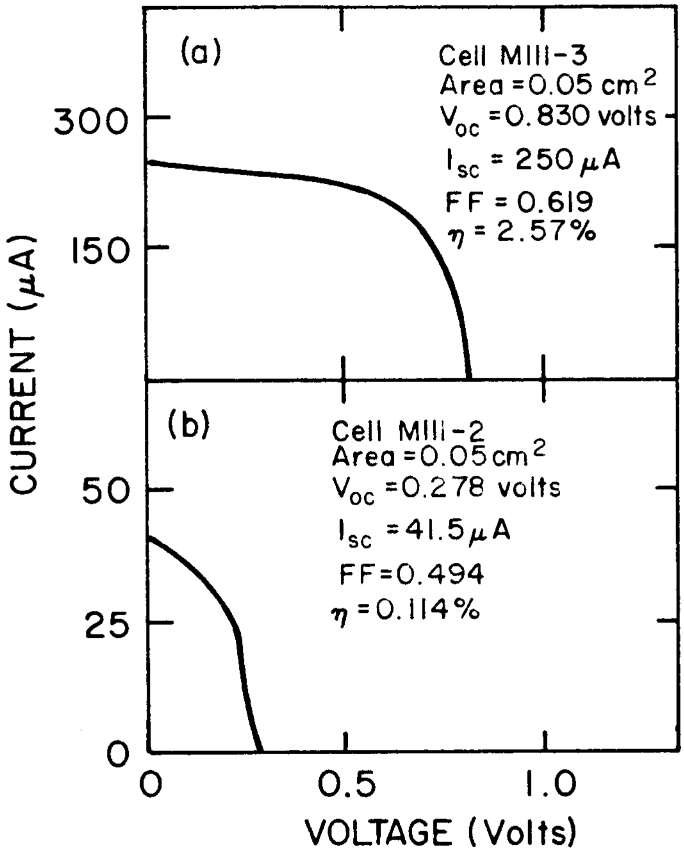

Figure 6-4. I-V Characteristics Of A Cell With The i-Layer Deposited In The (a) p-Chamber And In The (b) i-Chamber

There are two possible explanations for the inferior electrical characteristics of cells produced when the i-layer is deposited in the i-chamber. One possibility is that diborane carry-over does not occur in the i-chamber as it does in the p-chamber. It was noted in the cross-contamination experiment that diborane carry-over drastically reduces both the dark and light conductivities. A second possible explanation is that an interfacial layer forms on the p-layer during the time that the frame is advanced to the i-chamber. A subsequent deposition experiment indicated that diborane carry-over is responsible for the improved characteristics. In this experiment all three deposition layers were deposited onto a moving web, one layer at a time, and the thickness of each layer was adjusted by varying the web speed. The i-layer was deposited in the p-chamber but the time lapse between deposition layers was of the order of minutes. If the formation of interfacial layers is the problem in the above-mentioned cells, then cells produced in this experiment would have inferior characteristics. However, the cells demonstrated acceptable V_{OC} (~0.80 volts) and FF (≈ 0.58). Hence, it is concluded that the i-layer must be doped and profiled with a small amount of diborane in order to obtain good I-V characteristics.

6.3 Continuous Mode Deposition of P-I-N Layers

When depositing p-i-n layers in a continuous mode, it is necessary to satisfy the requirements for film thickness. Both the p^+ and the n^+ layers must be thin compared to the i-layer thickness. Additionally, the capability to independently vary the thickness of each layer for the purpose of optimizing the properties of the p-i-n cells is highly desirable, particularly in the early development stages. One possible approach involves placement of an adjustable aperture in at least two of the deposition chambers and controlling the area of deposition on the polyimide web. A second approach is to vary the RF power level to adjust film thickness. These approaches have drawbacks. An adjustable aperture is difficult to adapt to our multi-chamber system and varying the RF power level can affect film properties if changed too much. The method eventually selected to reduce the deposition rate to less than 1 Å/second involves reducing the silane concentration in the p and n deposition chambers. Reducing the silane concentration provides a number of additional benefits, including reduced silane consumption, decreased powder formation and lower dopant flow rate requirements which in turn reduces cross-contamination even further. Also, microcrystalline silicon may be deposited under low silane concentrations. Hence, a number of n and p films were deposited under reduced silane concentrations for the purpose of characterizing the properties of the films produced at low deposition rates.

p-layers were deposited using 1, 2, and 3% silane, respectively, and 2% diborane, while n-layers were deposited using 1% silane and 1% phosphine at different power levels. As expected, deposition rates were significantly reduced. Table 6-2 lists activation energy values measured on these films.

Table 6-2. Activation Energy Of p^+ Layers And n^+ Layers Deposited In The Continuous Mode At Various SiH_4/H_2 Ratios And RF Power

Film Type	SiH_4/H_2	RF Power	E_a
p	1%	10W	0.397
p	2%	10W	0.338
p	3%	10W	0.328
n	1%	10W	0.361
n	1%	20W	0.318
n	1%	30W	0.016
n	1%	40W	0.041
n	1%	50W	0.0293
n	1%	100W	0.0566
n	1%	150W	0.0570
n	1%	200W	0.0646

Films were also deposited in the intrinsic chamber with diborane levels ranging from 0 to 10 ppm. As expected, both the dark and light conductivities decreased with diborane concentration as shown in Figure 6-5. A number of p-i-n layers were deposited onto a moving web in a continuous process using the new operating conditions. Deposition variables included web speed, silane concentration in the p-zone, and RF power level in the n-zone. I-V characteristics were measured on a number of p-i-n cells, and although this was the first attempt at continuous deposition, some of the cells gave reasonably good properties. An I-V characteristic of one of the better cells is shown in Figure 6-6.

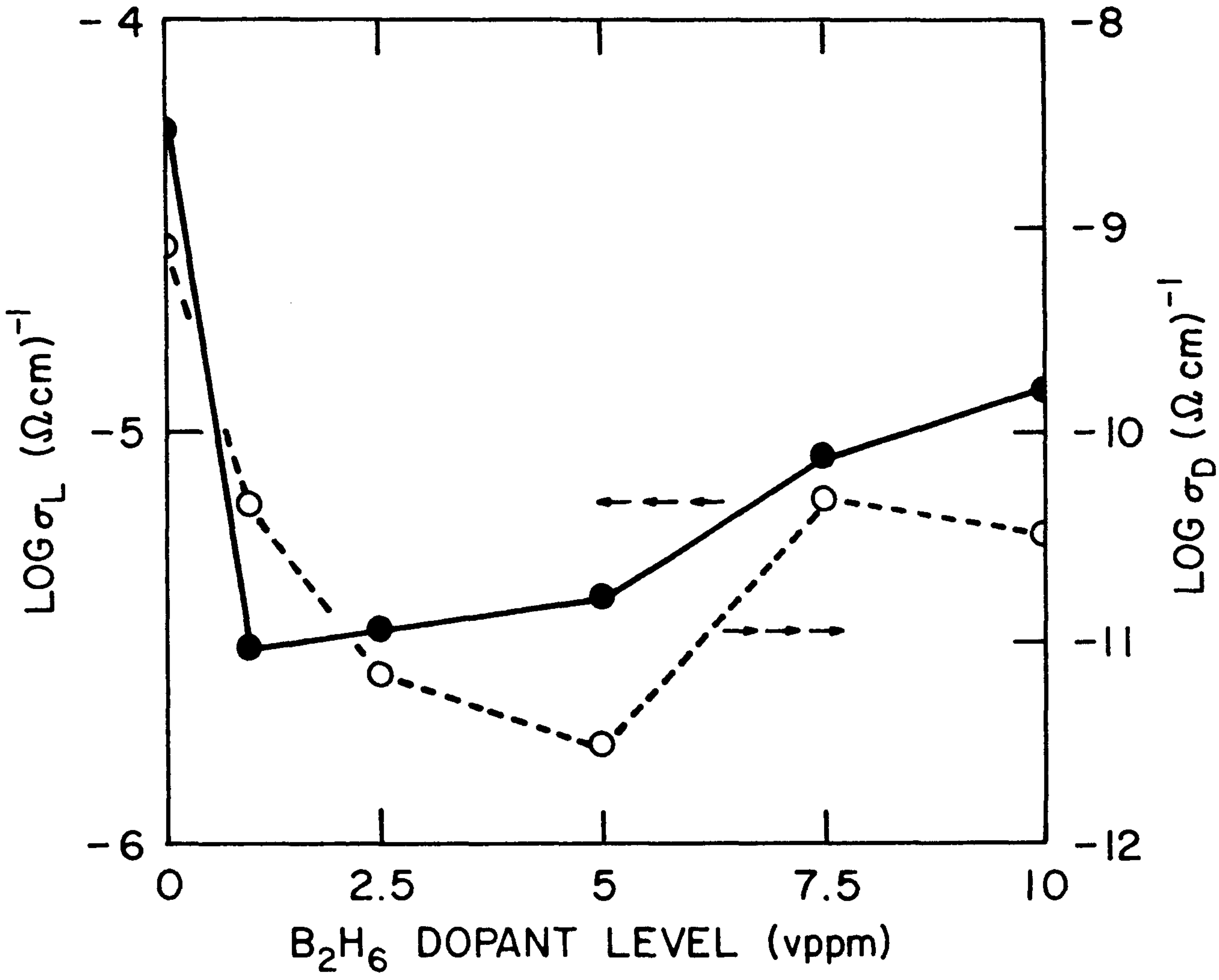

Figure 6-5. Light And Dark Conductivity Of I-Films As A Function Of B_2H_6 Doping Level In PPM

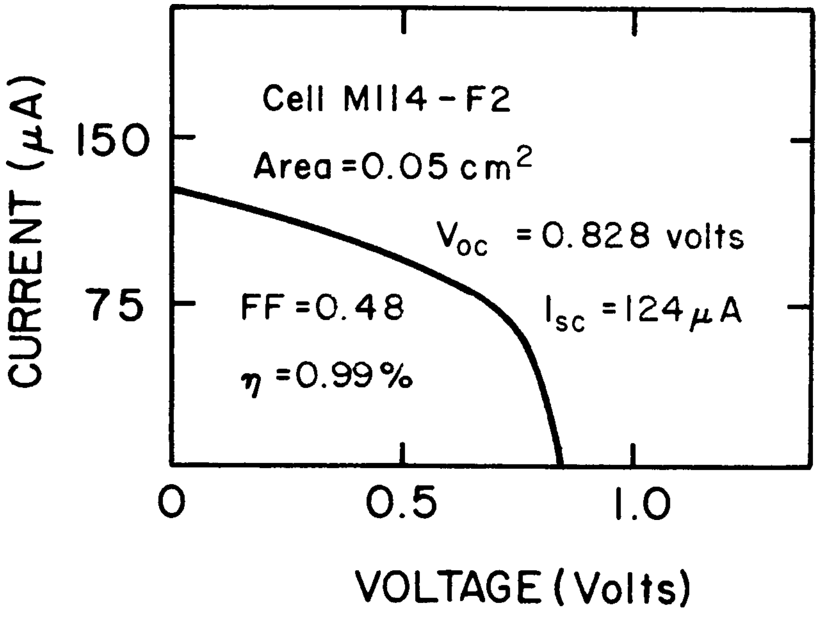

Figure 6-6. I-V Characteristics From One Cell Produced In The First Continuous Deposition Run

6.4 Summary

Progress has been made in depositing both single layer and p-i-n multi-layer films in the multi-chamber system: n-i-p films have the desired electrical and optical properties and these layers can be deposited continuously and sequentially to produce usable p-i-n devices. Future work will concentrate on optimizing the continuous deposition of p-i-n layers on both scribed and non-scribed polyimide web, and the optimization of i-layer B doping.

7.0 REFERENCES

1. Patel, R.I., "Thermodynamic Study of the Silane-Hydrogen Chemical System," Proceedings of the Materials Research Society, April, 1985.
2. Patel, R.I., J. Shirck, D.J. Olsen, N.T. Tran and K.A. Epstein, "High Deposition Rate Studies of Hydrogenated Amorphous Silicon," Proceedings of the 18th IEEE Photovoltaic Specialists' Conference, Las Vegas, Nevada, October 21-25, 1985.
3. Knights, J.C., G. Lucovsky and R.J. Nemanich, Journal of Non-Crystalline Solids 32 (1979) 393-403.
4. Moore, A.R., Semiconductors and Semimetals, Vol. 21, Part C, Academic Press, Inc., 1984, pp. 239-256.
5. Swanepoel, R., J. Phys. E. 16, (1983), 1219.
6. Paulick, T.C., "Inversion of Normal Incidence (R, T) Measurements to Obtain n + ik for Thin Films" submitted to Applied Optics.
7. Cody, G.D., E.R. Wronski, B. Abeles, R.B. Stephens, and B. Brooks: Solar Cells 2 (1980) 227.
8. Moore, A.R., J. Appl. Phys. 54 (1983) 222.
9. Goodman, A.M., J. Appl. Phys. 32 (1961) 2550.
10. Moore, A.R., and D.E. Kane, J. Appl. Phys. 56 (1984) 2796.
11. Hack, M. and M. Shur, J. Appl. Phys. 55 (1984) 2967.
12. Rose, A., "Concepts in Photoconductivity and Allied Problems," (Interscience, New York, 1963), pp. 40-43.
13. A.R. Moore, private communication.
14. Street, R.A. and D.K. Biegelsen in "The Physics of Hydrogenated Amorphous Silicon II," Topics in Applied Physics, ed. by J.D. Joanklopoulous and G. Lucovsky, Vol. 56, Springer-Verlage and G. Lucovsky, 1983, pp. 196-259.
15. M. Lowry, private communication.
16. As reported at PVSEC-1, November 13-16, 1984, Kobe, Japan.
17. Wong, B., D.L. Morel and V.G. Grosvenor, Technical Digest of the International PVSEC-1, Kobe, Japan, page 433.
18. Masataka Hirose, Japan Annual Reviews in Electronics, Computers and Telecommunications, Vol. 6, Amorphous Semiconductor Technologies and Devices, p. 173.
19. Born, M. and E. Wolf, Principles of Optics, Third edition, p. 66 ff.

20. Matson, T., R. Bird, and K. Emery, "Terrestrial Solar Spectra: Solar Simulation and Solar Cell Efficiency Measurements," DE 82002082, SERI/TR-612/964, September, 1981, pp. 117-123.

21. Weaver, J.H., "Optical Properties of Metals," CRC Handbook of Chemistry and Physics, (1985) E-363.

22. Cody, G.D., "The Optical Absorption Edge of a-Si:H," in Semiconductors and Semimetals, Vol. 21, edited by J. Pankove (Academic Press, New York, 1984), Part B, pp. 20-21.

23. Silicon Processing for Photovoltaics, Editors K.V. Rovi and C.P. Khaltah, North Holland Publishing, 6.

24. Han, M.K. and W.A. Anderson, Technical Digest of International Electron Device Meeting, Washington, D.C. (1981).

25. Sakata, I. and Y. Hayashi, Appl. Phys. Lett., 42, (1983) 279.

26. Hack, M. and M.S. Shur, J. Appl. Phys. 55 (1984), 12.

27. Kanagai, M., K.S. Lin, P. Sichanugrist, K. Konori, and Y. Takahashi, Proceedings of the 16th IEEE Conference on Photovoltaics, San Diego, p. 1321.

28. Hanak, J.J., "Monolithic Solar Cell Panel of Amorphous Silicon," Solar Energy, Vol. 23, 1979, p. 145.

29. Wyeth, N. Convers, "Sheet Resistance Component of Series Resistance in a Solar Cell as a Function of Grid Geometry," Solid State Electronics, Vol. 20, 1977, p. 629.

30. Tyan, Y. and E.A. Perez-Albuerne, "A Simple Monolithically Integrated Thin-Film Solar Cell Array," Record of the 16th IEEE Photovoltaic Specialists' Conference, 1982, p. 928.

31. Kiss, Z., "Research on High Efficiency Single-Junction Monolithic Thin Film Amorphous Silicon Solar Cells," SERI Amorphous Silicon Subcontractors' Review Meeting, December, 1983.

32. Gupta, Y., H. Liers, S. Woods, S. Young, R.DeBlasio, And L. Mrig, "Optimization of a-Si Solar Cell Current Collection," Record of the 16th IEEE Photovoltaic Specialists' Conference, 1982, p. 1092.

33. June, 1985 Semiannual.

34. Firester, A.H., "The Manufacture of Amorphous Silicon Photovoltaic Modules, Proceedings of the SPIE - Photovoltaics for Solar Energy Applications II, Vol. 407, 1983, p. 37.

35. Yamazaki, S., K. Itoh, S. Watabe, A. Mase, K. Urata, K. Shibata, and H. Shimohara, "Mask-less Fabrication of a-Si Solar Cells Using Laser Scribe Process," Record of the 16th IEEE Photovoltaic Specialists' Conference, 1982, p. 1092.

36. Takakura, H., K. Fujimoto, K. Okuda, C. Coluzza and Y. Hamakawa, "Spectroscopic Laser Scanning Analysis of Photo-Induced Current on a-Si Solar Cells," Japanese Journal of Applied Physics, Vol. 22, 1983, p. 569.

37. SERI Photovoltaic Advanced Research and Development: An Overview, SERI/sp-281-2235, February, 1984, DE84004492, U.C. Category 63. Available from: Superintendent of Documents, U.S. Government Printing Office, Washington, D.C. 20402.